Artificial Neural Network based Transferable Interatomic Potentials: Application for Gold Nanoparticles and its alloys

A THESIS

Submitted in partial fulfillment of the

requirements for the award of the degree

of

DOCTOR OF PHILOSOPHY

by

SHWETA JINDAL

DISCIPLINE OF CHEMISTRY

INDIAN INSTITUTE OF TECHNOLOGY INDORE

AUGUST 2020

INDIAN INSTITUTE OF TECHNOLOGY INDORE

CANDIDATE'S DECLARATION

I hereby certify that the work which is being presented in the thesis entitled **ARTIFICIAL NEURAL NETWORK BASED TRANSFERABLE INTERATOMIC POTENTIALS: APPLICATION FOR GOLD NANOPARTICLES AND ITS ALLOYS** in the partial fulfillment of the requirements for the award of the degree of **DOCTOR OF PHILOSOPHY** and submitted in the **DISCIPLINE OF CHEMISTRY, Indian Institute of Technology Indore**, is an authentic record of my own work carried out during the time period from July, 2015 to July, 2020 under the supervision of Dr. Satya S. Bulusu, Associate Professor, Discipline of Chemistry, IIT-Indore.

The matter presented in this thesis has not been submitted by me for the award of any other degree of this or any other institute.

Shweta (10-08-2020)
Signature of the student with date
(SHWETA JINDAL)

This is to certify that the above statement made by the candidate is correct to the best of my knowledge.

10-08-20
Signature of Thesis Supervisor with date
(DR. SATYA S. BULUSU)

SHWETA JINDAL has successfully given his/her Ph.D. Oral Examination held on 04-01-2021

Signature of Chairperson (OEB)	Signature of External Examiner	Signature(s) of Thesis supervisor
Date: 06.01.2021	Pradipta Bandyopadhyay Date: 06.01.2021	Date: 04-01-2021

Signature of PSPC Member #1	Signature of PSPC Member #2	Signature of Convener, DPGC
Date: 06-01-2021	Date: 06/01/2021	Date: 06-01-2021

Dr. Biswarup Pathak
Signature of Head of Discipline
Date: 06.01.2021

Dedicated

to

maa

Acknowledgements

I am highly obliged to my thesis supervisor Dr. Satya S. Bulusu, for believing in me and molding me into a researcher. He has continuously motivated me to work with perseverance and optimism. The way to solve a problem with a never give-up attitude of him has led me to sail through this Ph. D. journey. I am grateful for his patience during my hard times.

I would like to thank my PSPC members Dr. Manavendra Mahato and Dr. Anjan Chakraborty for their optimistic criticism and valuable inputs.

I am very thankful to IIT Indore for providing me the server facilities to do my theoretical research work. I would also like to acknowledge the IT team (Dhiraj sir, Subbu, Yogendra sir) of IIT Indore for helping me out in all sorts of technical troubles.

I am sincerely thankful to Ministry of Human Resource Development, Govt. of India and Council of Scientific and Industrial Research, Govt. of India for providing me the fellowship to pursue the research work.

I would like to thank my first labmate Dr. Siva Chiriki for teaching me some valuable hacks for programming, without which the initial days in the Ph. D. would have been hard. Also, I would like to thank Sourabh Kumar for helping me out in solving software issues in the server along with theoretical discussions.

I would like to thank my friends without whom this journey wouldn't have been so smooth. All the tea breaks, mall trips, cooking, dancing, campus wandering, cycling, playing badminton, with Sayan, Lichchavi, Nivedita, Komal, Kritika, Dr. Usha Udaar, Ramana, Abhishek will be

the most memorable part of this Ph. D. life.

I would also like to acknowledge Vikas Soni, Aniket Mandal, Shubham Rawat and Mukti Jadon for filling the lab with fun during their one year of project in the lab.

In the end, I would like to thank my Parents for having faith in me and supporting me throughout this life changing journey. A special thanks to my mom (Mrs. Anita Jindal) who in the first place encouraged me to move out of my comfort zone and go for the Ph. D. journey. Her patience of five years has been commendable. If it was not for her, I wouldn't have gone for Ph. D. I am also thankful to my Badebhaiya (Dr. Abhishek Jindal) for being a solid support throughout my Ph.D. He helped me in understanding the essential aspects of Ph.D. along with discussions about my research problems. A special thanks to my husband Dr. Sayan Chaudhuri for always being by my side through all the thick and thin time of Ph.D. His company as a fellow Ph. D. researcher made my journey a very relaxing and joyful one. I would like to thank my dear friend Dr. Bharti Gupta for always supporting me in all my ventures. Thank you God for everything!

(Shweta Jindal)

Abstract

Machine learning has the ability to solve a problem which is beyond the processing of a human brain. The learning and the processing of data by a machine provides different connections present within a database. Artificial neural network (ANN) is one of the robust machine learning technique that mimics the learning process of a human brain using the basics of a perceptron model. In the last few decades, ANN has been used to solve complex problems in chemistry. The calculation of potential energy surface (PES) of a nanoparticle (Np) is one such problem which can be solved using ANN. The ab initio methods can be applied for accurate prediction of PES, but their high computational cost makes them a poor alternative. ANN provides a solution to bridge the gap between accuracy of ab initio methods and low computational costs. ANN interatomic potentials provides a cheap and accurate alternative to study the structural dynamics of metallic Nps. Metallic Nps have a variety of applications which makes them an important topic to study theoretically. The study of structural dynamics of Nps leads to major insights into vacancy defects, surface energy, mechanical properties, plasmon-resonance behavior. In this thesis, the ANN interatomic potentials is constructed for gold Nps and their alloys. As gold shows a rugged PES due to relativistic effects, the fitting of PES was possible with high dimensional ANN. For constructing a PES using ANN, one of the important part is the descriptors of the atomic environment. Higher order invariants- Power Spectrum and Bispectrum have been applied with modified atomic environment density for describing the atomic environments. A transferable approach for fitting PES of an alloy system was not done prior to the work done in this thesis. For an alloy system, the PES is fitted using a single ANN by following a strategy of decoupled fitting of energy and forces. The elements are differentiated between each other using weightings in the descriptors. The PES fitted for small and medium sized clusters($\sim$1.8 nm) is found to be transferable to larger size clusters($<$3.3 nm). The computational time for accurate calculation of energy and forces using power spectrum-ANN for a Au_{147} cluster was reduced to seconds,

when compared to DFT ($\sim$ hours) (calculation done on parallelized 8 CPU [GenuineIntel 2600.0 MHz]). Due to an accurate prediction of PES of gold Nps, a symmetric core evolution with increase in size of gold Nps is studied. It is observed that an icosahedron core is evolving from Au_{160} to Au_{327} to Au_{571}. It is also observed that magic number clusters- Au_{147}, Au_{309}, Au_{561} and Au_{923} prefer amorphous structure over symmetric structures. The unusual bonding in gold leads to modification of the structural preference in magic number clusters. Overall, the proposed descriptors and various new models have proved to be of great significance in fitting the PES of complex system like gold.

PUBLICATIONS

List of Publications:

Publications included in this thesis:

1. **"Structural Evolution in Gold Nanoparticles using Artificial Neural Network based Interatomic Potentials"**
   S. Jindal and S. S. Bulusu, J. Chem. Phys. **152**, 154302(2020).

2. **"A transferable artificial neural network model for atomic forces in nanoparticles"**
   S. Jindal and S. S. Bulusu, J. Chem. Phys. **149**, 194101 (2018).

3. **"An algorithm to use higher order invariants for modelling potential energy surface of nanoclusters"**
   S. Jindal and S. S. Bulusu, Chem. Phys. Lett. **693**, 152–158 (2018).

4. **"Spherical harmonics based descriptor for neural network potentials: Structure and dynamics of Au_{147} nanocluster"**
   S. Jindal, S. Chiriki and S. S. Bulusu, J. Chem. Phys. **146**, 204301 (2017).

Other Publications not included in this thesis:

1. **"Correlation of structure with UV-visible spectra by varying SH composition in Au-SH nanoclusters"**
   S. Chiriki , S. Jindal, P. Singh and S. S. Bulusu, J. Chem. Phys. **149**, 074307 (2018).

2. **"cT phase diagram and Landau free energies of $(AgAu)_{55}$ nanoalloy via neural-network molecular dynamic simulations"**
   S. Chiriki , S. Jindal and S. S. Bulusu, J. Chem. Phys. **147**, 154303 (2017).

3. **"Neural network potentials for dynamics and thermodynamics of gold nanoparticles"**

S. Chiriki , S. Jindal and S. S. Bulusu, J. Chem. Phys. **146**, 084314 (2017).

Conference Proceedings:

1. Poster presentation titled, "A transferable artificial neural network model for atomic forces in nanoparticles," in *Theoretical Chemistry Symposium*, Feb 2019, organised by Birla Institute of Technology and Science, PILANI.

Contents

Figures

Tables

List of Abbreviations

ML	Machine learning
Np	Nanoparticle
NN	Neural network
ANN	Artificial neural network
PES	Potential energy surface
DFT	Density functional theory
ADF	Atomic density function
SWE	Schrödinger wave equation
SAS	Searching amorphous structure
GM	Global minimum
MD	Molecular dynamics
SC	Single component
MC	Multi component
BH	Basin hopping
KF	Kalman filter
L-BFGS	limited memory Broyden–Fletcher–Goldfarb–Shanno
LEMA	Levenberg–Marquardt
LM	lowest minimum
Ih	Icosahedron
Oh	Octahedron
Dh	Decahedron
RMS	Root mean square
MEAD	Modified exponentially weighted descriptors
AEI	Atomic equivalence index

Chapter 1

Introduction

1.1 Machine Learning

"Learning" is an integral part of human life. It helps us to grow in all aspects of life. One of the important branch of learning is utilizing the learned information in analyzing different situations. For example, based on the taste acquired for categories- sweet, salty and sour food we can predict the category for a new food item even before tasting it. There are many situations where we are unable to process the information and use it for our benefit. For example, predicting the weather, prices of stocks, preventing frauds. If we are cheated by a company and next time we want to invest in a new company, we won't be able to identify the credibility of this new company. In such situations, we require a technology by which we can process the information and obtain a clarity. One more example of such a situation is filtering of spam mails. The spam mails are filtered based on the keywords they contain. Sometimes, spam mails do not have those keywords and in such cases we require a mechanism by which the mails are filtered by analyzing its content smartly. This kind of learning, processing, filtering and prediction can be achieved by "Machine learning"(ML). ML is learning from a bunch of data and making predictions for the unseen data. The word "Machine" broadly refers to the computer on which such programs can be constructed. So, it is a computer which will learn and process the data. Around 60 years ago, the computer used to perform the task that humans used to code. Now, the computer analyses the data and interprets the results on its own. The ability of a "machine" to perform

like humans is called artificial intelligence.

The ML forms an important part of our daily life. It analyses the data and categorize it according to the pros and cons associated with a situation. It helps in classification and predictions. A lot of activities like getting suggestions about our likes and dislikes, recognizing people with same accuracy as humans, pattern detection in videos, categorizing mails as spams, predicting the cost of a property, chances of winning, are governed using ML. ML can be achieved by different algorithms which can be broadly classified as supervised learning and unsupervised learning. Supervised learning is a learning based on input-output pairs i.e., the data having the input features leading to an output result is trained by an algorithm. For supervised learning there are many training algorithms like linear regression, support vector machines, nearest neighbor, neural networks (NN), naive Bayes and logistic regression. In unsupervised learning, the output is not considered. The algorithms extract the patterns from the data based on the input features. Unsupervised learning is broadly achieved by a method known as clustering.

ML has given an insight deeper than human perceptions. The hypothesis and solution generated by a human brain is unable to take into account a lot of hidden features of a problem. ML based data analysis has brought a revolution in various fields like protein structural analysis[1], genomics[2], prediction of volcano eruption[3], discovery of new materials[4], among many others.

For discovery of new materials, ML extracts the patterns of the structural preference of atoms in a stable structure and thus predicts new structures accordingly. This can be achieved by supervised as well as unsupervised learning algorithms. In general, among supervised learning, NN have proven to be robust for extraction of patterns in scientific data analysis. In this thesis work, NN have been applied to study structural analysis of gold Nps.

1.1.1 NN model

As the name suggests, NN is the network of neurons in the nervous system of the human body. This network is responsible for various actions like detection of smell, feeling of pain, learning new things among many others. In 1943, McCulloch and Pitts[5] deciphered the neural activity in the human brain by a simple mathematical model. They explained the working of neurons in transmitting the signal from one part to another part in the body. This was the first "NN" mathematical model drawn from electrical circuits. In 1949, Donald Hebb[6] wrote a book "The Organization of Behavior", describing the learning process of the human brain. He gave a theory that the link between two neurons is strengthened as a signal is transmitted. The theories by McCulloch, Pitts and Hebb laid the foundation for applying NN model for learning real life problems and doing accurate predictions. In 1958, Rosenblatt[7] proposed the "perceptron" model. It is a model by which artificial neurons can learn in a supervised learning mode. Supervised learning is learning from a data having information of all the input-output pairs. In 1959, Arthur Samuel utilized the learning capability of a NN and coded a program for a game - Checkers[8]. It taught the game to learn on its own and to play it efficiently. This was the first computer game that could defeat a human brain. In 1960, Wildrow and Hoff[9] constructed a single layer artificial NN called ADALINE. They even constructed MADALINE, that consists of multiple ADALINE units. These were implemented to filter the noise in phone lines and is still in use. After 40 years of the breakthrough by McCulloch and Pitts, in 1980s the layers of neurons was increased from a single to a double layer. This was introduced to induce a slow learning and a better pattern classification. In 1982, Hopfield[10, 11] introduced the nonlinear link between the input from all the neurons received by a neuron and the output sent to the other neurons. The NN emerged as a fascinating tool with the predictions of secondary structure of protein in late 1980s[12, 13, 14], protein localization[15], predictions of cleavage sites[16], spectral data analysis[17, 18], solving Schrödinger wave equation

(SWE) for harmonic oscillator[19, 20], prediction of polymer properties[21], prediction of heat of formation[22], fitting the PES[23, 24, 25, 26], Monte Carlo simulations of polymers[27], among many others[28].

In this thesis work, fitting of PES is achieved using ML. The PES represents the variation of energy of a system with different atomic coordinates and thus provides an important piece of information for a chemical system. In 2007, Behler and Parrinello[29] made a breakthrough in fitting the PES of molecular systems. They addressed and removed the shortcomings of the previously followed approaches for fitting the PES. The Behler-NN is a two layer feed forward NN having the capability of fitting and reproducing high quality of ab initio results. It captures all the interactions of the system efficiently and a proper modeling of the interactions is not required. Their strategy was to map the Cartesian coordinates of the system into local atomic environment features. These features are then given as an input to NN, which then gives the atomic energy as the output. This energy approximation is then corrected by supervised learning from a data obtained from ab initio calculations. This approach motivated other scientists to work on generating PES more efficiently. Since 2007, various techniques using different kinds of fitting strategies have emerged as a powerful tool to generate PES or preferably called interatomic potentials[30, 31, 32, 33, 34, 35, 36, 36, 37]. Such techniques are widely known as "ML". I will be discussing the interatomic potentials in the next section. The advantage of these ML techniques is that they are not formulated on a specific model based on the atomic or electronic interactions. The fundamental idea of ML is to describe the property of interest in the form of a mathematical expression depending upon large number of tunable parameters. The parameters are adjusted with respect to the quantum chemical data fed into the "machine". The word "machine" refers to a pattern classification tool that captures and classifies the input data. It further processes the data into the desired output. The outline of the construction of a PES using an ML technique is followed by the brief introduction about interatomic potentials in the next section.

1.2 Interatomic Potentials

Various chemical processes like surface reactions, catalysis, synthesis can be explained by a thorough scanning of atomic interactions. The basic quantity that reflects atomic interaction is energy and atomic forces in a molecular/atomic system. The correct evaluation of these quantities leads to an accurate pathway, structural stability and mechanisms of reactions. The potential energy of a molecular/atomic system is dependent on interatomic interactions and therefore interatomic potentials calculate the potential energy by using mathematical equations.

The ab initio methods are the most accurate form of interatomic potentials. They estimate the energy and forces by solving the SWE for N-electrons of a molecular system. In order to estimate the PES, large amount of simulations are required which in turn requires calculation of energy and forces. The computational burden is huge if ab initio methods are employed for the energy and force calculation. Therefore, a classical approach is required for accurate estimation of the PES. The electronic structure calculations can be replaced by atomic level calculations for the estimations. One of the popular and a basic form of potential for diatomic molecules and noble gases was proposed by Lennard-Jones[38] and Morse[39]. These potentials rely on the additive nature for a multi atomic system. Since the interactions are not generally additive, the pair potentials are unable to perform as the number of atoms increases. For multi atomic systems, many pair potentials were introduced as Gupta potential[40], Embedded atom method[41, 42], Murrell Mottram potential[43], Finnis-Sinclair potential[44], force fields[45, 46, 47], reaxFF[48, 49] among many others. All these empirical potentials have a rigid mathematical modeling of the atomic interactions which may work for a few systems only. To overcome the modeling of atomic interactions, ML techniques are employed for predictions of energy and forces.

As discussed in previous section, ML techniques do not require a rigid physical connection between the input and output. They learn the

data and extract the patterns by which the atoms interact in a molecular system. Overall, there are four elements that comprises an ML technique for construction of interatomic potential(Fig. 1.1).

- Generate an input dataset consisting of different atomic arrangements.
- Extract the features from the input dataset in terms of local atomic environments, commonly called as descriptors.
- Feed the descriptors into a pattern recognition/classification "machine".
- Train the machine till the parameters are finely tuned with respect to the atomic system.

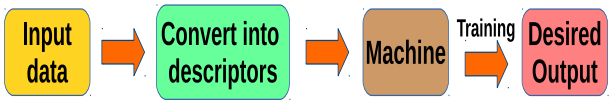

Figure 1.1. An overview of ML technique

The input dataset for ML technique should consists of all kinds of atomic environments that are feasible in actual practice. The structures can be obtained using different simulations like molecular dynamics (MD) and Monte Carlo using either empirical potential or ab initio potential as the interatomic potential. The following step is to extract the features of the dataset such that the "machine" is able to recognize minute details about the bonding and interactions in the atomic system. Fundamentally, a descriptor should be unique for each environment. It should be rotationally, translationally and permutationally invariant. There are many descriptors which are listed in the literature and can describe the atomic systems. For example, Behler's symmetric function[29, 50], SOAP kernel[51, 52], coulomb matrix[53], fingerprints[54], SNAP[55], embeddings[56], encoder[57, 58], wavelets[59, 60] can efficiently map the atomic environments. After mapping the input dataset to descriptors, a fitting technique is chosen. The

widely used fitting techniques can be broadly classified into NN and kernel based methods.

The architecture of NN based methods use multiple layers of neurons, and transfer the information from one layer to another by using weights. The weights capture the hidden information from the descriptors and fit them according to the desired output. The interatomic potential using NN based methods are usually referred to as NN potential. In the last decade, a lot of NN potentials have been developed using different architecture and for different molecular systems[30, 33, 61, 62, 63]. The variety of NN used are feed forward NN[29, 64], deep tensor NN[37], SchNet[65], graph NN[66], graph convolutional network[67], message passing NN[68] among many others. Kernel based methods[69, 70] uses a similarity function to compare any two data points in the input data. There are a lot of kernel based methods like support vector machines[71, 72], ridge regression, gaussian process ridge regression[51, 52], principal component analysis among others.

After the data is sent into the "machine", the learning/tuning of the parameters is achieved using different optimization algorithms like limited memory Broyden–Fletcher–Goldfarb–Shanno (L-BFGS)[73], Kalman Filter (KF)[74, 75, 76], Levenberg Marquardt (LEMA) algorithm[77], back propagation[78], gradient descent[79], Adam optimizer[80]. The optimization algorithm minimises the error between the actual and the predicted values by modifying the network weights. The optimization is done iteration wise, and the learning is stopped with the decrease in the error of prediction. The optimized parameters are then applied for predictions for a wide range of dataset.

1.3 Higher order invariants

For capturing the effect of atomic movements in crystals and liquids, Steinhardt[81, 82] proposed the use of bond orientational order parameters. The bond order parameters are second order(Q) and third order(W)

invariants of spherical harmonics. For an atom i in an N atom molecule, the higher order invariants- Q and W are defined for a particular frequency l of spherical harmonics as

$$Q_l^i = \left(\frac{4\pi}{2l+1} \sum_{m=-l}^{l} Q_{lm}^{i*} Q_{lm}^i \right)^{\frac{1}{2}} \tag{1.1}$$

$$W_l^i = \sum_{m_1,m_2,m_3=-l}^{l} \begin{bmatrix} l & l & l \\ m_1 & m_2 & m_3 \end{bmatrix} Q_{lm_1}^i Q_{lm_2}^i Q_{lm_3}^i \tag{1.2}$$

where, Q_{lm}^i is calculated using spherical harmonics where r_{ij} is length vector pointing from atom i to atom j.

$$Q_{lm}^i = \frac{1}{N} \sum_{i \neq j}^{N} Y_{lm}^j(\hat{r}_{ij}) \tag{1.3}$$

These higher order invariants have been applied in various applications like phase transitions[83, 84], free energy of clusters[85, 86] and in interatomic potentials[87]. The property of being rotationally and translationally invariant makes them highly efficient for describing atomic environments. The power spectrum[52] and bispectrum[88] coefficients forms the set, of which the Q and W are subset. These coefficients are discussed in next chapter. These coefficients have efficiently been applied to as atomic environment descriptors in the past few years. In this work, power spectrum and bispectrum coefficients have been modified and applied for constructing the PES of metallic Nps.

1.4 Metal Nps

Nps are the particles in the size range of 1 nm to 100 nm. They have unique properties and are extremely efficient in performing a lot of applications. Metallic Nps are the Nps of metals like gold, copper, silver, platinum, rhodium, sodium. In 5^{th} century B.C. when the Lycurgus cup was created using colloidal gold, the word "nano" was not known[89]. In 16^{th} century,

glazes composed of silver and copper Nps were reported. The glass makers in ancient times produced various colored stains using tiny amounts of silver and gold. In 1676, a drinkable gold solution was used to cure diseases. The solution contained gold which was not visible to human eyes. In 1685, a recipe for synthesizing coloring pigments was given by Cassius, known as Purple of Cassius[90]. In 1794, dying of silk was done with colloidal gold solution. It was in 1857, when Faraday discovered the Nps of metal in a solution[91]. This was supported by Mie in 1908[92], who showed the optical properties of metal Np. Metal nanoclusters are the clusters where the number of atoms that form a stable structure are in range of 2 to $\sim$100 atoms, leading to a size below $\sim$1 nm.

The Nps have evoked considerable attention due to quantum size effects and surface to volume ratio, that leads to a tremendous amount of applications in various fields. The properties showed by metal nanoclusters are a function of number of atoms and their structural arrangement. A slight change in the structural morphology leads to modification in the property of interest. For clusters having multiple species, the composition of the atomic species also has an impact on the properties of the nanocluster.

At the bulk level the atomic properties overlap with each other making the energy levels continuous. The valence electrons act like a free electron gas as the number of electrons are huge. As we go to nanoclusters, the atoms do not overlap with each other and thus the energy levels becomes discrete. The valence electrons do not behave as a free electron gas as the electrons are countable at such small size and have an impact on the properties. The clusters thus exhibits a quantum size effect leading to a gap in HOMO-LUMO. This gap results in tunable optical properties of the nanoclusters. As the size decreases from bulk to atomic level, the number of surface atoms increases with comparison to the atoms present in the core. This increase in the surface to volume ratio increases the reactivity of the clusters[93]. The magnetic moment increases due to large number of surface atoms. The low coordination of the surface atoms makes them

catalytically active.

All the above said properties motivates to study the metal nanoclusters. In this work, the focus of study is on gold and its alloys nanoclusters. Gold nanoclusters exhibits an added effect called relativistic effects[94, 95, 96, 97, 98]. The electrons in the heavy elements move at a higher speed causing relativistic effects which leads to alteration of properties.

1.4.1 Gold nanoclusters

Among metals, gold is known as an inert and a noble metal. This is attributed to its ability to stay anti-corrosive and non-reactive in the bulk state. One of the reason for inertness is relativistic effects, which stabilizes the valence electron ($6s^1$) and makes it difficult to react. As we go from bulk to nanometer level, gold becomes highly reactive and is found to have applications in catalysis[99, 100, 101, 102, 103, 104, 105], biosciences[106, 107] and radiosensitizer[108]. The changes occur at the nanometer level due to surface to volume ratio, more active sites and different electronic structure. In surface reactions like catalysis, the defects on the surface of the gold Nps becomes the active sites for reaction to take place. Among Nps, it is observed that, there is a decrease of catalytic activity with a decrease in the percentage of surface atoms. Gold nanoclusters are known to exhibit a wide variety of structures[31, 109, 110, 111, 112, 113] like planar(Au_{11}-Au_{13})[114], cages(Au_{16}-Au_{18})[115], pyramidal(Au_{20})[116], tubular(Au_{21}-Au_{24})[117] and amorphous core-shell($>Au_{33}$)[31, 112, 113, 118].

For establishing a proper structure dependent physical and chemical activity, it is important to study the structure evolution and thermodynamic stability of these clusters. It has been observed that catalytic activities in gold Nps becomes inactive for sizes greater than 5 nm.[98, 102, 105, 119, 120] It is very important to study the catalytic activity of gold Nps below 5 nm using electronic structure methods.

Metallic Nps belonging to the magic number series[121, 122] with

atoms – 13($\sim 0.6\ nm$), 55($\sim 1.2\ nm$), 147($\sim 1.8\ nm$), 309($\sim 2.2\ nm$), 561($\sim 2.7\ nm$) and 923($\sim 3.3\ nm$) are expected to have a symmetric structure (like icosahedron (Ih), decahedron (Dh), octahedron(Oh)). They are called "magic" because of a compact arrangement of atoms leading to a stable symmetric structure. They are also known to be more stable and possess different reactivities[119, 120, 123, 124, 125, 126] than clusters of other sizes. Although, gold is a metal, many studies have shown that, the magic numbers for gold Nps may not exhibit symmetric structure as the lowest energy structure. Among these, Au_{13} and Au_{55} have been proved to have a non-symmetric stable structures in the previous years[98, 111, 127, 128, 129, 130, 131, 132, 133] and recently Au_{147} has been proved to have an amorphous structure[134, 135, 136].

Due to large variations in the structures and chemical reactivities, it is important to study the structural dynamics of these clusters. This is possible by exploring the PES and getting the low energy stable structures.

1.5 Objectives of the study

In order to study metallic nanoclusters we have to run Monte Carlo or MD simulations. This requires the calculation of energy and forces by density functional theory (DFT) for all the structures as the simulation is processed. For larger systems (>100 atoms), it is almost impossible to carry out simulations using DFT as this will be highly computationally expensive. On the other hand, empirical potentials like the Gupta potential, Morse potential, Murrell–Motram potential, EAM, and MEAM have been time and again used for the prediction of energy and forces. It has been observed that for heavy atomic systems, like gold and platinum, relativistic effects play an important role and therefore the empirical potentials are unable to make an accurate prediction of the structure and properties of these systems. So, we have to construct an interatomic potential having an accuracy of DFT and a speed of empirical potentials using ML. ANN is one of the robust platform to construct PES of complex molecular systems. To

get a deeper insight into the structural dynamics of metallic nanoclusters, especially gold and its nanoalloys, different strategies are proposed in this thesis work. The computational burden for calculating the properties of large size Nps from DFT is very high. In this work, ANN is applied to reduce the computational cost for large size Nps using different atomic environment descriptors.

1.6 Framework of the Thesis

The thesis is arranged in seven chapters. The current chapter gives a brief history of ML techniques, metallic clusters, interatomic potentials and atomic environment descriptors.

Chapter 2: It provides the details of theoretical foundations laid in this work. The developments done in the existing theoretical models is elaborated. The basic framework of constructing an ANN potential is discussed.

Chapter 3: In this chapter, PES of gold nanoclusters up to a size of $\sim$ 1.8 nm (Au_{147}) is constructed. The radial functions and modified Power Spectrum coefficients are used to describe the atomic environments. An elaborated study of structural dynamics of Au_{147} is performed. A comparative analysis between DFT and ANN results is done.

Chapter 4: This chapter provides the details of construction of PES using filtered bispectrum coefficients as atomic environment descriptors. The model is applied to gold nanoclusters and a comparison is done between Power Spectrum coefficients and Bispectrum coefficients driven results.

Chapter 5: It presents the demonstration of the technique to model the interatomic potentials of alloys using ANN. The proposed strategy is applied to fit the PES of $(AgAu)_{55}$-$(AgAu)_{147}$ nanoalloys and $Au_{13}(SH)_6$-$Au_{38}(SH)_{24}$ nanoclusters. The transferable and computationally cheap strategy can be applied to any number of chemical species system.

Chapter 6: This chapter contains the structural evolution of gold nanoclusters from a few atoms to nanometer size range. A nucleation of a symmetric core is identified with an evolution up to $\sim$ 3.3nm. A new set of

magic numbers is identified for gold and a probabilistic study is performed to compare experimentally and theoretically obtained results.

Chapter 7: This chapter gives a conclusion and the future scope of the work done in thesis.

Chapter 2

Theoretical foundation and developments

2.1 Electronic structure calculations

The basic foundation of all the entities around us is an atom. An atom is made of electrons, protons and neutrons. The properties of any chemical system is thus governed by the electronic interactions. An electron is represented accurately by quantum mechanics. The state of a system is represented by wave function. Solutions to the SWE are the possible energies and wavefunctions of a system. From a wavefunction, one may calculate the properties of a system. The time independent SWE is given as

$$\hat{H}\psi(\mathbf{r}) = E\psi(\mathbf{r}) \tag{2.1}$$

The wave function ψ is dependent on electronic and nuclei positions in the space. According to Born-Oppenheimer approximation[137], the electronic and nuclei time scales are different and thus the wave function can be separated into ψ_e and ψ_n, respectively. The Hamiltonian operator consists of kinetic energy and potential energy contributions to the total energy. For a multi-electron system (n_e) with n_n nuclei, SWE is written as

$$H_e\psi_e = E_e\psi_e \tag{2.2}$$

$$(-\frac{1}{2}\sum_{i=1}^{n_e}\nabla_i^2 + \sum_{i<j}\frac{1}{|r_i - r_j|} - \sum_{i=1}^{n_e}\sum_{i_N=1}^{n_n}\frac{Z_{i_N}}{r_{i_N} - r_i})\psi_e = E\psi_e \tag{2.3}$$

The exact solution of SWE is not possible for multi-electron system due to the inter electronic repulsion term. It is impossible to solve for an optimized wave function that will give an accurate ground state energy and other properties. In order to get an accurate solution, the wave function has to be dependent on all the electronic coordinates at once, which is not possible to formulate. Since, electrons are fermions, they should follow anti symmetry rule for exchange. Slater determinant[138] takes anti symmetry in consideration and is a better way to approximate wave functions. Hartree-Fock(HF) theory provides a solution to this problem by using Slater determinant orbitals to calculate the ground state properties. The HF equation for i = 1,2,..,$N_{electron}$ modifies to

$$F_i\phi_i = \epsilon_i\phi_i \tag{2.4}$$

where, ϕ are spatial orbitals and F_i is the Fock operator of i^{th} electron given by

$$F_i = -\frac{1}{2}\nabla_i^2 - \frac{Z}{r_i} + \sum_{j}^{N_{electron}} (J_j(i) - K_j(i)) \tag{2.5}$$

J_j is the coulomb operator and K_j is the exchange operator. The HF theory has spin correlation taken care of by Slater orbitals, but coulomb correlation is missing. The shortcomings of HF theory is that, it cannot explain electron correlation. Moreover, using single Slater determinant it is difficult to explain the bond forming and the bond breaking in molecules. Hohenberg-Kohn(HK) proposed DFT using electron density as the fundamental quantity. Electron density is a simple quantity that depends only on coordinates- x, y, z rather than a complicated wave function that depends on all the electronic coordinates. The DFT is discussed in brief in the next section. In this work, all the electronic structure calculations are performed using DFT.

2.1.1 DFT

DFT bypasses the calculation of all the ground state wave n-electron functions. It calculates the electronic energy from the ground state electron density(ρ(r)). According to HK theorem[139], the ground state of a multi-electron system is a unique functional of the electron density ρ(r). The electron density is calculated from the wave functions as the integral over product of all the n electron wave function. On integrating the electron density, we can get the total number of electrons.

$$N_{electron} = \int \rho(\mathbf{r}) d\mathbf{r} \tag{2.6}$$

$$\rho(r) = N_{electron} \int ... \int \psi^*(r_2, ...r_{N_{electron}}) \psi(r_2, ...r_N) dr_2 ... dr_{N_{electron}} \tag{2.7}$$

The energy functional is defined as[140]

$$E[\rho(\mathbf{r})] = \int V_{ext}(\mathbf{r}) \rho(\mathbf{r}) d\mathbf{r} + F[\rho(\mathbf{r})] \tag{2.8}$$

$V_{ext}(\mathbf{r})d\mathbf{r}$ is the contribution from Coulomb interactions of electrons with the nuclei. The kinetic energy and inter-electronic interactions are represented by $F[\rho(\mathbf{r})]$. Variational method gives the ground state energy, which corresponds to a ground state density. Due to the constraint of number of electrons on the electron density, Lagrange multiplier($-\epsilon$) is introduced for minimizing the energy.

$$\frac{d}{d\rho(\mathbf{r})} \left[E[\rho(\mathbf{r})] - \epsilon \int \rho(\mathbf{r}) d\mathbf{r} \right] = 0 \tag{2.9}$$

Since, HK theorem was proposed for a system of interacting electrons, the total energy approximation was not that accurate. Kohn-Sham(KS) proposed a solution for accurate approximation of energy of the electrons. They approximated the functional $F[\rho(\mathbf{r})]$ by taking contributions from kinetic energy, electron-electron coulomb interaction and exchange correlation. The kinetic energy term is the energy of a fictitious system having non-interacting electrons having the density of interacting electrons. The

exchange correlation energy functional $E_{XC}[\rho(\mathbf{r})]$ contains the contribution due to exchange-correlation and the difference between the real kinetic energy and the fictitious system kinetic energy. The KS equation for energy can be written as

$$E[\rho(\mathbf{r})] = \sum_{i=1}^{N_{electron}} \int \psi_i(\mathbf{r}) \left(-\frac{\nabla^2}{2}\right) \psi_i(\mathbf{r}) d\mathbf{r} + \frac{1}{2} \int \int \frac{\rho(\mathbf{r}_1)\rho(\mathbf{r}_2)}{|\mathbf{r}_1 - \mathbf{r}_2|} d\mathbf{r}_1 d\mathbf{r}_2 +$$

$$E_{XC}[\rho(\mathbf{r})] - \sum_{v=1}^{N_{nucleus}} \int \frac{Z_v}{|\rho(\mathbf{r}) - R_v|} \rho(\mathbf{r}) d\mathbf{r} \tag{2.10}$$

The non interacting one electron orbitals are squared and summed for calculating the KS density.

$$\rho(\mathbf{r}) = \sum_{i=1}^{N_{electron}} |\psi_i(\mathbf{r})|^2 \tag{2.11}$$

The simplified form of KS equation is written as

$$\left[-\frac{\nabla_1^2}{2} + V_{effective}(r_1)\right] \psi_i(\mathbf{r}_1) = \epsilon_i \psi_i(\mathbf{r}_1) \tag{2.12}$$

$$V_{effective} = \left[- \left(\sum_{v=1}^{N_{nucleus}} \frac{Z_v}{r_{1v}} \right) + \int \frac{\rho(\mathbf{r}_2)}{r_{12}} d\mathbf{r}_2 + \left(\frac{dE_{XC}[\rho(\mathbf{r}_1)]}{d\rho(\mathbf{r}_1)} \right) \right] \tag{2.13}$$

Details of the DFT calculations

In this work, the DFT calculations are performed in Vienna Ab initio simulation package[141, 142, 143, 144](VASP). The electron orbitals are represented with a plane wave basis set. The full electron wave function is reduced by using projector augmented wave method (PAW)[145]. It treats core electrons and nucleus as a single entity and the valence electrons separately. The valence electrons are given by a set of pseudo wave functions having fewer nodes. The exchange correlation functional is approximated by generalized gradient approximation through Perdew-Burke-Ernzerhof (PBE) functional[146, 147]. The PBE functional gives accurate approximations for metallic clusters. Many studies have been

reported that validates the results obtained using PBE functional with experiments[115, 148, 149, 150, 151, 152]. The atomic systems considered in this work are non periodic, therefore, a gamma k point mesh of 1×1×1 is used. The cut off energy used for the clusters is 260 eV, and the gradient convergence is 10^{-4}. For a non periodic system like isolated atomic clusters, the cluster is kept in centre of a periodic cell. The length of the periodic cell should be enough for the cluster to not react between each other as shown in Fig. 2.1. The cubic box length for different size of clusters is kept by adding ~ 8 $\mathring{A}$ to the diameter of the cluster. This allows for a negligible interaction among molecules in neighboring cells.

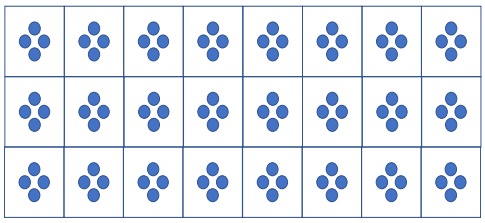

Figure 2.1. A periodic cell for a non-periodic isolated cluster

2.2 Empirical Potentials

Empirical potentials are mathematical functions that approximate the potential energy of a N-atom system. These potentials vary from taking two-body interactions to multi-body expansion terms. The parameters corresponding to different systems are fitted for a dataset, which is then applied for calculations. These potentials are extremely fast when compared to electronic structure calculations and therefore, the aim of this study is to get an empirical potential having an accuracy of DFT, at a much cheaper computational burden. The empirical potentials used and constructed in this work are discussed below.

Table 2.1. Parameters of Gupta potential for Ag and Au

	A (eV)	p	r^0 ($\mathring{A}$)	ζ (eV)	q
Ag-Ag	0.1028	10.928	2.892	1.178	3.139
Au-Au	0.2061	10.229	2.884	1.79	4.036

2.2.1 Gupta Potential

Gupta potential[40, 153] is a many body potential for metallic clusters. Cleri and Rosato (1993) have calculated the parameters of Cu, Au, Pt, Ni, Ag and Pd using second-moment approximation of tight binding Hamiltonian. The potential is expressed as contribution from repulsive ($E_r(h)$) and attractive pair terms ($E_a(h)$).

$$E = \frac{1}{2}\sum_{h=1}^{N} E_r(h) - E_a(h) \tag{2.14}$$

$$E_r(h) = \sum_{h\neq k}^{N} A_{hk} e^{-p_{hk}\left(\frac{r_{hk}}{r^0_{hk}}-1\right)} \tag{2.15}$$

$$E_a(h) = \left(\sum_{h\neq k}^{N} \zeta^2_{hk} e^{-2q_{hk}\left(\frac{r_{hk}}{r^0_{hk}}-1\right)}\right)^{\frac{1}{2}} \tag{2.16}$$

where, N is the total number of atoms in the structure and r_{hk} is the bond between an atom 'h' and 'k'. p_{hk} is dependent on the atomic species, r^0_{hk} is the minimum distance with the first neighbor, ζ_{hk} is a hopping integral and q_{hk} reflects the dependence on interatomic distances. All these parameters (r^0_{hk}, p_{hk}, A_{hk}, ζ_{hk} and q_{hk}) are fitted according to the experimental data of lattice parameters, cohesive energies and elastic constants for a reference crystal structure at $0K$. In this work, Gupta potential is used for generating an initial dataset for the fitting of PES of Ag and Au. The parameters used are given in Table 2.1[153].

2.2.2 NN potential

An interesting approach to get an interatomic potential is by learning the patterns of bonding, instead of providing the contribution to the energy exclusively. This is achieved by ML techniques which have a mathematical form of predicting energy. The energy is formulated to be dependent on the atomic environments. The machine is trained in such a way that the patterns in which energy is related to the atomic environments is captured. The ML techniques have proven to be highly robust for fitting the PES of many atomic systems in the last decade. One such ML technique is NN, which is a neuron based model. In NN, the energy is predicted from the atomic environments using a network of neurons. It is inspired from the biological model of neurons, where the signals are transmitted from one point to another, resulting in brain activity as an output. One of the pros of using NN is that there are lot of parameters on which the energy can be modeled and thus the amount of complexity in the energy predictions can be taken care of easily. NN is used for the problems where the relationship between the entities is not known. By adjusting different parameters of the network, the relationship is extracted. The input and output is known, but the link between the two is explored using NN. The number of parameters on which an output depends can vary from one to many, according to the complexity of the problem. To develop a basic understanding about architecture of NN, few examples are discussed below[154].

A single neuron NN An example of a single neuron network is converting mass from Kilo to Pounds. The relationship between Kilo and Pounds is linear and that's why only a single neuron is required. In Fig. 2.2, we have an input of 10 Kg and an output of 22.05 Pounds. In order to find the relation between the two, a guess weight of 5 is applied. The output obtained is 50, which gives an error of 27.95. To reduce the error, a smaller value of 2 is taken. The error obtained is 2.05, which is considerably lower than the previous weight error. To further reduce the error, a number 2.2 is chosen. Now, the error is negligible, and it can be said that network

is fitted well to convert the mass in Kg to that in Pounds. The error can be made zero, if the weight is taken 2.205. This shows that a network is fitted with a weight of 2.205 for converting Kg to Pounds.

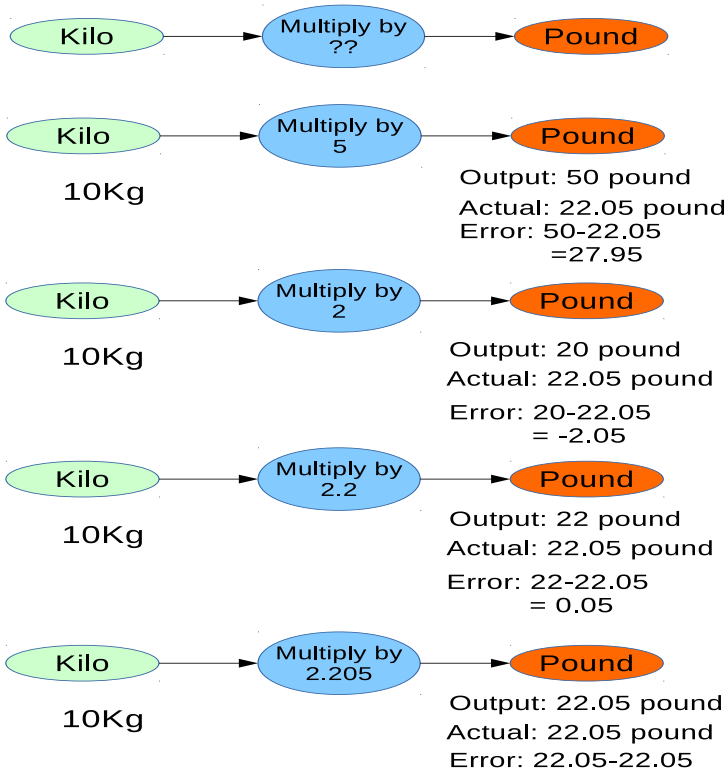

Figure 2.2. Fitting the single neuron network

A double neuron NN There are certain problems which cannot be solved using one neuron and thus, two neurons are required to make a relationship between input and output. For example, if we have to relate a human height and weight with the nutritional status, one neuron won't be able to draw a linear relationship. Now, two neurons are required- one for mapping height to nutritional status and one for mapping weight to nutritional status. Also, there has to be a link between the impact they each have on the relationship. As shown in Fig. 2.3, the two inputs- height and weight are related to the nutritional status by two neurons. The weights(w's) of each link carries the required information, leading to a consolidated output as the nutritional status.

A double layer NN The above problems are solvable by using a single layer of neurons between input and output. The purpose of using

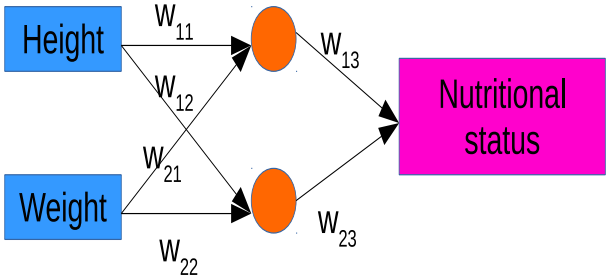

Figure 2.3. Fitting the double neuron network

NN is to solve much complex problems. For example, classifying a data in which the points cannot be classified by a single line as shown in Fig. 2.4. In this type of problem, the first layer of neurons helps to detect the basic difference between the two types of data points by drawing a line. The output from the first layer is not enough to make an accurate decision and thus, a second layer of neurons is applied. This layer captures the smoothness of the edges by which the data can be differentiated. In the output, it can be observed that one type of data is easily classified from the other type of data.

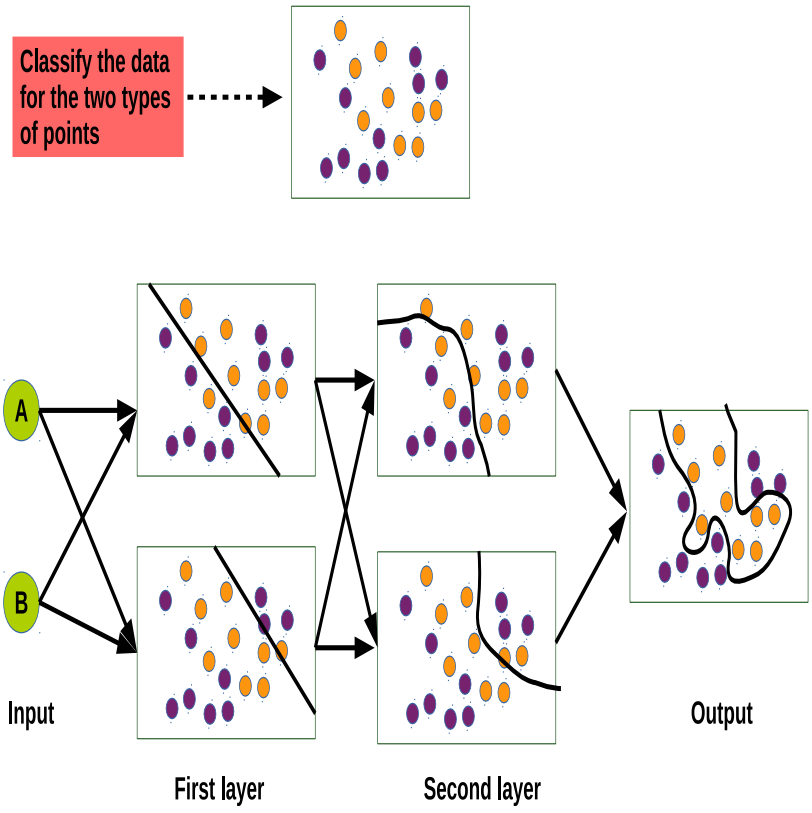

Figure 2.4. The double layer network

Biological NN The human brain consists of $\sim$ 80-90 billion neurons for transmitting the signals throughout the body. The basic structure of a neuron consists of dendrites, axon and terminals as shown in Fig. 2.5. A neuron receives the input signals from dendrites, which is then passed through axon till the terminals. These terminals are further connected to 100's of neurons, where this signal acts as the input. There are multiple layers of neurons through which a signal passes till an output is obtained. The neurons process the input signal and transmits it when a threshold is crossed. The input signal should have a high strength to trigger a neuron and pass the signal to another neurons. The need of so many neurons is to efficiently differentiate between the functions of different parts of human body along with the different sensations in the body. The artificial NN is inspired from biological NN to send the signals from input functions to an output via artificial neurons[5, 155, 156].

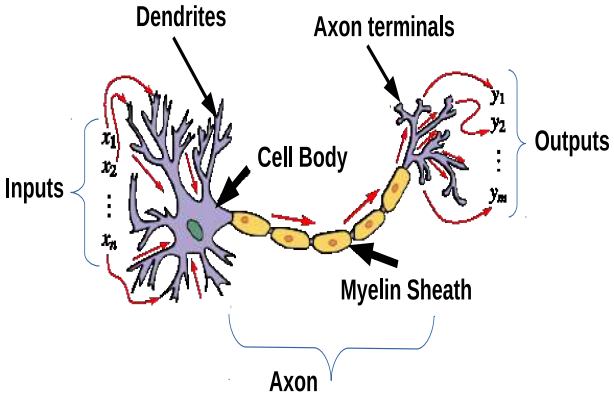

Figure 2.5. The structure of a neuron, Image courtesy: Wikipedia

The two characteristics of biological NN which are utilized in artificial NN are

- Taking multiple layers in the NN with large number of neurons in each layer.
- Taking a function that shoots up as the input value crosses a threshold thus acting as an artificial neuron.

An activation function like sigmoid function or hyperbolic tangent serves the purpose of processing an input to an output by keeping a threshold

into account[157]. For making the features interact among each other, two layers of neurons between input and output serves the purpose of solving complex non-linear problems using NN. Customizing the number of neurons depends on the classification of the input data.

Why NN to fit the PES of nanoclusters? The energy of a cluster depends upon the positions of atoms. We can map the individual atomic positions to the energy using a single layer of neurons. This type of model will give optimized parameters that can give the total energy. Such a model fails considerably if a structure is translated or rotated in the space leading to a change in atomic positions. The atomic positions should be replaced by a quantity which is rotationally and translationally invariant. The interatomic distance fits into this quantity and acts as a better input. As the interatomic distance of all the atoms is given as an input to NN, a fitting can be done using a single layer of neurons. The drawback of using interatomic distance is that a relative arrangement of atoms with respect to each other is not captured. To overcome this, for an atom, all the interatomic distances around it within a cut off distance is summed to give a density. This density is weighed with a gaussian function for taking the effect of interactions with a decrease in the interatomic distance. Since, the inputs are a summed function, they are separated by a hyperplane by the first layer of neurons. A second layer of neurons is now added to get the accurate shape of the atomic density. Therefore, in this work, a two hidden layer NN proposed by Behler and Parrinello[29] is applied. As shown in Fig. 2.6, the atomic environments are mapped to the descriptors. The information carried by them has to be processed in such a way that an accurate energy is predicted and the network learns the bonding patterns. For using NN, it is not relevant to know the functional form of the output dependence on the input functions of a system. The basic task consists of training a NN, by varying the biases of neurons and weights of connecting neurons so as to reproduce as accurately as possible the known energies and forces of a large number of atomic environments. The training should give a minimum error between the expected output and the predicted output.

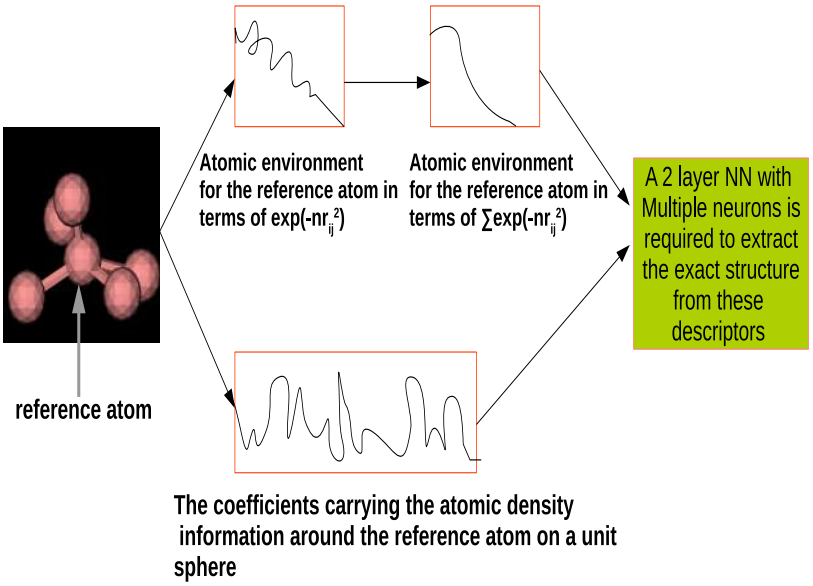

Figure 2.6. The conversion of structural information into the descriptors

As the training proceeds, NN captures the hidden patterns existing from input functions to yield the output. The NN architecture consists of input functions, hidden layers, bias weights and output. For a three atom system, a detailed NN architecture is shown in Fig. 2.7. In Fig. 2.7, for each atom the NN consists of 59 input functions, 5 neurons in hidden layer 1, 5 neurons in hidden layer 2 and one output. The outputs of the three atoms are summed to give the total energy of the molecule. The bias weights are given to each neuron of each hidden layer, respectively. All the components of the network are connected with each other through weights. In order to get the accurate predictions, the network is trained i.e. the weights are optimized till a convergence is achieved. In this work, the NN is applied to fit the PES of gold Nps and alloys of gold Nps based on a dataset consisting of DFT calculations. In 2007, Behler and Parrinello[29] proposed an atomic NN for fitting the PES of a system by mapping atomic environments to the total energy. Spherical harmonics based atomic environment descriptors[134] are used in this study to fit the energy of a cluster. The energy for an atom i is derived from the input functions P by following equation.

$$E^i_{atom} = \sum_{j=1}^{30} w^{23}_{j1}.f_j \left(w^b_j + \sum_{k=1}^{30} w^{12}_{kj}.f_k \left(w^b_k + \sum_{n=1}^{\text{input}} w^{01}_{nk}.P_{in} \right) \right) \qquad (2.17)$$

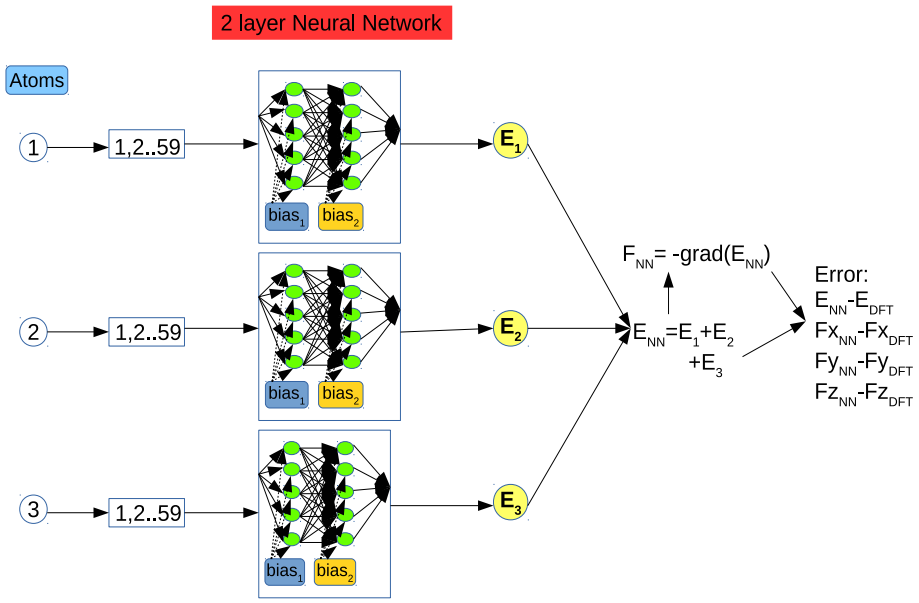

Figure 2.7. Feed forward NN architecture

Here, k and j are hidden layer 1 and 2, respectively. After a lot of trials with different number of neurons, the hidden layer neurons were kept 30 in each layer. This shows that 30 classifiers are required to separate the atomic environments. w_{nk}^{01}, w_{kj}^{12} and w_{j1}^{23} are the weights connecting neurons of input functions P to neurons of layer 1, neurons of layer 1 to neurons of layer 2 and neurons of layer 2 to single neuron of output, respectively. w_k^b and w_j^b are the weights for separately biasing layers k and j. f_k and f_j are the sigmoid function applied at the output of hidden layer 1 and 2, respectively for a non-linear dependence.

$$f_k = \frac{1}{1 + e^{-\left(w_k^b + \sum_{n=1}^{\text{input}} w_{nk}^{01}.P_{in}\right)}} \tag{2.18}$$

$$f_j = \frac{1}{1 + e^{-\left(w_j^b + \sum_{k=1}^{30} w_{kj}^{12}.f_k\left(w_k^b + \sum_{n=1}^{\text{input}} w_{nk}^{01}.P_{in}\right)\right)}} \tag{2.19}$$

The output obtained from DFT is the total energy of the system, therefore the total energy from NN is calculated as

$$E_{total}^{NN} = \sum_{i=1}^{atoms} E_{atom}^{i} \tag{2.20}$$

In order to explore the PES, accurate atomic forces are required and there-

fore from E_{total}^{NN}, the force for an atom i is calculated as

$$F_R^i = -\frac{\partial E_{\text{total}}^{NN}}{\partial R_i} = -\sum_{j=1}^{\text{atoms}} \frac{\partial E_j}{\partial R_i} = -\sum_{j=1}^{\text{atoms}} \sum_{n=1}^{\text{input}} \frac{\partial E_j}{\partial P_{j,n}} \frac{\partial P_{j,n}}{\partial R_i} \tag{2.21}$$

where R $\in$ {x,y,z} of atom $'i'$. The sensitivity in force predictions is high and therefore, along with energy, the forces are also fitted through the optimization of weights. The accuracy of fitting is measured by root mean square (RMS) error in energy and forces averaged over all the clusters in the testing set.

2.3 Optimization of NN weights and simultaneous fitting of energy and force

The NN is trained by optimizing the weights with respect to a decrease in the error between the predicted and the observed output. There are lot of optimization algorithms like back propagation[78], LEMA algorithm[77], Quasi Newton(QN) method[158], L-BFGS algorithm[73] and KF[74, 75]. In this work global extended KF is used as the weights optimization tool. The edge of KF over other algorithms is that KF is a very fast and robust optimization algorithm. The minimum amount of dataset required for PES fitting is around 10,000. The algorithms such as LEMA, L-BFGS computes the error for the entire dataset at once and optimizes it. Such an optimization takes a lot of time to converge and chances of lying in a local minimum is higher. On the other hand, KF optimizes the error for each data point and therefore the optimization is faster. The KF optimization is dependent on a error covariance matrix(P), hessian matrix(H) and error vector(δ). A stepwise procedure for weights optimization using KF is given as follows:

1. Initialize the NN weights as random numbers.

2. Set process noise (Q) and measurement noise covariance (R) and

initialize error covariance matrix P

Note: In this work, Q = 0.000001, R = 0.2 and P_{init} = 50

3. Calculate the energy and forces for a data point.

4. Calculate the error vector $\delta = [E_{DFT}^{cluster} - E_{NN}^{cluster}, F_x^{DFT} - F_x^{NN}, F_y^{DFT} - F_y^{NN}, F_z^{DFT} - F_z^{NN}]$ Note: The weights are optimized with respect to both energy and forces(3N components)

5. The Hessian matrix is calculated as derivative of error vector with respect to all the NN weights.

6. The KF equations are

$$\lambda_k = \lambda_{cons} * \lambda_{init} + (1 - \lambda_0) \tag{2.22}$$

- In this work, λ_{cons} =0.97 and $\lambda_{init} = 0.999$. λ_{init} is updated iteratively as

$$\lambda_{init} = \lambda_k \tag{2.23}$$

$$A_k = (\lambda_k^{-1} * H * P * H^T) + R \tag{2.24}$$

$$Kg = \lambda_k^{-1} * (P * H^T * A_k^{-1}) \tag{2.25}$$

- The error covariance matrix P is updated as iteration progresses

$$P_{update} = (\lambda_k^{-1} * (P - Kg * H * P)) + Q \tag{2.26}$$

$$P = P_{update} \tag{2.27}$$

- The weights are updated as

$$w_{new} = w_0 + Kg * \delta \tag{2.28}$$

Simultaneous fitting of energy and forces The forces are the negative gradient of energy with respect to the Cartesian coordinates. One of the approximation is to fit the energy using NN and predict forces using the derivative of energy. This is a traditional way to approximate atomic

forces. This requires the calculation of derivative of energy with respect to weights(H matrix in KF). Such an approximation leads to an inaccurate prediction for systems having a complex bonding pattern like gold. Forces can be accurately predicted if they are also fitted using NN in an indirect way. The approach is to initially predict forces using the gradient of the energy obtained from NN. The error is then calculated between the predicted forces and the DFT forces. This error is a 3× atoms(3N) dimensional vector. The error in energy and the 3N dimensional force error is then given to KF for optimizing the weights[76]. Due to this, an additional calculation of the H matrix for forces has to be performed. In this way, the energy and forces are simultaneously fitted using NN with a very high accuracy. Also, such a combined fitting leads to a lesser requirement of dataset as the atomic forces take care of a broad set of clusters in a size range.

2.4 Atomic environment descriptors

As the name suggests, the atomic environment descriptors represents the neighborhood of an atom. These descriptors are usually in terms of radial distribution function and angular functions. The descriptors should be rotationally, translationally and permutationally(in same species clusters) invariant. The mapping of the environments through such desciptors should be unique for different atomic environments. Such functions are given as an input to the NN for predictions of energy and forces. The number of descriptors required to map an environment should be enough to make a complete representation. If the number of descriptors are insufficient, it may lead to a sparse representation. Whereas, if the number of descriptors are large, the representation becomes redundant. So, a basic idea of the atomic system and a lot of trials lead to an efficient selection of the descriptors. In the NN, the total number of descriptors for all the atoms should be same in order to maintain proper dimensions throughout the construction of NN potential. In this work, radial functions and higher order invariants - Power spectrum[52] and Bispectrum[88] has been used

for depicting the atomic environments.

2.4.1 Radial distribution functions

Radial distribution functions (R_f) are two body functions, describing the variation of atoms with respect to interatomic distance. In this work, R_f for an atom i is given as sum of Gaussian functions with different falling rate η(Eq. 2.29) with respect to r_{ij}, the interatomic distance between atom i and j[50]. To probe different radii up to cut-off region, the values are chosen by plotting the radial function with respect to interatomic distance. The space till the cut-off region has to be covered properly and therefore, 9 functions are required corresponding to different falling zones of the Gaussian function. Each interatomic interaction is made smooth and slowly falling using η values. It helps in removing any artifacts when an atom enters or leaves the cut-off region. As shown in Fig. 2.8, a smooth decrease can be seen at different η values, till the cut off length of $8\mathring{A}$. For finalizing the number of parameters, a trial and error method is applied. Using different number of parameters, the NN fitting is performed. The magnitude of the error obtained for prediction of energy and forces helps to choose the required number of parameters. The different values of the falling rate η are given in Table 2.2. The contribution for an atomic energy is restricted by using a cut-off function $f_c(r_{ij})$. As mentioned above, the cut off radius(r_c) of 8 $\mathring{A}$ is kept in order to take all the contributions possible.

$$R_f^i = \sum_{i \neq j}^{atoms} e^{-\eta r_{ij}^2} f_c(r_{ij}) \tag{2.29}$$

$$f_c(r_{ij}) = \frac{1}{2}\left[cos\left(\frac{\pi r_{ij}}{r_c}\right) + 1\right] \tag{2.30}$$

Radial distribution functions prove to be a good descriptor for getting a radial mapping of atomic positions. The radial functions do not incorporate the effects of moving the atoms around the space (with fixed interatomic distance). To get an angular positioning of one atom with respect to another atoms, other functions are required. The angular functions depending

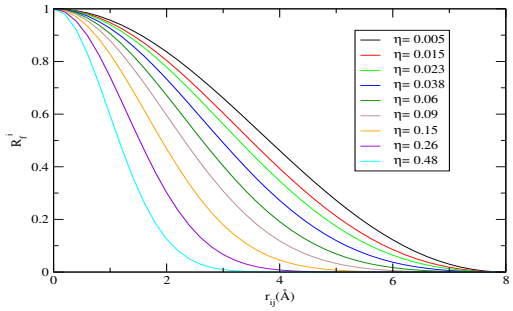

Figure 2.8. The variation of radial function R_f^i with inter atomic distance r_{ij}

Table 2.2. Values of the parameter η

ζ $(\mathring{A}^{-2})$	0.005	0.015	0.0230	0.038	0.060	0.090	0.150	0.260	0.480

on three atoms in a system are generally used to provide the missing information. The calculation of these three body angular functions become computationally expensive with increase in the number of atoms in a system. In this work, the three body angular functions are replaced by higher order invariants obtained from modeling the atomic density in terms of spherical harmonics. The higher order invariants capture the angular positions much accurately and their calculation depends on two body terms rather than three body terms.

2.4.2 Modeling of atomic density

The neighboring atomic density (ρ) of an atom i can be described by delta function summed over all its neighbours j[159].

$$\rho(\mathbf{r}) = \sum_{i \neq j} \delta(\mathbf{r} - \mathbf{r}_{ij}) \tag{2.31}$$

The density can be expanded (Eq. 2.33) in terms of spherical harmonics ($Y_{lm}(\theta, \phi)$) which form an orthonormal basis for the L_2 functions on the unit sphere[52].

$$Y_{lm}(\theta, \phi) = N_{lm} P_l^m(\cos\theta) e^{im\phi} \tag{2.32}$$

where, P_l^m are the associated legendre polynomials and N_{lm} is the normalisation constant given as $\sqrt{\frac{2l+1}{4\pi}\frac{(l-m)!}{(l+m)!}}$.

$$\rho(\hat{\mathbf{r}}) = \sum_{i \neq j} \delta(\hat{\mathbf{r}} - \hat{\mathbf{r}}_{ij}) = \sum_{l=0}^{\infty} \sum_{m=-l}^{l} c_{lm} Y_{lm}(\hat{\mathbf{r}}) \tag{2.33}$$

where, $\rho(\hat{\mathbf{r}})$ is the projection of the density in Eq. 2.31 on the unit sphere. The coefficients c_{lm} in Eq. 2.33 are obtained by taking the inner product with Y_{lm} on both sides as

$$\sum_{i \neq j} \int_0^{2\pi} \int_0^{\pi} \delta(\hat{\mathbf{r}} - \hat{\mathbf{r}}_{ij}) Y_{lm}^*(\hat{\mathbf{r}}) \sin\theta d\theta d\phi = \int_0^{2\pi} \int_0^{\pi} c_{lm} Y_{lm}(\hat{\mathbf{r}}) Y_{lm}^*(\hat{\mathbf{r}}) \sin\theta d\theta d\phi \tag{2.34}$$

The spherical coordinates are r, θ and ϕ which are calculated for a diatomic bond ij as

$$r_{ij} = \sqrt{(x_i - x_j)^2 + (y_i - y_j)^2 + (z_i - z_j)^2} \tag{2.35}$$

$$\theta_{ij} = cos^{-1} \frac{z_i - z_j}{r_{ij}} \tag{2.36}$$

$$\phi_{ij} = tan^{-1} \frac{y_i - y_j}{x_i - x_j} \tag{2.37}$$

θ_{ij} and ϕ_{ij} corresponds to calculation of θ and ϕ for a particular r_{ij}. In spherical coordinates the delta function modifies to

$$\delta(\hat{\mathbf{r}} - \hat{\mathbf{r}}_{ij}) \sin\theta d\theta d\phi = \delta(\cos\theta - \cos\theta_{ij}) \delta(\phi - \phi_{ij}) \sin\theta d\theta d\phi \tag{2.38}$$

So, simplifying Eq. 2.34 and using $\int_0^{2\pi} \int_0^{\pi} Y_{lm}(\hat{\mathbf{r}}) Y_{lm}^*(\hat{\mathbf{r}}) \sin\theta d\theta d\phi = 1$,

$$\sum_{i \neq j} \int_0^{2\pi} \int_0^{\pi} N_{lm} \delta(\cos\theta - \cos\theta_{ij}) P_l^m(\cos\theta) \sin\theta d\theta \delta(\phi - \phi_{ij}) e^{-im\phi} d\phi = c_{lm} \tag{2.39}$$

Solving the independent integrals of Eq. 2.39,

$$\int_0^{2\pi} \delta(\phi - \phi_{ij}) e^{-im\phi} d\phi = e^{-im\phi_{ij}} \tag{2.40}$$

$$\int_0^{\pi} \delta(\cos\theta - \cos\theta_{ij}) P_l^m(\cos\theta) \sin\theta d\theta = P_l^m(\cos\theta_{ij}) \tag{2.41}$$

Therefore, from Eq. 2.39,

$$c_{lm} = \sum_{i \neq j} N_{lm} P_{lm}(\cos\theta_{ij}) e^{-im\phi_{ij}} = \sum_{i \neq j} Y_{lm}^*(\hat{\mathbf{r}}_{ij}) \tag{2.42}$$

It can be seen from Eq. 2.42 that radial information is completely lost from the density projection i.e., r_{ij} is not directly included in the calculation of atomic density. So, a weighting is introduced in the delta functions expansion to provide information about the actual positions of atoms. The modified atomic density function (ADF) is written as

$$\rho(\mathbf{r}) = \sum_{i \neq j} e^{-\xi r_{ij}^2} \delta(\mathbf{r} - \mathbf{r}_{ij}) \tag{2.43}$$

where, $e^{-\xi r_{ij}^2}$ is the Gaussian weighting function. Different values of the factor ξ helps in incorporating the effect of various distances from the central atom. The values of ξ used in this work are given in Table 2.3.

Table 2.3. Values of the parameter ξ

ξ ($\mathring{A}^{-2}$)	0.0028	0.0040	0.0110	0.0280	0.059

Since the atomic interactions over a very long range do not have much impact on energy, the number of neighbors of an atoms are restricted by using a cut off function in the density distribution.

$$\rho(\mathbf{r}) = \sum_{i \neq j} e^{-\xi r_{ij}^2} f_c(r_{ij}) \delta(\mathbf{r} - \mathbf{r}_{ij}) \tag{2.44}$$

The coefficients c_{lm} gets modified according to the modified ADF (Eq. 2.44). They can be calculated as shown below. Along with l and m, now the coefficients are dependent on number of ξ parameters. These parameters

will be represented by n and therefore, c_{lm} is now modified to c_{nlm}.

$$\sum_{i \neq j} e^{-\xi r_{ij}^2} f_c(r_{ij}) \delta(\hat{\mathbf{r}} - \hat{\mathbf{r}}_{ij}) = \sum_{l=0}^{\infty} \sum_{m=-l}^{l} c_{nlm} Y_{lm}(\hat{\mathbf{r}}) \tag{2.45}$$

Simplifying as the same way followed above (Eq. 2.34 to Eq. 2.42), modified c_{nlm} are obtained as

$$c_{nlm} = \sum_{i \neq j} e^{-\xi r_{ij}^2} f_c(r_{ij}) Y_{lm}^*(\hat{\mathbf{r}}_{ij}) \tag{2.46}$$

The entire information of the ADF is contained in the spherical harmonics coefficients c_{nlm}. They provide the amplitude and phase of the function at a particular frequency l and degree m. Overall, it is a signal containing the information of an atomic environment in terms of amplitude and phase. Since spherical harmonics expansion is an infinite series therefore, a truncation is needed at a value of l which gives accurate results i.e, a low error in the NN weights. The maximum value of l is selected by fitting the dataset and thus, the value of l which corresponds to the minimum error in energy and force predictions is then finalized.

2.4.3 Power Spectrum

A rotationally and permutationally invariant descriptor can be obtained from the coefficients c_{nlm} in the form of power spectrum (P_{nl}) as given below[52]. Power spectrum is a second order invariant descriptor. The power spectrum gives the overall amplitude of the signal at a particular frequency.

$$P_{nl} = \sum_{m=-l}^{l} c_{nlm}^* c_{nlm} \tag{2.47}$$

We introduce a normalization constant in our definition of P_{nl} and thus Eq. 2.47 modifies to

$$P_{nl} = \frac{4\pi}{2l+1} \sum_{m=-l}^{l} c^*_{nlm} c_{nlm} \tag{2.48}$$

In the current study, the l is varied from 0 to 9 and the total number of n is 5. So, the total angular coefficients per atom is 50. This formulation of power spectrum using c_{nlm} is applied to single component(SC) systems. In power spectrum, the coefficients (c_{nlm}) are assumed to be uncorrelated to each other and the information about the signal at each frequency is obtained. From earlier studies[52, 134], it is shown that power spectrum is sufficient to represent an atomic environment but still some of the information about the function is lost[88] if the Fourier modes are treated independently[160]. To overcome this discontinuity in representing the atomic environment by power spectrum, third order invariant-bispectrum[88] is studied further.

In Eq. 2.21, the gradients of power spectrum for an atom i can be calculated as follows. The gradient is calculated with respect to x coordinate, which can be derived in a similar way for y and z.

$$\frac{dP^i_{nl}}{dx_i} = \sum_{m=-l}^{l} \left(\frac{dc^i_{nlm}}{dx_i} c^{i*}_{nlm} + c^i_{nlm} \frac{dc^{i*}_{nlm}}{dx_i} \right) \tag{2.49}$$

$$\frac{dc^i_{nlm}}{dx_i} = \sum_{i \neq j} \left(\frac{d(e^{-\eta r^2_{ij}})}{dx_i} Y^m_l(\hat{r_{ij}}) f_c(r_{ij}) + \frac{dY^m_l(\hat{r_{ij}})}{dx_i} e^{-\eta r^2_{ij}} f_c(r_{ij}) + \frac{df_c(r_{ij})}{dx_i} Y^m_l(\hat{r_{ij}}) e^{-\eta r^2_{ij}} \right) \tag{2.50}$$

Note: If coefficient of an atom i is differentiated with repect to coordinate of atom j then, sum over all atoms vanish

$$\frac{dc^i_{nlm}}{dx_j} = \left(\frac{d(e^{-\eta r^2_{ij}})}{dx_j} Y^m_l(\hat{r_{ij}}) f_c(r_{ij}) + \frac{dY^m_l(\hat{r_{ij}})}{dx_j} e^{-\eta r^2_{ij}} f_c(r_{ij}) + \frac{df_c(r_{ij})}{dx_j} Y^m_l(\hat{r_{ij}}) e^{-\eta r^2_{ij}} \right) \tag{2.51}$$

Solving the derivative terms in Eq. 2.50 →

$$\frac{d(e^{-\eta r_{ij}^2})}{dx_i} = e^{-\eta r_{ij}^2}(-\eta 2 r_{ij})\left(\frac{2x_{ij}}{2r_{ij}}\right) = -2\eta e^{-\eta r_{ij}^2} x_{ij} \tag{2.52}$$

$$\frac{df_c(r_{ij})}{dx_i} = -0.5\left(\frac{\pi x_{ij}}{r_c r_{ij}}\right)\sin\frac{\pi r_{ij}}{r_c} \tag{2.53}$$

$$\frac{dY_l^m(\hat{r_{ij}})}{dx_i} = \frac{dY_l^m}{d\theta(r_{ij})}\frac{d\theta(r_{ij})}{dx_i} + \frac{dY_l^m}{d\phi(r_{ij})}\frac{d\phi(r_{ij})}{dx_i} \tag{2.54}$$

The expression for Y_l^m →

$$Y_l^m(\theta,\phi) = \begin{cases} N_{lm}P_l^m(\cos\theta)e^{-im\phi} & \text{when } m < 0, \\ (-1)^m N_{lm}P_l^m(\cos\theta)e^{im\phi} & \text{when } m \geq 0. \end{cases}$$

Note: In the $Y_l^m(\theta,\phi)$, m is always given as $|m|$ for calculations and the negative m is taken as a condition, $P_l^m(\cos\theta)$ are associated Legendre polynomials.

$$N_{lm} = \sqrt{\frac{2l+1}{4\pi}\frac{(l-|m|)!}{(l+|m|)!}} \tag{2.55}$$

We will write the derivative for $m < 0$, and it can be followed in a similar way for $m \geq 0$.

$$\frac{dY_l^m}{d\theta(r_{ij})} = N_{lm}e^{-im\phi}\text{cosec}\theta(l\cos\theta P_l^m(\cos\theta) - (l+m)P_{l-1}^m(\cos\theta)) \tag{2.56}$$

Note: $P_{l-1}^m(\cos\theta)$ becomes 0 when $m > l-1$

So, for $m > l-1$ Eq.2.56 reduces to

$$\frac{dY_l^m}{d\theta(r_{ij})} = N_{lm}e^{-im\phi}\text{cosec}\theta(l\cos\theta P_l^m(\cos\theta)) \tag{2.57}$$

$$\frac{dY_l^m}{d\phi(r_{ij})} = -imN_{lm}P_l^m(\cos\theta)e^{-im\phi} \tag{2.58}$$

$$\frac{d\theta(r_{ij})}{dx_i} = \frac{z_{ij}x_{ij}}{r_{ij}^2\sqrt{x_{ij}^2 + y_{ij}^2}} \tag{2.59}$$

$$\frac{d\theta(r_{ij})}{dy_i} = \frac{z_{ij}y_{ij}}{r_{ij}^2\sqrt{x_{ij}^2 + y_{ij}^2}} \tag{2.60}$$

$$\frac{d\theta(r_{ij})}{dz_i} = -\frac{\sqrt{x_{ij}^2 + y_{ij}^2}}{r_{ij}^2} \tag{2.61}$$

$$\frac{d\phi(r_{ij})}{dx_i} = -\frac{y_{ij}}{x_{ij}^2 + y_{ij}^2} \tag{2.62}$$

$$\frac{d\phi(r_{ij})}{dy_i} = \frac{x_{ij}}{x_{ij}^2 + y_{ij}^2} \tag{2.63}$$

$$\frac{d\phi(r_{ij})}{dz_i} = 0 \tag{2.64}$$

Solving derivative terms in Eq. 2.51

$$\frac{d(e^{-\eta r_{ij}^2})}{dx_j} = -e^{-\eta r_{ij}^2}(-\eta 2 r_{ij})\left(\frac{2x_{ij}}{2r_{ij}}\right) = 2\eta e^{-\eta r_{ij}^2} x_{ij} \tag{2.65}$$

$$\frac{df_c(r_{ij})}{dx_j} = 0.5\left(\frac{\pi x_{ij}}{r_c r_{ij}}\right)\sin\frac{\pi r_{ij}}{r_c} \tag{2.66}$$

Note: $\frac{dY_l^m}{d\theta(r_{ij})}$ and $\frac{dY_l^m}{d\phi(r_{ij})}$ will remain the same.

$$\frac{d\theta(r_{ij})}{dx_j} = -\frac{z_{ij}x_{ij}}{r_{ij}^2\sqrt{x_{ij}^2 + y_{ij}^2}} \tag{2.67}$$

$$\frac{d\theta(r_{ij})}{dy_j} = -\frac{z_{ij}y_{ij}}{r_{ij}^2\sqrt{x_{ij}^2+y_{ij}^2}} \tag{2.68}$$

$$\frac{d\theta(r_{ij})}{dz_j} = \frac{\sqrt{x_{ij}^2+y_{ij}^2}}{r_{ij}^2} \tag{2.69}$$

$$\frac{d\phi(r_{ij})}{dx_j} = \frac{y_{ij}}{x_{ij}^2+y_{ij}^2} \tag{2.70}$$

$$\frac{d\phi(r_{ij})}{dy_j} = -\frac{x_{ij}}{x_{ij}^2+y_{ij}^2} \tag{2.71}$$

$$\frac{d\phi(r_{ij})}{dz_j} = 0 \tag{2.72}$$

2.4.4 Bispectrum

Bispectrum is the Fourier transform of triple correlation function and includes coupling of information from two frequencies (l_1 and l_2) as shown in Eq. (2.73).

$$b_{ll_1l_2} = \sum_{m=-l}^{l}\sum_{m_1=-l_1}^{l_1}\sum_{m_2=-l_2}^{l_2} c_{lm}^* C_{mm_1m_2}^{ll_1l_2} c_{l_1m_1}c_{l_2m_2} \tag{2.73}$$

where, $C_{mm_1m_2}^{ll_1l_2}$ are the Clebsch Gordon coefficients and c_{lm}'s are the harmonic coefficients at a particular frequency. The signal at two frequencies exhibits a phase coupling and thus gives new information as compared to the information obtained from independent frequencies in power spectrum. The non linear coupling leads to an energy transfer between different frequencies and therefore makes them correlated[160]. The phase information which is lost in power spectrum is thus taken into account in bispectrum.

The rules that are followed in construction of bispectrum are (a) l varies from $|l_1 - l_2|$ to $l_1 + l_2$, and (b) $(l_1 + l_2 + l)$ should be an even

number, since the bispectrum coefficients are invariant to reflection and are real numbers. $(l_1 + l_2 + l)$ should not be odd, since the coefficients becomes imaginary and are not invariant to reflection[161], c) $m_1 + m_2 = m$ such that Clebsch Gordon coefficients does not become zero. The value of bispectrum coefficients changes with permutations in l_1, l_2 and l[55]. These are related as

$$\frac{b_{l_1,l_2,l}}{\sqrt{2l+1}} = (-1)^{l_1} \frac{b_{l_1,l,l_2}}{\sqrt{2l_2+1}} = (-1)^{l_2} \frac{b_{l,l_2,l_1}}{\sqrt{2l_1+1}} \tag{2.74}$$

As number of l_1 and l_2 are increased, calculation of bispectrum becomes computationally expensive due to increase in possible combinations for l_1, l_2, l. After many simulations considering different l_1 max and l_2 max values, it is observed that the accuracy of energy and force prediction depends on some of the specific combinations of l_1 and l_2. For keeping the minimum coefficients for describing atomic environment, an algorithm is designed to select the frequencies at which the signals at different frequencies are needed to be coupled. The coupling of specific frequencies is of utmost importance as it leads to more information with less computational calculations. A normalized bispectrum i.e. *bicoherence*[162] is calculated to assess the frequencies that contains correlated information.

$$\text{bicoh}(l_1, l_2) = \sqrt{\frac{b^2_{ll_1l_2}}{P_{l_1}.P_{l_2}.P_l}} \tag{2.75}$$

It signifies the fraction of energy present in a signal at frequency l due to coupling between l_1 and l_2. The bicoherence values lie in the interval $0-1$. A value towards 1.0 indicates high phase coupling and a value towards 0.0 indicates very weak coupling such that random phases are present between the frequencies. To remove similar coefficients due to permutation in l_1, l_2, and l, the bicoherence formula is modified as

$$\text{bicoh}(l_1, l_2)^{updated} = \frac{bicoh(l_1, l_2)}{\sqrt{2l+1}} \tag{2.76}$$

The bispectrum and power spectrum values for different frequencies

are calculated. The bicoherence value for each combination of l_1, l_2, and l is then estimated. The top 15 combinations which have bicoherence values between 0.3 to 1.0 is chosen. It allows us to take the coefficients which are sufficient to describe the complex atomic environments. Since, spherical harmonics are used for describing the environments, therefore, each atom will have different values of bispectrum coefficients. So, the combinations of l_1, l_2 and l won't be same for all the atoms in a cluster. In this way, each atom has different sets of frequency coupling and calculating bicoherence gives us the maximum information of the function. In this work, l_1 and l_2 are varied from 0 to 4 and l varies from $|l_1 - l_2|$ to $(l_1 + l_2)$. A total of 35 combinations are possible for different values of l_1, l_2 and l as shown in Table 2.4. The overall algorithm is given stepwise as follows.

1. Calculate all the possible combinations of l_1, l_2 and l.
2. Calculate bispectrum coefficient of a particular combination.
3. Calculate power spectrum coefficients at all the possible frequencies between $|l_1 - l_2|$ and $(l_1 + l_2)$.
4. Calculate bicoherence using Eq. (2.76).
5. If value of bicoherence is ≥ 0.3 then save that frequency combination else discard it.
6. Arrange the coefficients in order of decreasing bicoherence values.
7. Take the top 15 combinations per atom ▷ Input coefficients are fixed for NN

2.4.5 Descriptors for Multi Component system

The modeling of atomic density for a multi component (MC) system cannot be the same as a SC system because each element in the periodic table has different bonding patterns which is not captured by kernel based methods. Behler et al[30, 61] proposed to use different set of network weights for all

Table 2.4. Possible combinations of l_1, l_2 and l for $l_1$max $= 4$, $l_2$max $= 4$

l_1 l_2 l	l_1 l_2 l	l_1 l_2 l	l_1 l_2 l	l_1 l_2 l
000	121	222	246	345
011	123	224	330	347
022	132	231	332	440
033	134	233	334	442
044	143	235	336	444
110	145	242	341	446
112	220	244	343	448

the elemental species in a system. This scheme is computationally effective for a system consisting of a few chemical species. On increasing the types of chemical species, the number of networks increases, thus increasing the complexity of fitting. One way to overcome this situation is to differentiate the chemical species at the descriptor level and use a single set of network weights for the entire molecular system. Recently, Gastegger et al.,[163] Artrith et al.[62] and Unke et al.[56] have proposed the weighting of descriptor functions according to an element and fitted the energies of a molecular dataset.

Since atomic forces are of utmost importance to run MD simulations, a concurrent fitting of energy and forces for MC system using NN through a single network has to be done. At first, a bond specific weighting of atomic density and radial functions (given in equation 2.44 and 2.29) is introduced.

$$\rho^h_{mod}(\mathbf{r}) = \sum_{h \neq k} w_{hk} e^{-n r^2_{hk}} \delta(\mathbf{r} - \mathbf{r}_{hk}) f_c(r_{hk}) \tag{2.77}$$

$$d^h_{\text{mod rad}} = \sum_{h \neq k} w_{hk} e^{-\xi r^2_{hk}} f_c(r_{hk}) \tag{2.78}$$

The w_{hk} is specific for a bond (b_{hk}) between atom h and k. This is chosen as $exp(\frac{\mu_{hk}}{m_\alpha})$, where μ_{hk} is the reduced mass of b_{hk} given as $\frac{m_h \times m_k}{m_h + m_k}$. m_h, m_k are the molecular mass of atom h and k, respectively. m_α takes the value of the molecular mass of atom whose local environment is being calculated. Comparing with the existing approach for SC systems, it can be deduced as modified exponentially weighted descriptors (MEAD). The energy of the

clusters is calculated using MEAD in the NN.

To obtain the atomic forces for the MC system, the gradient of energy obtained from MEAD is calculated. This leads to an unnecessary scaling of the forces as the individual weighting of bonds makes it difficult for NN to find a global minimum (GM) in weights. This bottleneck is managed by modeling the forces in a decoupled manner from the energy obtained above. The initial step is to set the bond specific weighting in MEAD to be unity. This makes the MC system to behave as SC system. A dummy energy from the NN is obtained by using the descriptors whose bond specific weighting is unity. These descriptors does not contain any element specific information. To incorporate the nature of the atom in the local environment, an element specific weighting of the gradients is introduced. The gradient of the descriptor with respect to the coordinates of the atoms as shown in Eq. 2.79 is weighted. This element specific weighting embeds the fluctuations in the descriptor with slight variation in position with respect to a particular element such that when the data will be trained via NN, network will recognize the element specific variations for the forces.

$$F_R^{\text{weighted}} = -\sum_{N=1}^{atoms}\sum_{k=1}^{input}\frac{\partial E'_N}{\partial d_{N,k}}\left(w_\beta \times \frac{\partial d_{N,k}}{\partial R}\right) \tag{2.79}$$

Here, E'_N is the dummy energy obtained from descriptors with $w_{hk} = 1$ and $d_{N,k}$ are the MEAD with $w_{hk} = 1$. The E'_N is termed as a dummy energy as no element specific information is contained and the energy of the cluster is not trained using this. w_β is chosen as the ratio of the effective nuclear charge of the valence electrons of an element(Z_e) to that of total effective nuclear charge of all the chemical species present in the molecular system. The proposed model is shown in a concise way in Fig. 2.9. It consists of supplying two sets of descriptors - (i) MEAD for energy, (ii) MEAD with $w_{hk} = 1$ for forces, into the NN. The first output of the model is system energy obtained from the weights of the NN and the MEAD descriptors. The second output is atomic forces which are obtained using

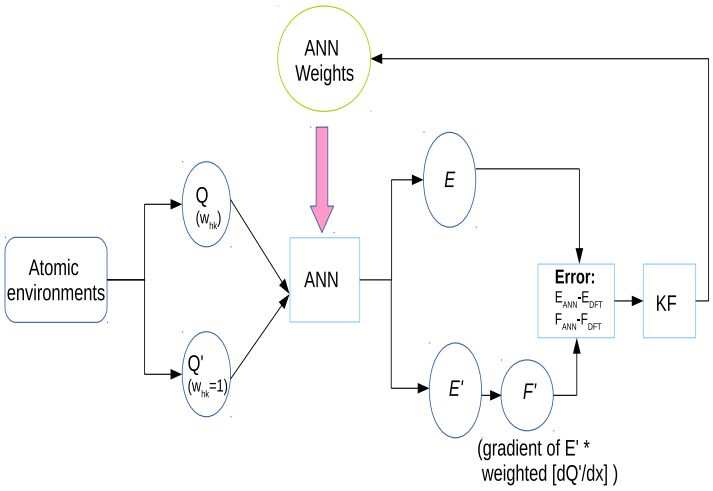

Figure 2.9. The proposed model for concurrently fitting energy and forces of a cluster. Q and Q' are the descriptors for E and F', respectively. $F' = F_R^{\text{weighted}}$ and $E = E_{cluster}$. The block KF represents the global extended KF.

the same weights of the NN but different descriptors. The total scheme is summarized as follows.

1. Calculate the MEAD using Eq. (2.77) and (2.78) of all the atoms for fitting the energy of a cluster.

2. Calculate the descriptors (MEAD with $w_{hk} = 1$) and gradients of descriptors with respect to atomic positions using $\left(w_\beta \times \frac{\partial d_{N,k}}{\partial R}\right)$ for all the atoms for fitting the atomic forces.

3. Split the entire dataset into a training and testing set for NN.

4. The NN is then trained with different types of clusters and the weights are validated after each iteration.

5. The training is stopped when a minimum root mean square error is observed.

2.5 Construction of data for any atomic system

All the proposed descriptors- radial function, power spectrum for SC and MC system and bispectrum are calculated using the interatomic distances. For a MC system, along with interatomic distances, effective nuclear charges of the chemical species and the reduced mass corresponding to a particular bond are calculated. This makes the proposed approach to be applicable for any atomic system. These descriptors-NN combination can be applied to construct the PES of any molecular system. The basic ingredient of construction of PES is the dataset, which is fitted using descriptor-ANN integrated model.

In order to fit large size clusters, an economic approach named *split technique* is designed. According to the split technique, for any cluster, an atom is chosen. Its neighbouring atoms along with that atom are cut from the cluster to form small sized clusters. The radius of all these small clusters is the fixed cut-off distance. Using this way, many small sized clusters can be generated from a large atom cluster. A similarity check is run between different small clusters to avoid any repetition of an environment. The advantage of this approach is that the dataset can be constrained to clusters with less than 100 atoms, but fit it up to environments of large sized clusters. The split technique is much efficient and easier to use than cutting the molecule in two halves. The cutting leads to structure having a very high energy due to dangling bonds. The splitting of clusters radially with respect to a cut-off radius reduces the presence of dangling bonds. The input functions in NN are atomic descriptors and therefore split technique provides a benefit in fitting the NN. To generate any dataset, following steps should be followed:

1. Choose an initial potential - Empirical potential, Force fields or *ab initio*.

2. Run Monte Carlo simulations, Basin hopping (BH), MD simulations

using any of the above potentials.

3. Collect around 2000 clusters and optimize them for minimizing the forces.

4. Calculate the *descriptors* and its gradients for the clusters and simultaneously calculate the energy and forces using DFT.

5. Feed the data obtained in above step to ANN and fit it using KF[74, 75]/Back propagation[78]/Conjugate gradient[79]/LEMA[77]/QN method[158]/ L-BFGS[73] or any other optimization algorithm to optimize the set of NN weights.

6. For an accurate representation of PES, generate more dataset using MD simulations (potential- NN) at different temperatures.

7. In case of big clusters (>100 atoms), split them in small atomic environments such that core and surface configurations are included in the dataset.

8. On refining and optimizing the different clusters obtained, repeat step 4.

9. A final fitting is done using around 11000 clusters and the converged weights can be utilized further in many applications.

2.6 Exploring the PES

After fitting the interatomic potential with a dataset, the PES of any Np can be explored using different methods like MD simulations, Monte Carlo simulations, BH, multicanonical basin hopping (MCBH), genetic algorithm among others. For very large clusters, a new tool namely "searching amorphous structure" (SAS) is designed. This is an effective tool for narrowing down the exploration of PES by generating structures that are near to GM. This tool is beneficial for the systems which prefer amorphous geometries and distorted symmetric structures.

2.6.1 MD simulations

MD simulations have been an effective tool since 1980s for simulating a molecular system with time[164, 165]. The equation of motion (F=ma, a=d^2x/dt^2) is solved to get the evolution of the atomic system with time. The acceleration of atoms is dependent on the positions and velocities. These are estimated using different algorithms like Verlet, leap frog. An MD simulation begins with an initial set of coordinates and velocity. The acceleration is then calculated by $a = F/m$, where F is obtained from the interatomic potential. In this work, the position and velocity updates with time is estimated using velocity-verlet integration[166]. The temperature is kept constant using Andersen thermostat[164]. These are the equations for the position and velocity update.

$$\vec{r}(t + \delta t) = \vec{r}(t) + \vec{v}(t)\delta t + \frac{1}{2}\vec{a}(t)\delta t^2 \tag{2.80}$$

The $\vec{r} \in \{x,y,z\}$, δt is the small change in time, $\vec{v}(t)$ is the atomic velocity and $\vec{a}$ is the acceleration. The $\vec{a}(t + \delta t)$ is calculated using $a = F/m$, with updated $\vec{r}(t + \delta t)$. The velocities are updated as

$$\vec{v}(t + \delta t) = \vec{v}(t) + \frac{1}{2}(\vec{a}(t) + \vec{a}(t + \delta t))\delta t \tag{2.81}$$

The MD runs are performed at various temperatures to explore multiple zones of PES. The simulation time is kept according to the computational resources and the molecular system evolution. The trajectories obtained from MD runs are saved with respect to different temperatures and time step. After initial 1000 structures, different structures are picked at every 100 step. These structures are then quenched to get a local minimum. This helps in identifying a lot of local minimum structures on PES and thus an effective exploration.

2.6.2 Monte Carlo simulations

Monte Carlo simulations[167] generates a pool of structures based on the energy differences. At each Monte Carlo step, the structures are modified by randomly changing the coordinates of either one atom or multiple atoms. The random movement (Δr) lies in a range from $-\Delta r_{max}$ to $+\Delta r_{max}$. The energy of the new structure (E_{new}) is calculated and compared with the energy of the previous structure (E_{old}).

$$\Delta E = E_{new} - E_{old} \tag{2.82}$$

If ΔE is negative, then the move is accepted and the new structure is added to the pool. If ΔE is positive, the new structure has higher energy than the previous structure. In such case, an acceptance criterion is applied. The Boltzmann probability is calculated using

$$P = e^{-\frac{\Delta E}{kT}} \tag{2.83}$$

A random number(ω) is generated between $0 - 1$. If P is greater than ω, then the move is accepted, else if the ω is greater than P, then the move is rejected and the simulation is started from the previous structure again. The approach that Monte Carlo follows is the statistical probability for accepting or rejecting a structure. On the other hand, MD simulations solves the Newton equation of motion and gets an ensemble average over a period of time.

2.6.3 BH

BH[168] is a variant of Monte Carlo method where energy sampling is done for the optimized structures. An initial structure is constructed. It is followed by minimization of the energy using a gradient based optimization technique. In this work, L-BFGS algorithm was used. In the next step, the atoms are displaced randomly and the structure is minimized. To accept a move, the Boltzmann probability is calculated using the minimized energies

of the structure. BH helps to find the low energy regions of PES. Various atom displacing techniques can be applied to get different regions on the PES. BH can lead to a local minima trap if the random displacements are not effective to take the system out of a potential energy well. To overcome this problem, MCBH is used.

2.6.4 Multi Canonical BH

The probability with which a structure is accepted or rejected is modified in MCBH[169, 170, 171]. The Boltzmann weight(w) is replaced by the weight which is dependent on density of states($\rho(E)$). The probability distribution during the sampling is

$$P(E,T) \propto \rho(E)w(E) \tag{2.84}$$

The weight is dependent on the density of states as $w(E) \propto 1/\rho(E)$. Therefore,

$$P(E,T) \propto \rho(E)\frac{1}{\rho(E)} = \text{constant} \tag{2.85}$$

This makes the exploration of the entire energy space by random displacements. The density of states are estimated initially, which is then updated as the sampling progresses. Initially, weight w is taken as $e^{-\beta^{(0)}E}$. The BH is run and an energy histogram $H^{(1)}(E)$ is generated from the sampled structures. The energy histogram can be written as

$$H^{(1)}(E) \propto \rho(E)w^{(0)}(E) \tag{2.86}$$

$$\rho(E) \propto \frac{H^{(1)}(E)}{w^{(0)}(E)} \tag{2.87}$$

Since, $w^{(1)}(E) = 1/\rho(E)$,

$$w^{(1)}(E) \approx \frac{w^{(0)}(E)}{H^{(1)}(E)} \tag{2.88}$$

These steps are performed till the last iteration(n) to obtain $w^{(n)}(E)$ such that $H^{(n+1)}(E)$ is obtained. The overall steps of multi canonical BH is

1. A first BH run is performed.

2. The minimum and maximum energy obtained from the run is noted.

3. The energy interval ($E_{max} - E_{min}$) is divided into b bins with width $(E_{max} - E_{min})/b$.

4. For each bin, the statistics are obtained and histogram is filled for all the states.

5. For the next iteration, the entropy is calculated to give the weight(w) for the system. This leads to a new hopping for further exploration of PES.

2.6.5 SAS tool

Using the SAS tool, for structures having multiple layers (core and shell), spherical structures are constructed with different number of atoms possible in each spherical layer. Initially, the number of layers a nanocluster/Np can possess is checked. The diameter of each layer is then fixed accordingly. To take care of all the atomic combinations possible in a layer, the number of atoms are varied by ± 10 with respect to an expected number of atoms. After generating different structures, optimization is carried out using NN as the interatomic potential and L-BFGS as the optimizer. In order to incorporate the Ih, Dh and Oh symmetry in the core, few clusters were constructed having spherical layers over the Ih, Dh and Oh symmetric cores.

To assess the credibility of the proposed scheme, the SAS tool was applied for the clusters whose lowest energy structures are already identified - Au_{34}[31, 172, 173, 174], Au_{42}[175], Au_{55}[98, 111, 127, 128, 131, 132], Au_{58}[31, 118, 176] and Au_{147}[134, 136]. The process began with the construction of 15 structures of each with different atomic arrangements. On optimization using L-BFGS, all the structures were found to be near to their possible GM. For Au_{34}, three structures having 2, 3 and 4 atoms in the core with a caged surface was obtained. For Au_{42}, 3, 5 and a 6 atom

core structures were obtained with an amorphous surface. For Au_{55}, 7 and 8 atoms in the core were obtained on optimization. There was a 10 atom core obtained for Au_{58} and for Au_{147}, a range of structures were observed with surface atoms varying from 100 to 107. The results obtained for these clusters led to further apply SAS tool to get an insight into large sized clusters. The SAS tool is briefly described in following steps.

1. Calculate the expected number of layers in a nanocluster/Np according to its size.

2. Specify the diameter of each spherical layer.

3. Take a range of number of atoms in each layer (expected atoms $\pm$ 10)

4. Make spherical layers taking number of atoms and diameter into consideration.

5. Merge all the spherical layers in one structure to make a spherical structure.

6. To take care of possibility of a symmetric core :-

   Take Ih, Dh, Oh geometry as core and put a spherical layer of atoms over it.

7. Optimize the spherical structure and search for more minimas using any of the methods like BH[168], Genetic Algorithm[177, 178], MD simulations, MCBH[169, 170, 171] etc.

Chapter 3

Exploring the PES of Au_{147} using Power spectrum descriptors

3.1 Introduction

Gold nanoclusters have always been a subject of interest for research in various applications like plasmonics,[179] biomedical,[179, 180] non-linear optics,[179] catalysis[179] among others. The larger symmetry clusters, known as magic number clusters, for gold[120] have been identified as Au_{13}, Au_{55}, Au_{147}, Au_{309}, Au_{561} and Au_{923}. These clusters tend to be more stable and show different reactivities[119, 123] when compared to non-magic clusters. The assumed geometry of these clusters is Ih which has been recently published by Li *et al.*.[120] In this chapter, NN potential is constructed using power spectrum descriptors to analyze the dynamics of Au_{147}. In the literature, Au_{13} and Au_{55} has already been proved to have non-symmetric structures. So, for this study Au_{147} is chosen to find the structural variation and preference for symmetry in these clusters. From an EXAFS study[181, 182] on bare and supported Au_{147}, it has been recently shown that Au_{147} exhibits an Ih geometry. In this study, it is found that although being magic, Au_{147} does not exhibit an Ih geometry. Also, according to DFT, the Ih geometry lies 4 eV higher than the predicted GM structure. The fluxional property of Au_{147} has also been studied using various order parameters.

3.2 Computational details

Descriptors The atomic environment descriptors consists of 9 radial functions given by Eq. 2.29 and 50 power spectrum coefficients given by Eq. 2.48. The c_{nlm} is given by Eq. 2.46. A maximum value of $l = 10$ gave the lowest RMS error for energy and forces.

Generation of dataset Initial data for fitting is generated using Monte Carlo simulations with Gupta potential and an initial fit is done with NN. The MC simulations are run for different initial geometries for 1 million steps such that a variety of structures are obtained. After the first set of weights are obtained, MD simulations are run using those weights at different temperatures at a time step of 3 *fs* to obtain more refined data for $Au_{30} - Au_{147}$ range of nanoclusters. To reduce the computational burden of running DFT based MD simulations for generating more data for a large system ($Au_{30} - Au_{147}$), an initial set of NN weights are obtained. The structures are then quenched using L-BFGS algorithm and then they are included in the database. To make the calculations computationally cheap, 1000 clusters of Au_{147} are split into small clusters. Along with the environments, 30 Au_{147} clusters are taken (without splitting) in the dataset. Overall, $10,136$ clusters are generated which contains all types of clusters below 100 atoms. The entire dataset of $10,136$ clusters is shuffled and divided into training set of 9050 clusters, and test set of 1086 clusters.

DFT calculations The DFT calculations are performed using VASP.[141, 142, 143, 144] The PAW method is used to describe the core electrons. It takes into account the relativistic effects in gold clusters. The electron correlation is described by generalized gradient approximation using the PBE functional.[146, 147] To sample the Brillouin zone, Gamma k-point ($1\times 1 \times 1$) mesh is used. The cell size for clusters below 100 atoms is taken $20 \times 20 \times 20$ $\mathring{A}^3$, whereas for Au_{147} it is kept $25 \times 25 \times 25$ $\mathring{A}^3$. The threshold energy is set to be 250 eV and the gradient convergence is set as 10^{-4}.

Table 3.1. RMS error in energy and forces for different size of training set

Size	RMS error energy(meV/atom)	RMS forces error (meV/Å/atom)
1086	10.846	143.305
2172	7.78	124.332
5068	5.57	85.255
9050	5.00	84.00

3.3 Results

3.3.1 Fitting of energy and forces by NN

The fitting of radial functions and power spectrum coefficients with NN shows a very smooth decay in the RMS error of energy and forces with each iteration. An RMS error of 5 meV/atom for energy and 84 meV/Å/atom for forces was obtained. The number of iterations in which the error converged is 7, which shows that fitting can be done very fast using these descriptors-NN combination. The testing and training RMS error of energy with iterations is plotted in Fig. 3.1. For measuring the sensitivity of this prediction model with respect to the size of training set, a PES fitting for different size of the dataset is done. The RMS error in energy and forces with respect to size of the training set is reported in Table 3.1. With an increase in size of the dataset, the RMS error decreases and a saturation in the RMS error is observed after a certain size of dataset is reached.

3.3.2 Comparison of power spectrum coefficients with other descriptors

Bartók *et al.*,[52] incorporated the radial information of a system in the c_{nlm} by taking a product of orthonormal radial functions with the spherical harmonics in the expansion of the density. This leads to modified basis

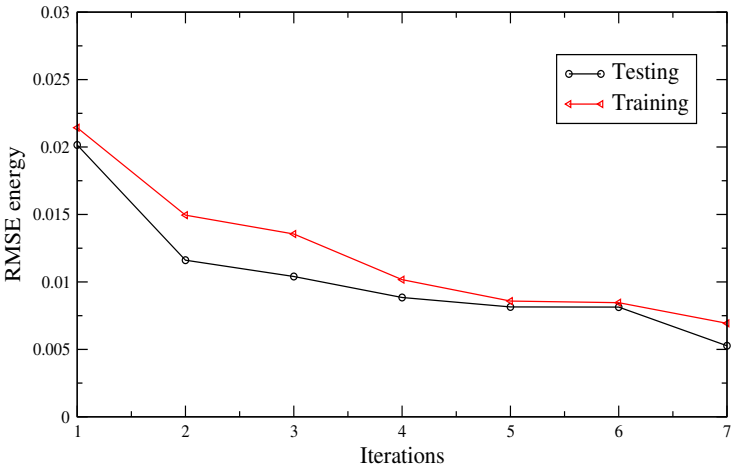

Figure 3.1. Decay in the RMS error of energy for training and testing dataset with iterations

functions.

$$\rho(\mathbf{r}) = \sum_{i \neq j} \delta(\mathbf{r} - \mathbf{r}_{ij}) = \sum_{n} \sum_{l=0}^{\infty} \sum_{m=-l}^{l} c_{nlm} g_n(r) Y_{lm}(\hat{\mathbf{r}}) \tag{3.1}$$

On solving, c_{nlm} is obtained as

$$c_{nlm} = \sum_{i \neq j} g_n(r_{ij}) r_{ij}^2 Y_{lm}^*(\hat{\mathbf{r}}_{ij}) \tag{3.2}$$

Using these coefficients in the power spectrum expression and fitting them with NN did not give convincing results. Although, the weights obtained gave RMS error of 12 meV/atom in energy prediction and 92 meV/Å/atom in forces prediction, they were unable to give an accurate prediction when atoms are very far and very close to each other. Behler's symmetric functions[50] were also calculated for the dataset and trained using NN. The RMS error in energy and forces for Behler's functions was 9 meV/atom and 112 meV/Å/atom respectively. In Table 3.2 below, the comparison of the accuracy in predicting the energy and forces of power spectrum-NN method, Behler's symmetric functions[50] based method, and Bartok's descriptor[52] with ANN is mentioned. It can be seen that the proposed method achieves the smallest RMS error in energy and forces as compared to both the other methods. Therefore, the approach of providing radial functions separately and using a weighted delta function for density pro-

jection, is an effective way to model interatomic potentials for metallic systems.

Table 3.2. Comparison of RMS error in energy and forces for different models

Size	Energy(meV/atom)	Forces (meV/Å/atom)
Proposed method	5.00	84.00
Bartok power spectrum-NN	12.00	92.00
Behler functions-NN	9.00	112.00

3.3.3 Validation of the weights

The validation of the obtained weights (RMS error of 5 meV/atom for energy and 84 meV/Å/atom for force prediction) is done on 190 clusters quenched from MD simulations (at 400 K) of $Au_{30} - Au_{147}$. The energy per atom for these clusters for both DFT and NN is plotted in Fig. 3.2. From this plot, it is observed that the NN predicted energies are in an agreement with the DFT predicted energies. For a clear resolution, the relative difference between NN and DFT predicted energies is plotted as shown in Fig. 3.3, in which maximum number of clusters lies in the range of average RMS error energy i.e., 5 meV/atom, while a few clusters lies above and below the error range. One of the reason for this may be the presence of a wide range of dataset which is fitted for the PES. This validation helps to measure the prediction accuracy of the optimized weights on the clusters other than the test set.

The NN predicted and DFT predicted energies of Au_{147} clusters are compared within an energy range of 6 eV. Randomly, 10 clusters of Au_{147} are chosen and an optimization is done by DFT and NN potentials. Their energies are compared as shown in Fig. 3.4(a). Also, the energies of 30 unoptimized clusters of Au_{147} is compared using DFT and NN as shown in Fig. 3.4(b). It is inferred that NN potential predicts energy in agreement with DFT for high as well as low energy clusters.

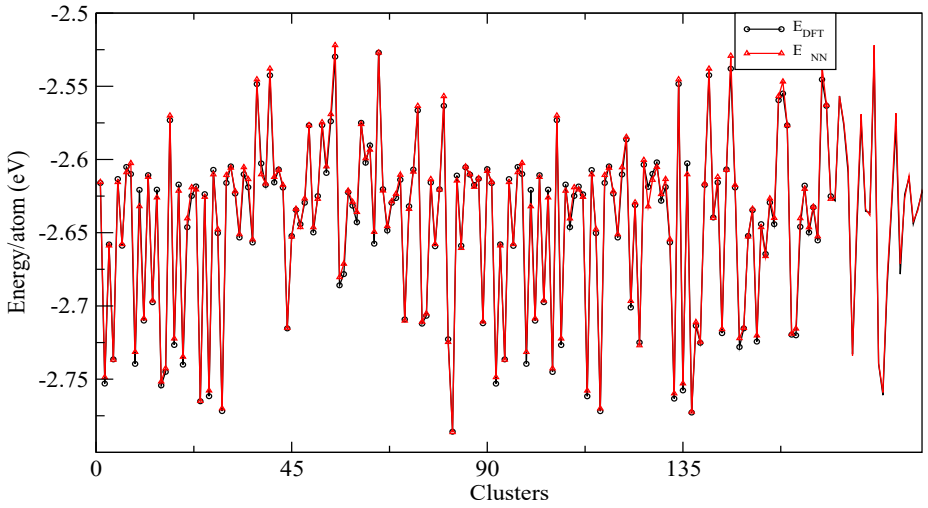

Figure 3.2. Comparison of DFT and NN predicted energies for $Au_{30} - Au_{147}$ clusters

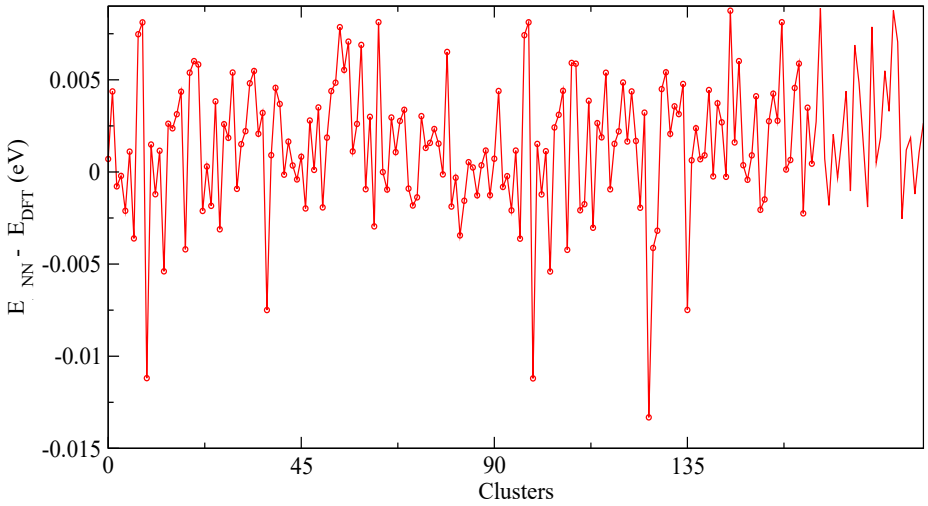

Figure 3.3. Relative difference between DFT and NN predicted energies (per atom) for $Au_{30} - Au_{147}$ clusters

3.3.4 Computational time for energy and force calculation

The time taken for calculation of energy and forces of a Au_{147} cluster is 3 seconds on a single CPU [GenuineIntel 2600.0 MHz] unlike DFT which takes around 7 hours on parallelized 16 CPU [GenuineIntel 2600.0 MHz] for this calculation. Using the Behler's symmetric functions[50], the time taken for the same system is around 14 seconds. Therefore, the approach used in this study is economic and computationally cheap. A parallel code

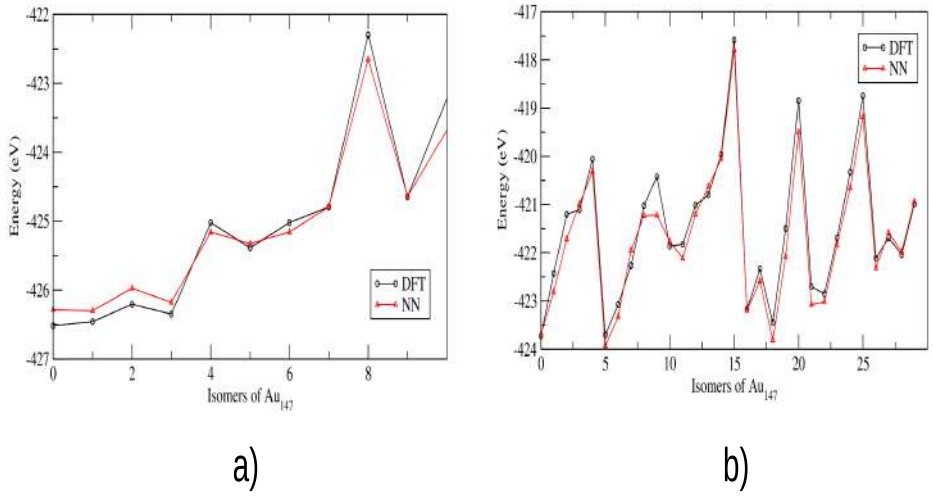

Figure 3.4. Comparison of DFT and NN predicted energies of a range of Au_{147} clusters a) Optimized clusters b) Unoptimized clusters

is also written for the functions. The time for calculation of energy and forces of one Au_{147} reduced to 1.7 seconds on 8 CPU [GenuineIntel 2600.0 MHz] using the parallel code.

3.3.5 Global Optimization of Au_{147} cluster

The GM search for Au_{147} using BH method is performed. The initial structures for BH are selected from the MD simulations performed at 300 K, 400 K, 500 K and 600 K. These structures are quenched first and then taken as the beginning structure for global optimization runs. The GM search is started using 10 different initial structures of Au_{147} and each BH run is done for 20,000 steps. Au_{147} is one of the magic number cluster, and therefore the most stable structure assumed for it is an Ih[120, 181, 182]. A large number of isomers of Au_{147} were generated and the structural pattern they follow is 105 atoms in the outer shell, 35 atoms in the middle shell, and 7 atoms in the inner shell, unlike an Ih that contains 13 atoms in the inner shell, 42 atoms in the middle shell and 92 atoms in the outer shell. According to NN, and verified from DFT, the GM contains a 7 atom symmetric inner core structure, with the arrangement of the 35 atoms in the middle layer, also in a symmetric manner. The energy of the Ih is

almost 4.0 eV higher than the GM structure obtained as shown in Table 4.1. Since the converged energy error is 5 meV/atom, for a 147 atoms cluster, it becomes 0.7 eV on an average. Therefore, the predicted NN energy lies in the error range and is not exact in magnitude as DFT. The structure of Ih geometry and the predicted GM is shown in Fig. 3.5.

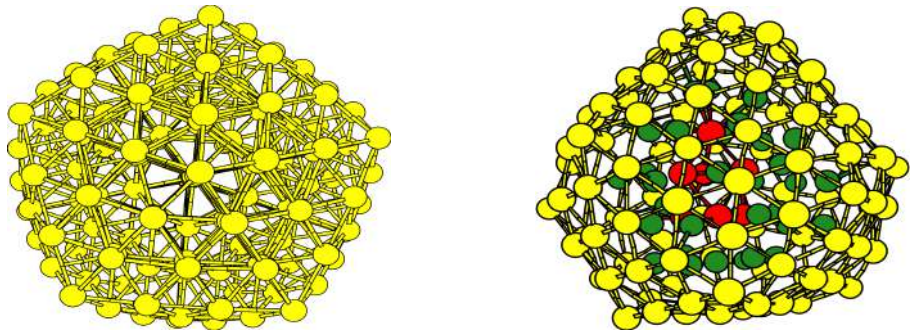

Figure 3.5. Geometries of Au_{147} a) Ih, b) GM

Table 3.3. Energy of GM and Ih structure of Au_{147}

Structure	Fig. 2(a)	Fig. 2(b)
DFT (eV)	-422.2959	-426.5174
NN (eV)	-422.6557	-426.2996

The inner core of the predicted GM structure is shown in Fig. 3.6. The atomic arrangement of 7 atoms makes a monocapped octahedron. A lot of isomers of Au_{147} that are very close in energy (0.5 eV), but different in the atomic arrangements were encountered. These isomers consists of 6 - 7 atoms in inner layer, 35 - 36 atoms in middle layer and, 105 atoms in the third shell is maintained. Due to a high energy difference between the Ih

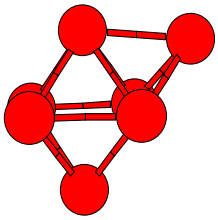

Figure 3.6. 7 atom inner core of GM

structure and the predicted GM structure, it can be inferred that being a

magic cluster, Au_{147} does not exhibit Ih structure as the most stable isomer and there are a lot of other stable geometries possible for it.

3.3.6 Comparison between Au_{68} and Au_{147}

Xu *et al.*[183] identified new structures of thio protected Au_{68}, which contains a 32 atom core. The arrangement of the atoms in the core resembles the core structure of the GM of Au_{147} predicted by DFT (42 atoms) as shown in Fig. 3.7. The core shows a layer pattern, which is also reflected in core of Au_{147} GM. Since the number of atoms are not equal, therefore, a resemblance can be predicted by comparing the layers in both the structures. In the top two layers (colored red), the number of atoms in Au_{68} is 10 and in Au_{147} it is 8, but the coordination number of the capped atom is 5 in both the structures. In the same layers, a hexagonal shaped arrangement of atoms is observed for both the structures. In the orange colored layer, there are 10 atoms in Au_{68} and 11 atoms in Au_{147}, which indicates the binding of atoms in a similar way for both the clusters as atoms are varying by just one in number. The yellow colored layer contains 14 atoms in Au_{147} and 9 atoms in Au_{68}, but the coordination number of the surface atoms of the core structures is found to be same. The blue colored layer consists of only 3 atoms in Au_{68} and 9 atoms in Au_{147}. This layer is not similar but from the pattern followed in other layers, it can be deduced that in presence of more atoms, this layer will also exhibit same pattern as that in Au_{147}. So, it can be concluded that on evolving from Au_{68} to Au_{147}, a similar pattern in the core is maintained.

3.3.7 Temperature dependent probability of Au_{147} isomers

Nps are highly sensitive materials and their stability depends on numerous parameters. One of the important parameter is temperature. Around 60 isomers of Au_{147}, that are within 0.5 eV of the predicted GM isomer were

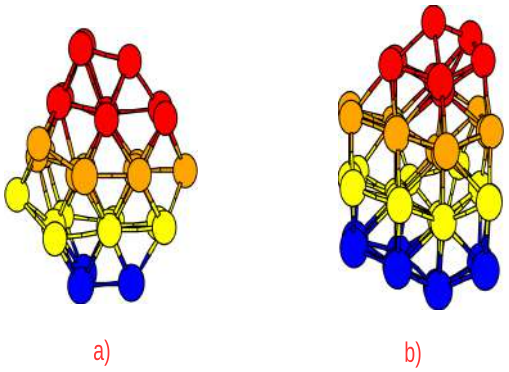

Figure 3.7. a) The layer pattern in the core geometry of Au_{68} (Xu et al), b) The layer pattern in the core geometry of predicted GM of Au_{147}

collected. Since GM cannot be stable at all the temperatures, therefore, to find the most probable structures at different temperatures, the probabilities of all these isomers at 3 temperatures - 300 K, 500 K and 800 K using the method implemented by Li *et al.*[184] was calculated. This method gives the probability of a particular isomer at a temperature by implementing rotational, vibrational and electronic partition functions in the calculation. The equation for calculating the probability of one structure is

$$P_\omega = \frac{e^{\left(\frac{-\Delta E^\omega}{K_B T}\right)} q^\omega_{rot} q^\omega_{vib} q^\omega_{ele}}{\sum_\omega e^{\left(\frac{-\Delta E^\omega}{K_B T}\right)} q^\omega_{rot} q^\omega_{vib} q^\omega_{ele}} \tag{3.3}$$

The ΔE^ω represents the relative potential energy of an isomer with respect to GM. The rotational, vibrational and electronic partition function of an isomer is represented by q^ω_{rot}, q^ω_{vib} and q^ω_{ele}, respectively. The electronic transitions are of very high energy therefore, the term is omitted as the molecule preferably stay in the ground state, and the excited states have a negligible contribution to the partition function.[185] Rigid rotor approximations and harmonic approximations are adopted for calculating the rotational and vibrational partition function, respectively. The Eq. (3.3) modifies to

$$P^m_\omega = \frac{e^{\left(\frac{-\Delta E^\omega}{K_B T}\right)} q^\omega_{rot} q^\omega_{vib}}{\sum_\omega e^{\left(\frac{-\Delta E^\omega}{K_B T}\right)} q^\omega_{rot} q^\omega_{vib}} \tag{3.4}$$

P^m_ω refers to the modified probability expression. The rotational and vibrational partition functions are calculated using the formulas shown in Eq.

(3.5) and Eq. (3.6).

$$q^{\omega}_{rot} = \left(\frac{8\pi^2}{\beta h^2}\right)^{3/2} \frac{\sqrt{\pi I^{\omega}_a I^{\omega}_b I^{\omega}_c}}{\sigma^{\omega}} \tag{3.5}$$

$$q^{\omega}_{vib} = \prod_n \frac{e^{\frac{-hc\tilde{\nu}^{\omega}_n}{2K_BT}}}{1 - e^{\frac{-hc\tilde{\nu}^{\omega}_n}{K_BT}}} \tag{3.6}$$

$\tilde{\nu}$ is the wave number of n^{th} normal mode of an isomer and I^{ω}_a, I^{ω}_b, I^{ω}_c are the three principle moments of inertia of the isomer. It is observed that the probability of GM is found to be less than the other isomers at all the temperatures considered. It is also observed that the top 20 isomers after the GM exhibits similar probability, indicating the presence of a mixture of isomers at a particular temperature. Considering the maximum peak in the probability plot (Fig. 3.8), it is inferred that isomer-12 is the most probable at all the temperatures. The isomer-12 is shown in Fig. 3.9. On comparing the core structure of GM and the most probable isomer, a difference in the arrangement of atoms can be clearly observed as shown in Fig. 3.10. The most probable isomer has a more symmetric core, therefore, its probability is the greatest at all the temperatures considered. The probability of GM along with the most probable isomer at different temperatures is given in Table 3.4. Isomer number 14 and 20 have an equal probability at temper-

Table 3.4. Probability of GM and most probable structure of Au_{147}

T (K)	$P_{GM}(\%)$	$P_{mostprobable}(\%)$
300	7.1	8.50
500	4.17	7.90
800	2.8	7.19

ature 800 K, so the properties of a Np cannot be predicted by considering just one isomer. The most probable or nearly probable isomers have to be considered for studying the dynamics of a Np at a particular temperature. The probable isomers show a stark difference in the arrangement of their core structure, some of which are shown in Fig. 3.11. It can be inferred that though Au_{147} does not exhibit Ih geometry, but the GM and the most

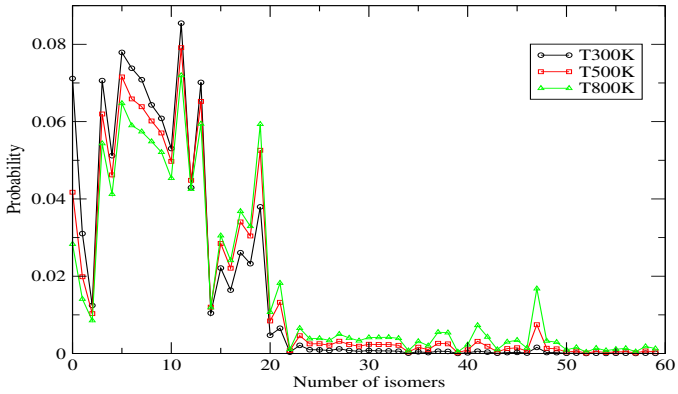

Figure 3.8. Probability plot of all the isomers of Au_{147}

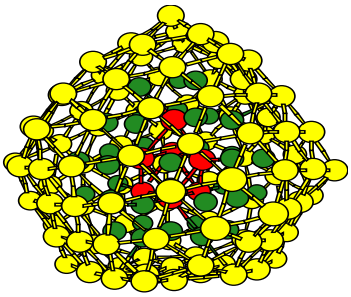

Figure 3.9. Most probable isomer at 300 K, 500 K, 800 K

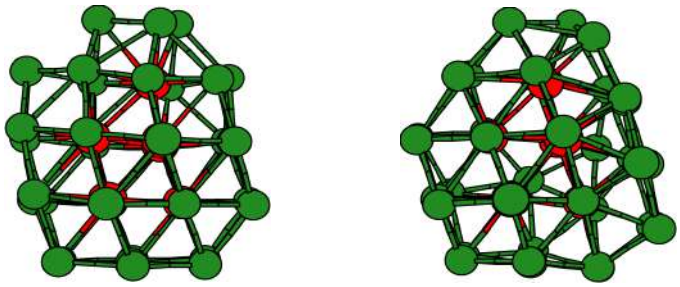

a) b)

Figure 3.10. Core structure of Au_{147} a) Most probable isomer, b) GM

probable isomer have a symmetry in their structures.

3.3.8 Fluxionality in Au_{147}

Gold clusters exhibit an interesting property, *fluxionality*, by virtue of which the atoms in a molecule are in a state of motion such that, many low lying isomers exists at a particular temperature with a minimal energy difference between them. In a core-shell structure, the fluxionality can be due to a dynamic surface or a dynamic core. So, to study fluxionality in

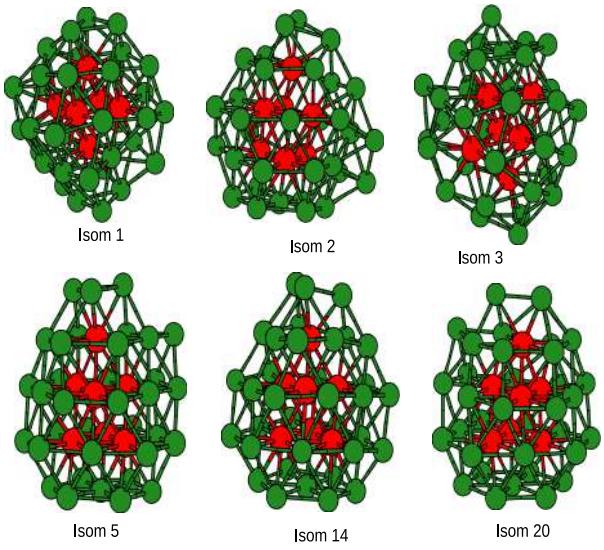

Figure 3.11. 42 atom core of some low lying isomers of Au_{147}

Au_{147}, MD simulations are run at three temperatures - 300 K, 400 K, 700 K. Generally, the chemical reactions are carried out at room temperature, therefore, the dynamics of the GM is studied at 300 K. For getting a broader picture of the structural evolution with temperature, 400 K and 700 K temperature are also considered. The simulations are run at a time step of 3 *fs* for a time duration of 1 *ns* . The advantage of studying gold's fluxional behaviour is that it plays an important role in surface mediated reactions like catalysis.[186, 187, 188, 189, 190, 191] The fluxionality in smaller gold clusters has been investigated earlier[192, 193, 194]. A high fluxionality in Au_{147} clusters is observed. It is noticed that the core atoms are highly mobile at 400 K, and both surface and core atoms are in a constant motion at 700 K.

To study the movements in the structures as the simulation is processed, order parameters can be calculated. The order parameters implemented in the current study are average fluctuations in the bond length,[184] volume variation in the cluster,[184] root mean square distance (RMSD)[192] and atomic equivalence index (AEI).[195]

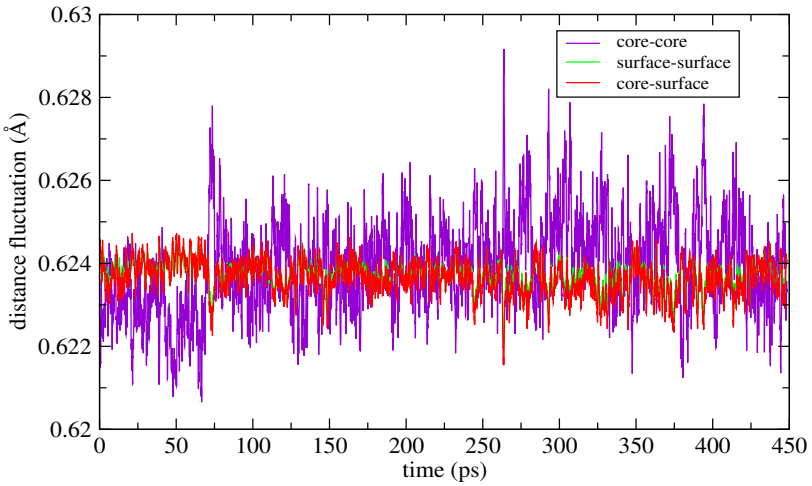

Figure 3.12. Average bond length fluctuations of Au_{147} at 400 K

Average bond length fluctuation

The average bond length fluctuations[184] with time is estimated for the MD trajectory of Au_{147} at 400 K. The plot of the distance fluctuations with respect to time elapsed is shown in Fig. 3.12. In the plot, the fluctuations in core-core atoms, surface-surface atoms, and core-surface atoms is represented by purple color, green color and red color respectively. From the plot, it can be inferred that core exhibits large fluctuations as compared to surface of Au_{147} with the simulation time. Due to these fluctuations in core, there is a change in the coordination number between surface and core atoms, providing an evidence of rotation of the core atoms unit. So, from average distance fluctuation calculations at 400 K, it can be concluded that due to rotations and vibrations in core, Au_{147} shows fluxionality.

Volume variation

As the Nps are non-speherical, their volume is calculated as

$$V = \frac{4}{3}\pi R_1 R_2 R_3 \tag{3.7}$$

where, the three radii of Np is calculated using moment of inertia (I) and total mass (M) of the Np.

$$R_a = \sqrt{\frac{5}{2}}\sqrt{\frac{I_a}{M}} \qquad (3.8)$$
$$a = 1, 2, 3$$

The volume variation[184] in Au_{147} clusters is calculated for MD simulation trajectories at 300 K, 400 K and 700 K. The plot is shown in Fig. 3.13. In Fig. 3.13, the volume variation for temperature 300 K, 400 K and 700 K is represented by black color, red color and green color respectively. From the plots at 300 K and 400 K, it can be inferred that there is not much volume variation in the structures, such that, no major movements are observed throughout the MD trajectory at these temperatures i.e., the structures formed along the simulation does not show large variations with respect to GM. However, at temperature 700 K, a lot of volume variation is observed. The structure of the GM is completely disturbed and a large deviation in structures is observed. The atoms are highly mobile and the structure changes a lot as can be seen from Fig. 3.13. Highest variation in the volume is observed in structure a,b,d in Fig. 3.13(b), where the clusters are more distorted as compared to our GM. Also, structure c and e in Fig. 3.13(b) have a low variation in volume, and thus are near to GM geometry.

RMSD

The RMSD[192] of the clusters corresponding to the GM structure at temperature 300 K and 700 K. Different peaks in the RMSD plots does not confirm the presence of entirely different configurations. It is a parameter to show that the atoms are moving and are not static.

$$RMSD_{conformation} = \sqrt{\frac{\sum_{i=1}^{atoms}(x_i - x_i^c)^2 + (y_i - y_i^c)^2 + (z_i - z_i^c)^2}{N}} \qquad (3.9)$$

where, x_i, y_i, z_i are the coordinates of the GM and x_i^c, y_i^c, z_i^c are the coordinates of the conformation obtained from MD trajectory, N is the

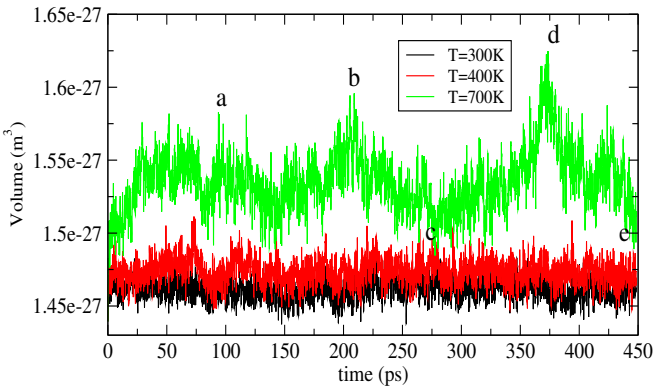

(a)

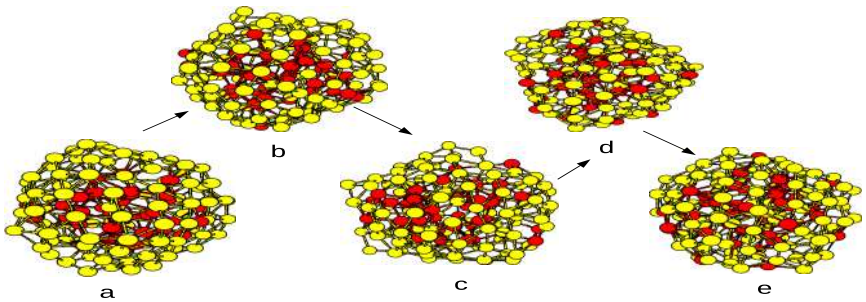

(b)

Figure 3.13. (a) Volume variation of Au_{147} at 300 K, 400 K, and 700 K and (b) Structural evolution with simulation time at 700 K

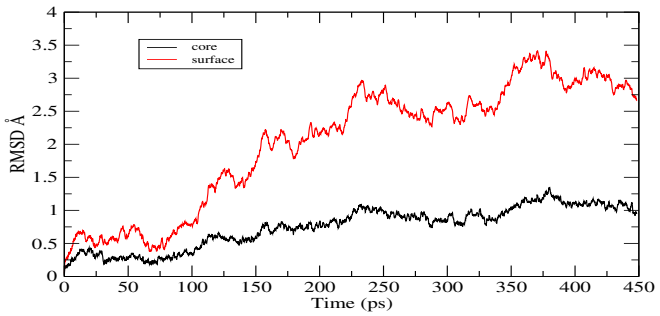

(a)

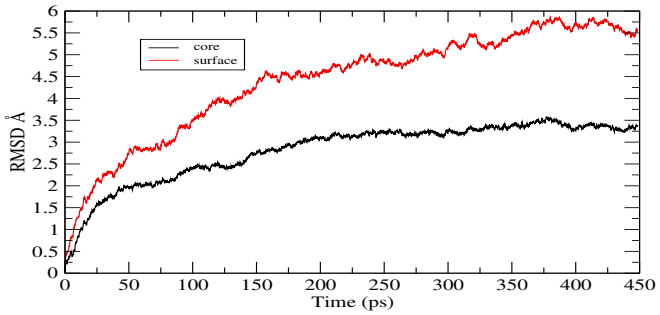

(b)

Figure 3.14. RMSD plot of Au_{147} a) 300 K b) 700 K

number of atoms in the conformation. The relevance of RMSD is that the atomic positions are numbered such that after every time step they change the position which can then be compared with the initial structure. Therefore, we can observe how the structure is evolving as the simulation is processed. From the RMSD plots shown in Fig. 3.14, it is observed that the core and surface atoms are continuously moving with the simulation time. At 300 K, the RMSD of core atoms is low (Fig. 3.14a) as the structural variation of core is less, so the movements are confined in a smaller region. On other hand, surface atoms have a large phase space for movement, therefore, RMSD is higher for surface atoms. At 700 K, the initial symmetry of the structure is destroyed within 1 *ps* of the simulation. Since, volume variation (Fig. 3.13a) is high at 700 K, therefore, the core and surface atoms are showing a steep increase in RMSD with the simulation time. So, from RMSD , it is concluded that Au_{147} atoms are in a state of motion with the simulation time and therefore, shows fluxionality.

AEI

AEI is atomic equivalence index that shows the movement of an atom with respect to other atoms in a cluster. During a simulation, atoms exhibit two types of movements- within the layer and migrating to other layers. AEI shows the movement of atoms as the simulation progresses. AEI ($\varrho_i(t)$) is calculated using position vector $\overrightarrow{R}$ of an atom (i) with respect to other atoms (j) at time t.

$$\varrho_i(t) = \sum_{j \neq i}^{N} |\overrightarrow{R}_i(t) - \overrightarrow{R}_j(t)| \tag{3.10}$$

The GM structure of Au_{147} consists of three layers- inner core, middle layer, surface. So, to visualize the behaviour of atoms with progress in simulation, few atoms are randomly selected from the surface and few atoms from the core and their AEI is calculated. The AEI is calculated for Au_{147} at 300 K and 700 K. At 300 K, the AEI plot (Fig. 3.15(a)) shows three distinct region in which the bottom region refers to inner core atoms, middle region refers to middle core and the top region refers to surface atoms. So, it can be inferred that core atoms remain in the core and surface atoms remain on the surface. The atoms are not getting exchanged between the layers. At 700 K, in Fig. 3.15(b), it is observed that now the three layers atoms are showing an intermixing. One of the core atom, represented by the blue color curve, moves from core to surface in the beginning of simulation and again goes back to core after a few time steps. On further increase in simulation time, it completely goes to surface and then stays there. Similarly, some of the surface atoms are coming inside the core as seen from grey and brown colored plot in the Fig. 3.15b. The atom represented by brown color initially stays on the surface, but after some time, it breaks into the core and stays there. So, a core to surface and surface to core atom movement is observed. Therefore, it is concluded that the atoms are getting exchanged between core and surface throughout the simulation.

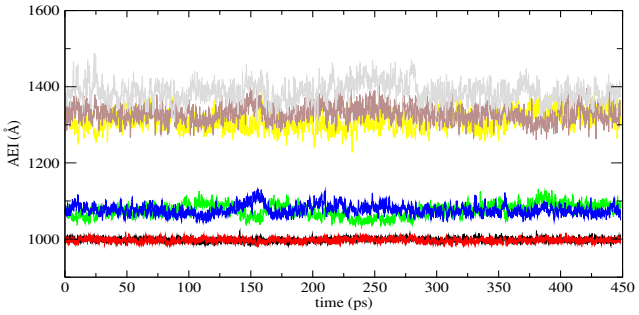

(a)

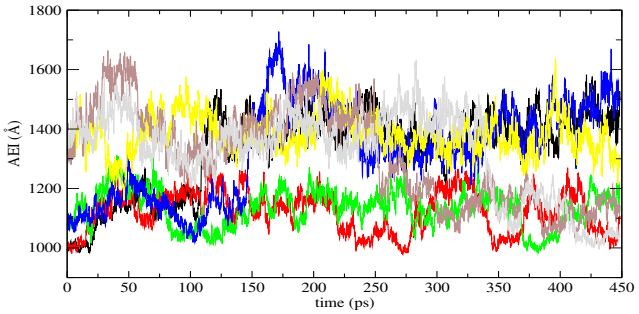

(b)

Figure 3.15. AEI plot of Au_{147} a) 300 K b) 700 K

3.4 Summary

In summary, the PES for gold clusters ranging from $Au_{30} - Au_{147}$ with an RMS error of 5 meV/atom for energy and 84 meV/Å/atom for force calculations is successfully fitted. The spherical harmonics applied in the form of power spectrum for describing the atomic environment and using it with NN provides a highly efficient system for fitting the PES of a nanocluster. The computational time for accurate calculation of energy and forces of a single Au_{147} cluster is reduced to ∼1.7 seconds, which is very fast when compared to DFT (∼7 hours). An extensive GM search is performed along with MD simulations for Au_{147} at different temperatures. It is found that a large number of isomers are possible that lie within a narrow energy scale of 0.5 eV from the GM. The Au_{147} GM consists of a symmetric core and an unsymmetric surface unlike Ih which is a highly symmetric structure. It is also confirmed that GM of Au_{147} is found to be 4 eV lower in energy than the Ih geometry from the DFT calculations. As found in many other gold clusters, Au_{147} also exhibits fluxionality and its observed that it has a dynamic surface as well as a dynamic core.

Chapter 4

Exploring the PES of Au_{147} using Bispectrum descriptors

4.1 Introduction

In chapter 3, the second order invariants - power spectrum was applied to fit the PES of gold nanoclusters. It was seen that although being a magic number cluster, Au_{147} prefers an amorphous geometry as the GM. For further studying the structural arrangements using NN potentials, the modeling of atomic density can be improved by considering third order invariants- bispectrum. Bispectrum has the efficiency of carrying more information of the density than power spectrum. The bispectrum is a higher order invariant than the power spectrum, so its spherical harmonics expansion carries more information and gives a more accurate representation of the atomic environment.

In this chapter, the atomic environments are modelled using bispectrum descriptors. For comparison between the efficiency of power spectrum and bispectrum, the NN potential is fitted up to Au_{147} in this study. An algorithm is also proposed for selecting the frequencies that need to be coupled for extracting the phase information between different frequency bands. It is found that higher order invariant like bispectrum is highly efficient in exploring the PES as compared to other invariants.

4.2 Computational details

The dataset ($Au_{30} - Au_{147}$) constructed in the previous chapter is utilized in this work for training the NN potential (training set: 9050 clusters, test set: 1086 clusters). The descriptors are calculated for the entire dataset. The atomic environment descriptors consists of 9 radial functions given by Eq. 2.29 and 15 bispectrum coefficients given by Eq. 2.73. As discussed in chapter 2, l_1 and l_2 varies from 0 to 4 and l varies from $|l_1 - l_2|$ to $l_1 + l_2$. A total of 35 combinations are possible, out of which 15 coefficients are selected having a bicoherence value between 0.3 to 1.0. The c_{lm} is given by Eq. 2.42. The number of neurons in both the hidden layers is 30. KF was used as the weights optimization algorithm.

Weighting of ADF: For power spectrum coefficients, the weighting of ADF is done in order to differentiate between atoms lying very far and very near to the reference atom. The results generated using weighted density function in bispectrum did not give a low prediction error as the number of coefficients increases a lot when compared to non-weighted density function in bispectrum. So, to reduce the input coefficients and keeping the prediction accuracy, the weighting is not done in calculations of bispectrum coefficients. For checking the ability of descriptor to detect small movements, an atom of a Au_{147} cluster was selected. The atom was displaced towards one of its neighbour and the bispectrum and power spectrum coefficients were calculated. Similarly the atom was displaced away from that neighbouring atom and the coefficients were calculated. The values of the coefficients are plotted as shown in Fig. 4.1. It is observed that the changes in the values of the coefficients is much pronounced in non-weighted bispectrum coefficients. Comparing Fig. 4.1(a) and 4.1(c), it can be inferred that the sensitivity in identifying small changes in the structure is high in bispectrum as compared to power spectrum. Weighting of the density function in bispectrum only increases the number of coefficients and also some of them does not capture the change as observed in Fig. 4.1(b). Therefore, a non-weighted density function is used in bispectrum

as an efficient descriptor.

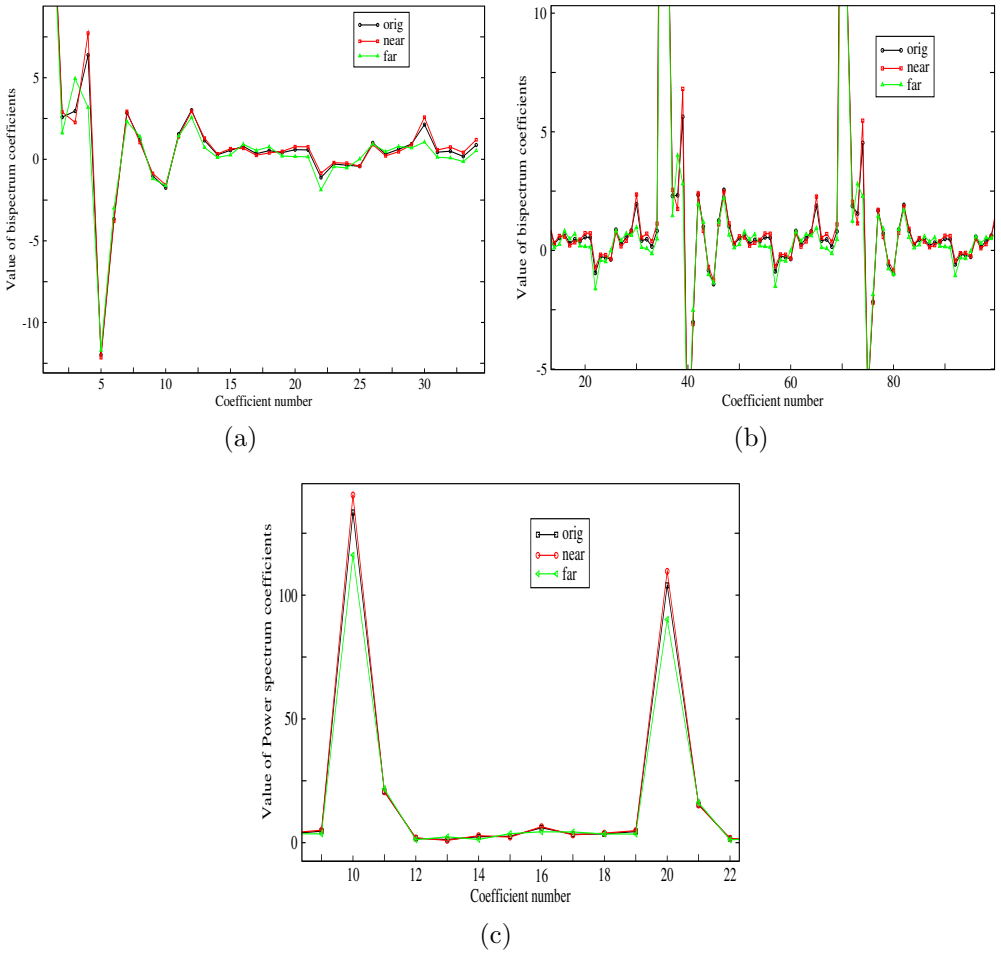

Figure 4.1. Descriptor plots a) Bispectrum coefficients without weighting the ADF, b) Bispectrum coefficients with weighting the ADF, c) Power spectrum coefficients

4.3 Results

4.3.1 Selection of coefficients

In order to select the number of coefficients, many trials using different number of input coefficients into the NN was performed. In the first trial, all the 35 bispectrum coefficients along with 9 radial functions for an atom was fitted. The RMS error in prediction of energy and forces was 5.5 meV/atom and 114 meV/Å/atom, respectively. These weights were validated on the test set. It was observed that these weights are efficient in predicting

correct energy and forces for Au nanoclusters. In order to decrease the number of coefficients further, 15 bispectrum coefficients corresponding to the top 15 values (among the 35 coefficients) of bicoherence along with 9 radial functions were taken. On fitting these coefficients for the same data set, an RMS error of 5.3 meV/atom and 110 meV/Å/atom in energy and forces prediction was obtained, respectively. Further, these weights were validated and it was observed that there is a good agreement between the NN and DFT predicted energies. Based on these observations, the number of input coefficients were restricted to 24 $(15 + 9)$ for describing an atomic environment.

As the number of coefficients in power spectrum were 59, and in bispectrum it is 24, a comparison in the computational time was done. The time taken for calculation of energy and forces for a Au_{147} cluster (147 atoms) is 7 seconds using bispectrum-NN, 3 seconds using power spectrum-NN and 7 hours using DFT on a single CPU (GenuineIntel 2600.0 MHz). The computation time is higher for bispectrum as it's a third order invariant. In choosing between the power spectrum or the bispectrum, there is a tradeoff between accuracy and computing time.

4.3.2 Validation of NN weights

In order to validate the weights obtained using 24 coefficients per atom in bispectrum-NN model, RMS error in energy for the testing set clusters is plotted in Fig. 4.2. From the plot, it can be seen that 40.69% of clusters lie above the average RMSE and 59.3% of clusters lie below the average RMS error. The majority of the clusters lie below an RMS error of 10 meV/atom. Only a few clusters exhibit large errors in energy. So, bispectrum NN can be trusted in practice for an approximate prediction of energy and forces for a cluster. The relative efficiency of DFT with power spectrum and bispectrum is compared for a set of 36 clusters of Au_{147} selected from MD trajectories at 300 K and 400 K. From Fig. 4.3, it can be inferred that bispectrum is more efficient than power spectrum as the predictions from

bispectrum and DFT are in good agreement with each other.

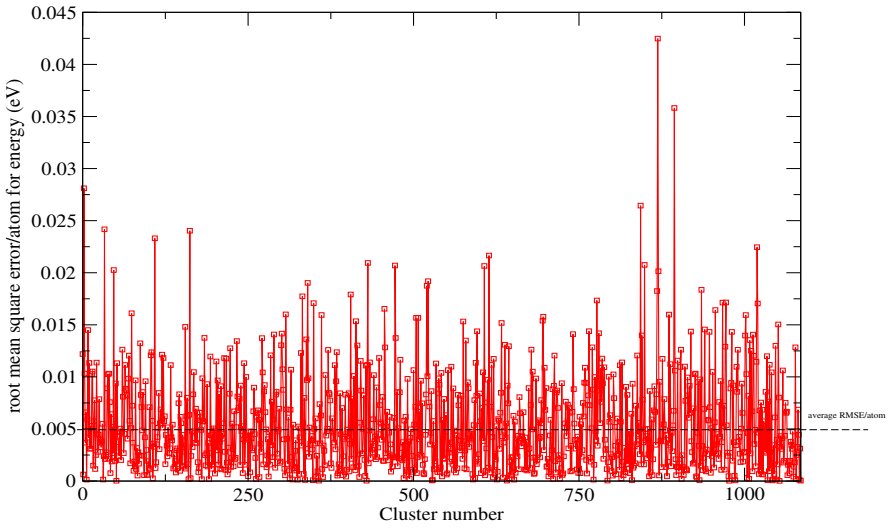

Figure 4.2. The validation set RMS error/atom in energy for $Au_{30} - Au_{147}$ clusters

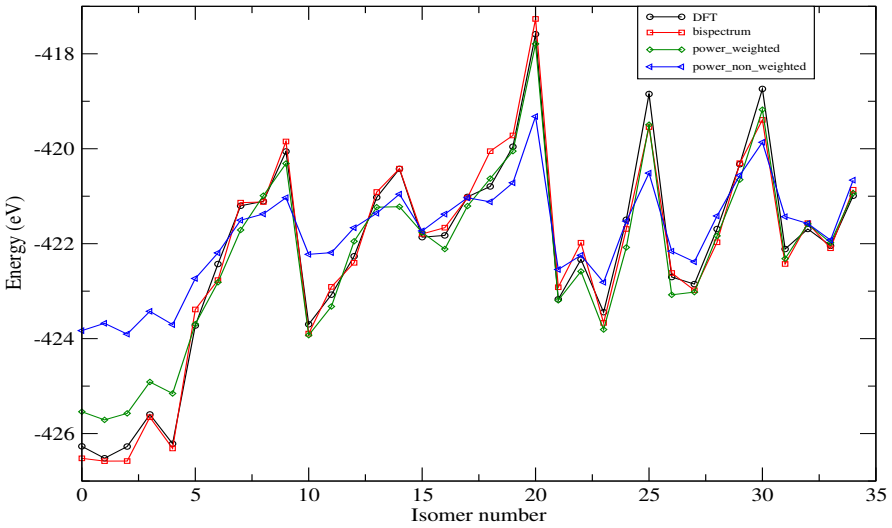

Figure 4.3. Comparison of energy prediction from DFT, bispectrum, weighted and non-weighted ADF in power spectrum for a set of Au_{147} clusters

4.3.3 Exploring PES of Au_{147} nanocluster via global optimizations

In order to test the PES exploration of bispectrum, global optimization using the NN weights fitted for bispectrum coefficients is performed. The initial structures for running the optimizations are taken form the work

done in chapter 3. BH algorithm[168] was used for finding new minimas. For energy minimization L-BFGS[73] algorithm was applied. Around 20 different initial structures were taken and the optimization were performed for 30000 steps for each structure. In order to explore various possible structures, a lot of structural perturbations were induced via BH during the optimization. Doing so, many potential wells can be identified. Using BH, a lot of isomers were obtained in an energy range of 6 eV. A histogram is plotted in Fig. 4.4 to show the number of isomers obtained in different energy ranges.

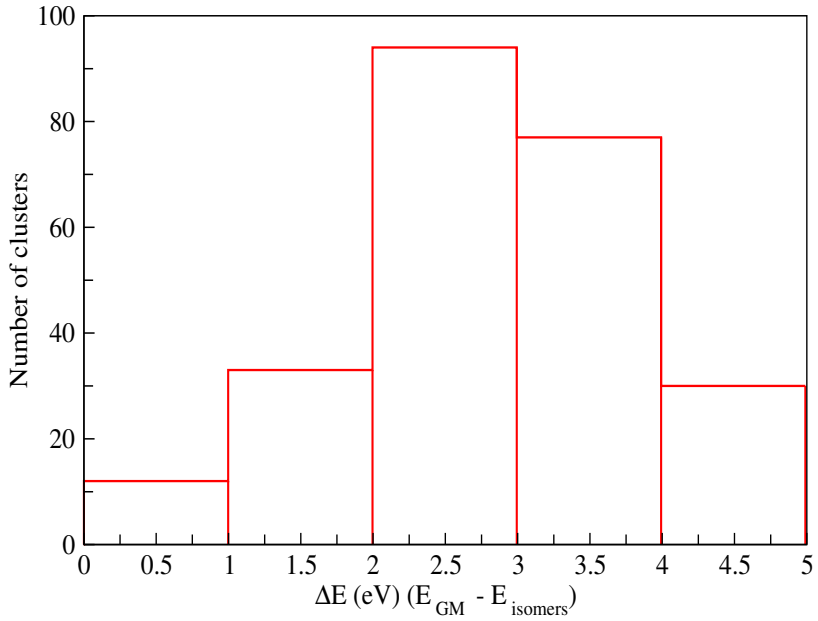

Figure 4.4. Number of clusters of Au_{147} belonging to various energy range

A lot of isomers of Au_{147} consisting of 105 atoms on the surface and 42 atoms in the core were obtained. The core comprises of two layers - inner core and secondary core. Inner core atoms vary from 6 to 8 and secondary core atoms vary from 36 to 34 in the various isomers obtained. In comparison to the series of isomers obtained using power spectrum in chapter 3, some new inner core geometries are generated from bispectrum. Structures with 6 inner core atoms and other isomers were not identified during the optimization done using power spectrum[134].

Geometries of different inner core structures are shown in Fig. 4.5. The difference is in the atomic arrangement in all the isomers although a

symmetry is maintained in the structures.

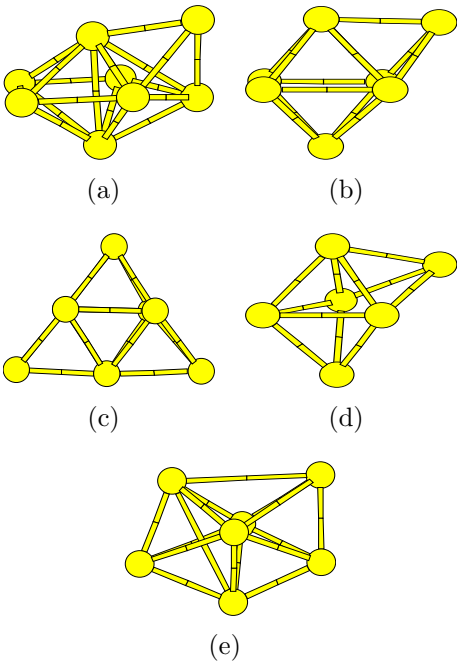

Figure 4.5. Inner core structures for different isomers of Au_{147} (a) 8 atoms: *capped pentagonal bi-pyramidal shape*, (b) 7 atoms: *capped square bi-pyramidal shape*, (c) 8 atoms: *pyramidal shape*, (d) 6 atoms: *capped trigonal bi-pyramidal shape*, (e) 7 atoms: *star shape*.

Since bispectrum captures the atomic environments in an improved way, the purpose behind performing the global optimizations on Au_{147} is to bring out the difference in the exploring PES capabilities of power spectrum and bispectrum. The aim is accomplished by discovering a lot of different structures from bispectrum within a narrow energy range of 0.3 eV.

The GM remains the same as predicted by power spectrum which contains 7 atoms inner core as shown in Fig. 4.6(b). Other isomers obtained lie very near in energy to the predicted GM as seen in Table 4.1. According to DFT as well as ANN, Fig. 4.6(b) represents the GM structure. It consists of a capped square bi-pyramidal shape inner core. The isomer shown in Fig. 4.6(c) consists of 8 atoms in the inner core which forms a stable pyramidal geometry thus lying 0.24 eV (DFT) higher than the GM. The energies predicted by ANN are not exactly accurate as those predicted by DFT since the converged weights error for energy prediction is 5.3 meV/atom ($\sim$ 0.78 eV for Au_{147}). Another isomer that lies just 0.25 eV

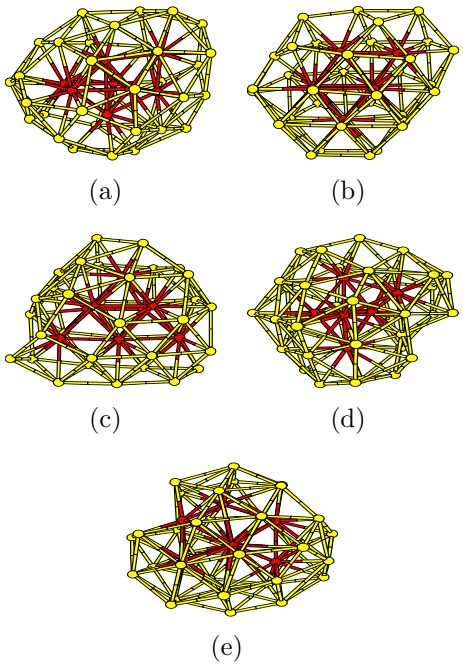

Figure 4.6. Core structures (42 atoms) for different isomers of Au_{147} (a) Contains 8 atoms in the inner core, (b) Contains 7 atoms in the inner core, (c) Contains 8 atoms in the inner core, (d) Contains 6 atoms in the inner core, (e) Contains 7 atoms in the inner core.

(DFT) higher than GM exhibits a capped pentagonal bi-pyramidal shaped inner core as shown in Fig. 4.6(a). Isomer shown in Fig. 4.6(e) lies 0.3 eV (DFT) higher than GM and exhibits a star shaped inner core.

Power spectrum is computationally cheaper than bispectrum, but it's less efficient in exploring the PES. Therefore, there is a trade off in accuracy and computational time for using these high order invariants as descriptors.

Table 4.1. Relative energy of GM with respect to other isomers of Au_{147}

Structure	Fig. 4.6(a)	Fig. 4.6(c)	Fig. 4.6(d)	Fig. 4.6(e)
ΔE_{DFT} $(E_{GM} - E_{isom})$ (eV)	0.2513	0.2468	0.9226	0.3048
ΔE_{ANN} $(E_{GM} - E_{isom})$ (eV)	0.0591	0.0019	0.9256	0.2685

4.4 Summary

In this work, higher order invariants - bispectrum are used to describe an atomic environment. Along with radial functions, they are given as an input to ANN to predict the energy and forces of gold nanoclusters. As a lot of permutations are possible in the bispectrum coefficients, an algorithm is proposed to selectively choose the frequencies for coupling, in order to reduce the total number of input coefficients to ANN. The advantage of using bispectrum over power spectrum is in its ability to search the PES efficiently. A lot of new structures were obtained from MD simulations using bispectrum-NN potential. These structure were not identified during the simulations done using power spectrum-NN potential. As bispectrum is very sensitive, it can be used as a potential order parameter for calculating various properties of a nanocluster.

Chapter 5

Fitting the PES of gold-silver nanoalloys and thio- protected gold nanoclusters

5.1 Introduction

In chapter 3 and 4, a single NN was applied to fit the PES of gold nanoclusters. In order to fit the PES of a system having atoms of different elements, a new method is proposed here. The traditional approach for fitting the PES for a MC system using NN is to consider n networks for n chemical species in the system. This shoots the computational cost and makes it difficult to apply to a system containing different kinds of species. A new strategy of using a single artificial neural network(SANN) to compute the energy and forces of a chemical system is discussed here. Since atomic forces are significant for geometry optimizations and MD simulations for any chemical system, their accurate prediction is of utmost importance[196, 197, 198, 199, 200, 201]. To predict the atomic forces, the traditional way of fitting forces from underlying energy expression is modified and applied. The atomic force fitting has made it possible to train smaller size systems and extrapolate the parameters to make accurate predictions for larger systems making the approach transferable. This proposed strategy has definitely made the mapping and fitting of atomic forces easier and can be applied to a wide variety of molecular systems.

The key points of the proposed strategy are

(a) Due to a precise atomic force fitting, the ANN weights fitted for a small size system can be extrapolated to similar compositions in the larger size systems,

(b) The overall model is transferable in two ways - (i) It can be used to fit any Np's PES as we require just a dataset, from which, the inter-atomic distances, effective nuclear charges and reduced mass can be utilised to give an input to ANN, (ii) The weights are transferable for a chemical system to any size of the clusters of similar composition.

Since the complexity of a descriptor increases with the type of chemical species, therefore, the proposed technique is applied to two different systems - bimetallic nanoalloys made up of silver and gold atoms $(AgAu)_{55}$-$(AgAu)_{147}$, and thiol protected gold nanoclusters $Au_{13}(SH)_6$-$Au_{38}(SH)_{24}$. To study the dynamics of $Ag_{35}Au_{112}$ and $Au_{68}(SH)_{32}$, global optimizations and MD simulations are performed.

5.2 Computational details

5.2.1 Parameters for fitting $(AgAu)_{55}$ - $(AgAu)_{147}$

In order to generate training data for $(AgAu)_{55}$ - $(AgAu)_{147}$, an initial data consisting of $(AgAu)_{55}$ was generated using Gupta potential[40] as the inter atomic potential in MD simulations. After getting around 2500 clusters, an initial run of NN training was performed. Using the obtained set of NN weights, MD simulations was run at 300 K, 400 K, 500 K and 600 K at a time step of $1fs$ for $(AgAu)_{55}$ and $(AgAu)_{147}$. To avoid high computational costs for generating ab initio data of $(AgAu)_{147}$, around 1000 clusters of $(AgAu)_{147}$ are split into different atomic environments. A total data of 11,000 clusters was accumulated containing different compositions of $(AgAu)_{55}$ and various environments of $Ag_{35}Au_{112}$. The composition of 24 % of silver atoms is chosen for $(AgAu)_{147}$, as it promises to be catalytically dynamic.[202] The energy and forces calculations for the dataset was executed on VASP.[141, 142, 143, 144] Scalar relativistic effects and the

core electrons are taken care of by PAW method. Generalized gradient approximation and PBE[146, 147] functional is applied for treating electron correlations. Gamma k-point (1×1×1) mesh is used to sample the Brillouin zone. The threshold energy is set as 260 eV and the force convergence is set as 10^{-4}. A box length of $22 \times 22 \times 22\mathring{A}^3$ is applied for the entire dataset with a vacuum dimension of 11 Å. The dataset was split in a training set of 9,500 clusters and a testing set of 1,500 clusters. The number of inputs defining the environment for an atom was 59 which was obtained by taking l from 0 to 9 in Eq. 2.48. The n in Eq. 2.77 takes on 5 values in order to make the function fall smoothly with increasing interatomic distance. The n values are $0.0028, 0.0040, 0.0110, 0.0280$ and 0.059. The number of radial functions in Eq. 2.29 are taken as 9 values corresponding to ξ values- $0.005, 0.015, 0.0230, 0.038, 0.060, 0.090, 0.150, 0.260$ and 0.480. The number of hidden layer neurons were set to be 30. The $w_{\beta N}$ value for Au and Ag in Eq. 2.79 is calculated using Clementi - Raimondi[203, 204] effective nuclear charges.

5.2.2 Parameters for fitting $Au_m(SH)_n$

A diverse set of $Au_m(SH)_n$ clusters are taken in which m varies from 13 to 38 and n varies from 6 to 24 to fit the energy and forces. Since $Au_{13}(SH)_6$, $Au_{13}(SH)_8$, $Au_{13}(SH)_9$ and $Au_{15}(SH)_8$ are small sized clusters, the initial data containing these composition clusters were generated by MD simulations coupled with DFT as the interatomic potential. After getting an initial data, the NN weights are generated. These weights are then integrated with MD simulations for generating more data for the rest of the compositions in span of $Au_{13}(SH)_6$ to $Au_{38}(SH)_{24}$. Overall, 11,500 clusters are generated and divided into a training data set of 10,000 clusters and a testing data set of 1,500 clusters. The number of inputs per atom was kept to 59 for all the $Au_m(SH)_n$ clusters. The network for $Au_m(SH)_n$ also had 30 neurons in both the hidden layers. The $w_{\beta N}$ values for Au, S and H in Eq. 2.79 is calculated using Clementi - Raimondi[203, 204]

effective nuclear charges.

5.3 Results and discussion

Note: In AgAu figures: Au is represented by yellow and Ag is represented by red.
In Au(SH) figures: Au is represented by yellow, S is represented by red and H is represented in white.

5.3.1 Silver-Gold nanoalloys: Study of $Ag_{35}Au_{112}$

On fitting the energy and forces with the proposed approach, an average RMS error of 5.9 meV/atom and 74 meV/Å/atom for energy and atomic forces, respectively, was achieved. In order to verify the prediction capability of the weights, the DFT and NN energies are calculated for a small set of 500 clusters. The energy per atom for all the clusters is plotted in Fig. 5.1(a) and the absolute value of the difference between DFT and NN energies is plotted in Fig. 5.1(b). The components of forces predicted from NN and DFT for the training and testing set clusters is compared, as shown in Fig. 5.2. The correlation observed between the predicted NN and DFT forces reflects the accurate fitting of atomic forces for a MC system by the proposed approach. For making the point more relevant, the x component of force for three different composition and size clusters- $Ag_{13}Au_{33}$, $Ag_{15}Au_{69}$ and $Ag_{19}Au_{38}$ is plotted as shown in Fig. 5.4. To validate the efficiency of the fitted energy and forces for the bimetallic system, geometry optimizations and MD simulations are performed. An initial structure of $Ag_{35}Au_{112}$ consisting of three layers of atoms arranged in Ih geometry with silver atoms occupying the middle core and rest of the structure containing the gold atoms as shown in Fig. 5.3 is taken. Such an arrangement is chosen as it is already studied[202, 205] that in Au rich nanoalloys, gold atoms occupy surface and core atoms. The MD simulations were ran at different temperatures - 300 K, 400 K, 500 K and 600 K. A time step of 1 fs was

used and the simulations were ran for a total time of 1 *ns*. Since $(AgAu)_{147}$ is a large system, *ab initio* MD simulations have not been performed yet. Various studies[205, 206] have been done using empirical potentials but they lack the QM accuracy. The optical absorption spectra[207] has been studied using first principles but dynamics has not been explored.

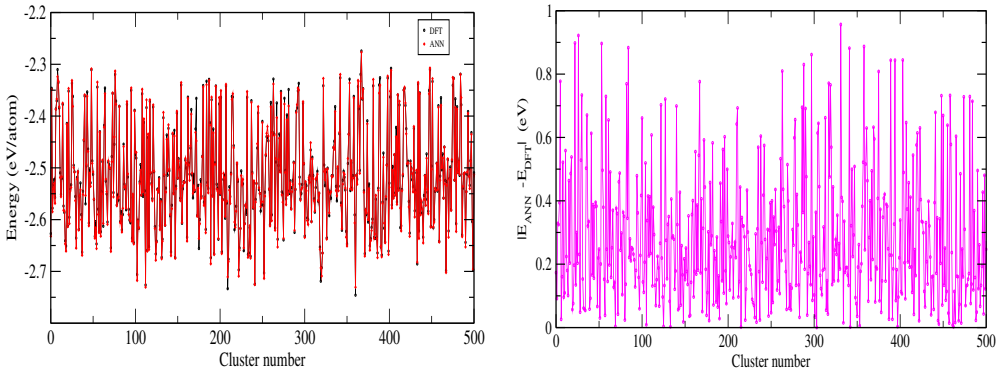

(a) (b)

Figure 5.1. (a) Comparison of DFT and ANN predicted energies for $(AgAu)_{55}$ - $(AgAu)_{147}$, (b) Plot showing the absolute value of $|E_{ANN} - E_{DFT}|$ for $(AgAu)_{55}$ - $(AgAu)_{147}$

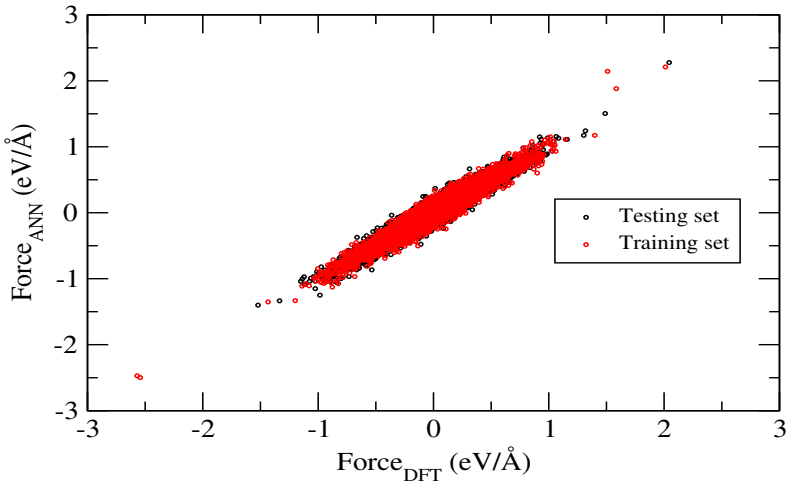

Figure 5.2. Correlation plot of ANN and DFT predicted atomic force components for testing and training set of $(AgAu)_{55}$ - $(AgAu)_{147}$ clusters

It has been observed that with time the Ih geometry is completely destroyed and there is a huge variation in the atomic arrangement. At 300 K, the initial structure is maintained for a time of 13 *ps*, and then silver atoms start to move towards surface. The gold atoms are too in a state of continuous rotational and vibrational motion but the geometry of

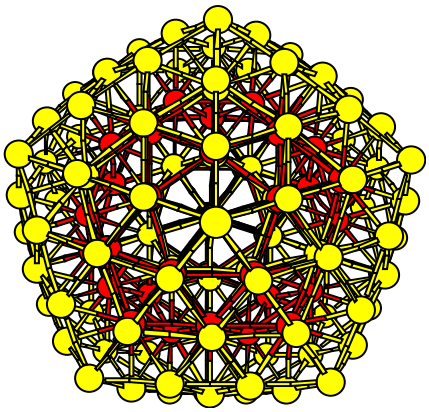

Figure 5.3. Initial structure of $Ag_{35}Au_{112}$ for MD simulations

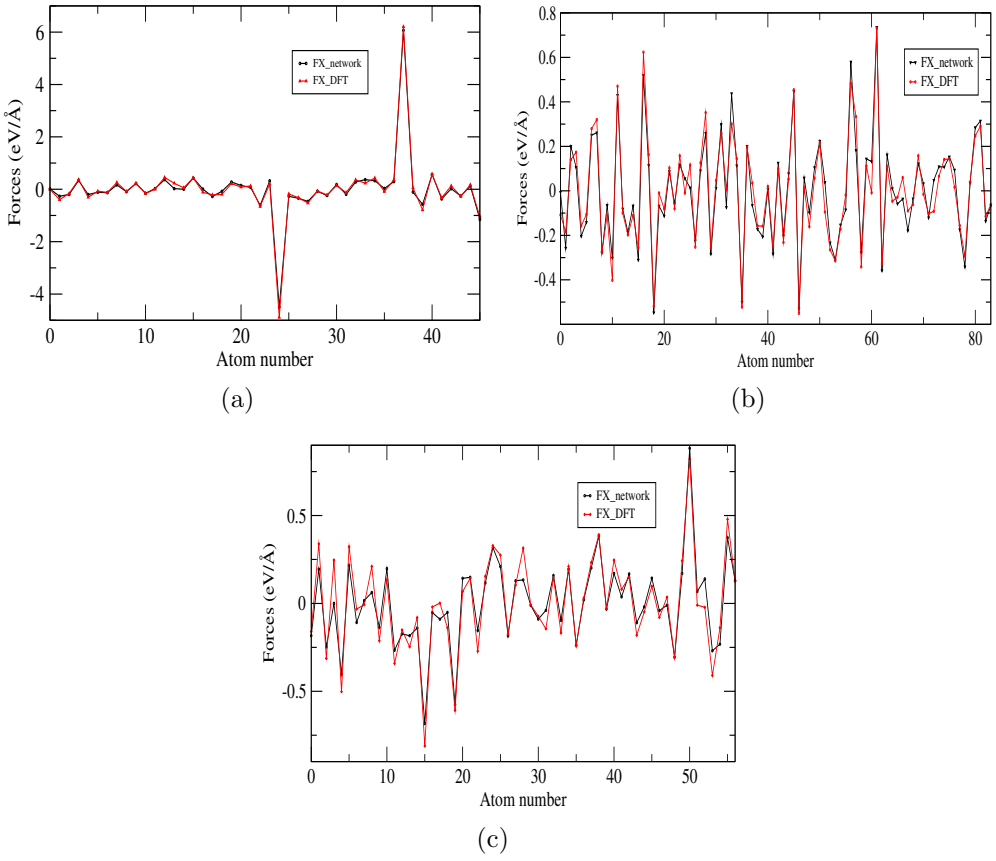

Figure 5.4. Plot of X component of force for (a) $Ag_{13}Au_{33}$, (b) $Ag_{15}Au_{69}$, (c) $Ag_{19}Au_{38}$

inner core is maintained as such. As the simulation time is progressed, the geometry of the inner core changes from 13 gold atoms to 10 gold atoms and the middle core atomic arrangement alters from 42 atoms to 37 atoms comprising of both silver and gold atoms. Overall the surface atoms increases from 92 to around 100 atoms. This atomic arrangement of 100-37-10 is almost similar to the atomic arrangement in the GM structure

of Au_{147} as shown in chapters 3 and 4. It shows that Ih geometry is not favored in pure gold or gold rich clusters. As simulations are performed at higher temperatures, it is observed that more silver atoms are moving from middle core to the surface. One of the interesting observation is that the silver atoms never entered the inner core. They either occupied the middle core or lied on the surface. Also, at a temperature of 600 K, almost all the silver atoms enriched the surface which is in accordance with the results for 24 % composition of Ag in $(AgAu)_{55}$ as published by Chiriki et al.[202] The structure obtained at 600 K is shown in Fig. 5.5 in which the surface enriched with Ag can be seen.

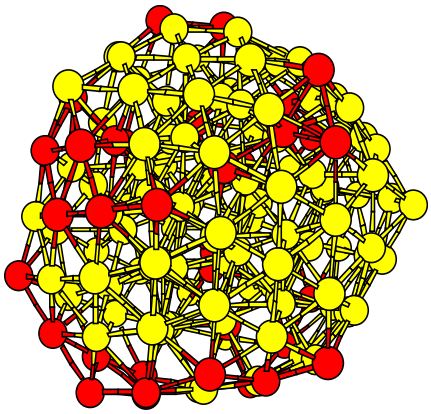

Figure 5.5. Structure of $Ag_{35}Au_{112}$ obtained at 600 K

To study the movements in the cluster with simulation time, RMSD[192] is calculated as the order parameter. It calculates the average distance an atom has moved from the initial structure. For a structure at a given time, a sum over all the atomic movements is taken and divided by the total number of atoms in the structure.

$$RMSD = \sqrt{\frac{\sum_{v=1}^{atoms}(x_v - x_v^s)^2 + (y_v - y_v^s)^2 + (z_v - z_v^s)^2}{N}} \tag{5.1}$$

In Eq. 5.1, x_v, y_v and z_v are the Cartesian coordinates of the initial structure and x_v^s, y_v^s and z_v^s are the Cartesian coordinates of the structure at a given simulation time. The RMSD plots at 300 K, 400 K, 500 K and 600 K is shown in Fig. 5.6. It can be inferred that both the core atoms and the surface atoms of $Ag_{35}Au_{112}$ undergo a lot of movements thus making

it a highly fluxional cluster. With the increase in simulation time, it is observed in all the temperatures that both surface and the core atoms try to attain the geometry as of initial structure, but since that structure is not stable, the geometry changes to a more stable arrangement of atoms.

In order to show the inter mixing of atoms between surface and core at 600 K, AEI[195] is plotted. It is a very sensitive indicator and maps even the tiny movements throughout the simulations. Since it's a 147 atom cluster, it is not possible to plot the AEI for all the atoms. So, 4 atoms were selected from the structure in which two are the core atoms and other two are surface atoms. The plot is shown in Fig. 5.7. There is a continuous movement of the core atom to the surface and back to the core, as seen by the blue colored curve in Fig. 5.7. The surface atoms are moving but not entering the core as observed from the red and the black colored curves in Fig. 5.7.

After running the MD simulations for 1 *ns*, the local minima structures are collected from the trajectories obtained at different temperatures. The geometry optimizations is performed using L-BFGS algorithm[73]. From optimizations, a few symmetric inner core geometries is obtained as shown in Fig. 5.8. The lowest energy isomer that is quenched from the MD trajectories is shown in Fig. 5.9(a). It contains 10 atoms in the inner core, 37 atoms in the middle core and 100 atoms on the surface. From the initial structure of MD simulations, 5 silver atoms moved to the surface forming the lowest energy isomer. Another isomer with 9 atoms in the inner core, 36 atoms in the middle core and 102 atoms on the surface is shown in Fig. 5.9(b). There was a difference of 0.39 eV between the two isomers, showing a possibility of large number of fluxional isomers for $Ag_{35}Au_{112}$. Overall, a cage like structure makes the foundation of gold rich $Ag_{35}Au_{112}$ alloy.

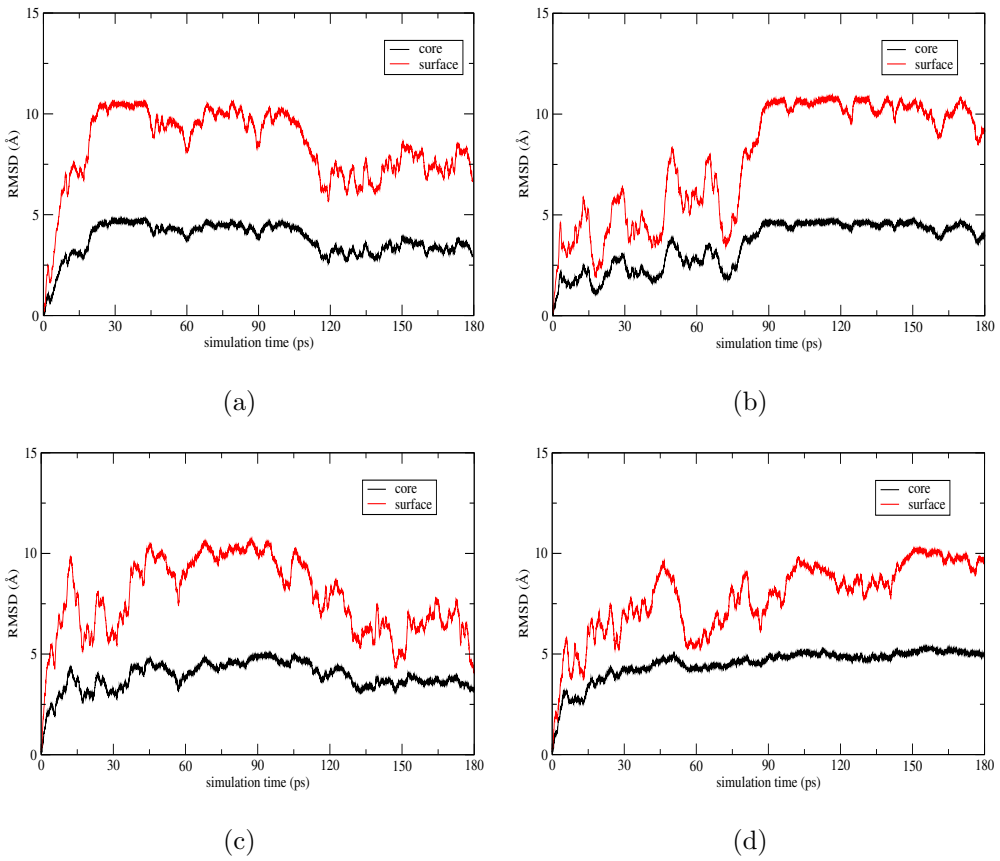

Figure 5.6. RMSD plots for MD simulations of $Ag_{35}Au_{112}$ at (a) 300 K, (b) 400 K, (c) 500 K, (d) 600 K

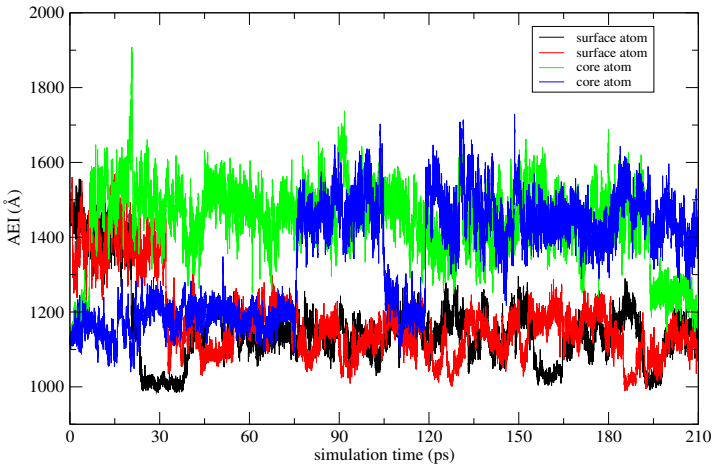

Figure 5.7. The AEI of two core atoms and two surface atoms in $Ag_{35}Au_{112}$ throughout the MD simulations at 600 K

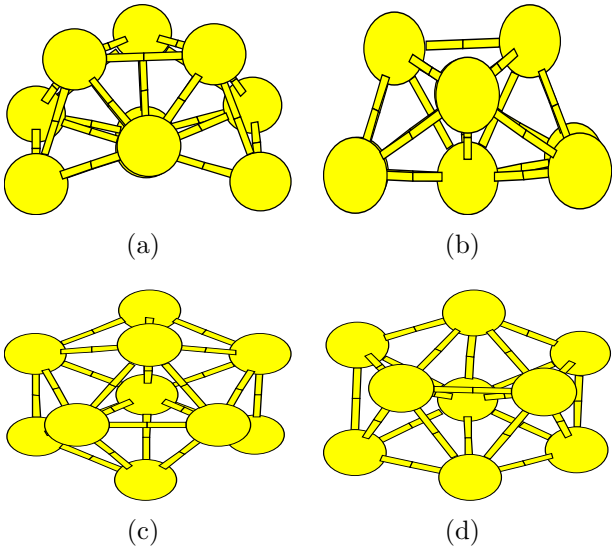

Figure 5.8. The inner core geometry for $Ag_{35}Au_{112}$ (a) 10 atom inner core (side view), (b) 9 atom inner core (side view), (c) 10 atom inner core (top view), (d) 9 atom inner core (top view)

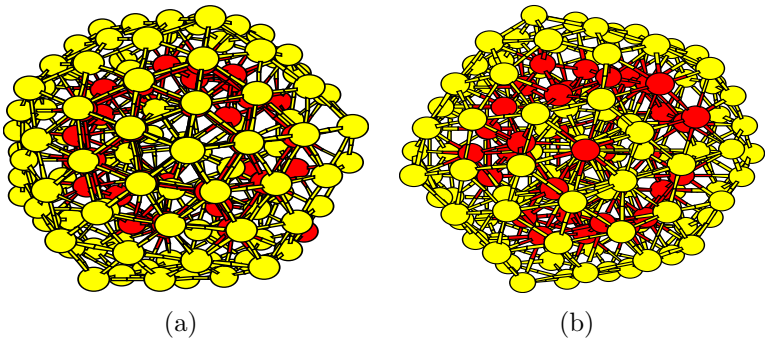

Figure 5.9. (a)The lowest energy structure quenched for $Ag_{35}Au_{112}$, (b) The structure consisting of 9 atom inner core and lying 0.39 eV higher in energy than lowest energy structure of $Ag_{35}Au_{112}$.

5.3.2 Thiol protected gold nanoclusters: Study of $Au_{68}(SH)_{32}$

The thiol protected gold nanoclusters are considered for validation of the proposed method due to the increased complexity in the structure. The gold, sulphur and hydrogen atoms have different valence electrons and orbital configuration which leads to different patterns of bonding between each other. Therefore, using the descriptors an accurate prediction of the forces is a challenge. On fitting the dataset consisting of clusters from $Au_{13}(SH)_6$-$Au_{38}(SH)_{24}$, an average RMS error of 8.6 meV/atom for en-

ergy of a cluster and 176 meV/Å/atom for atomic forces was obtained. The reason for getting a higher RMS error as compared to gold-silver nanoalloys is the huge variations in thiol protected gold clusters which makes it difficult to fit. The weights are validated for a set of 500 clusters consisting of $Au_m(SH)_n$ clusters (m : 13 - 38 and n : 6 - 24). Their energies are compared with the DFT predicted energies as shown in Fig. 5.10(a). The absolute value of the difference between ANN and DFT predicted energies for these clusters are plotted in Fig. 5.10(b). The atomic force components as predicted from ANN and DFT for the training and testing set clusters are compared as shown in Fig. 5.11. Similar to $AgAu$ system, the y component of forces as predicted by ANN and DFT for three different compositions- $Au_{13}(SH)_8$, $Au_{15}(SH)_{13}$ and $Au_{20}(SH)_{12}$ is plotted as shown in Fig. 5.13. It can be seen that the predictions are well correlated and thus the proposed scheme can be utilized for accurate prediction of atomic forces. The ANN weights are extrapolated to study the geometry optimization and dynamics of $Au_{68}(SH)_{32}$. On geometry optimization of the GM and the local minimas predicted for $Au_{68}(SH)_{32}$ by Xu et al.,[183] similar structures are obtained as shown in Fig. 5.12. This reflects that the atomic forces were fitted very well and have captured necessary bonding patterns between Au, S and H. Also, the dataset $Au_{13}(SH)_6$-$Au_{38}(SH)_{24}$ forms a subset for the atomic environments of $Au_{68}(SH)_{32}$.

Since, geometry optimization was achieved accurately, MD simulations are performed further. The MD simulations are run at temperatures - 100 K, 150 K, 200 K and 300 K at a time step of 0.1 *fs* for a total time of 1 *ns*. Running the dynamics at 300 K gave an important insight into structural stability of thiol protected gold nanoclusters. It is observed that thiol group undergoes desorption from the gold surface as shown in Fig. 5.14. This observation is in accordance with the work done by Büttner et al.[208] by using X-ray photoelectron spectroscopy for thiol passivated gold particles. To validate this observation, average bond length fluctuations[184] are plotted for the S and staple - Au bonds as shown in Fig. 5.15. The plot highlights that the S and staple- Au are intact at a very low tem-

perature of 100 K. But as the temperature is increased, the fluctuations increase in the beginning of the simulation and thus leads to a breakage in the bond between S and Au. This is clear from the blue colored plot at 300 K shown in Fig. 5.15. Therefore, in order to maintain the protection of gold nanoclusters, they should be stabilized below 150 K such that thiol group does not desorb from gold surface. Different local minima structures are quenched from the MD simulations using L-BFGS algorithm. Some of the core geometries are shown in Fig. 5.16.

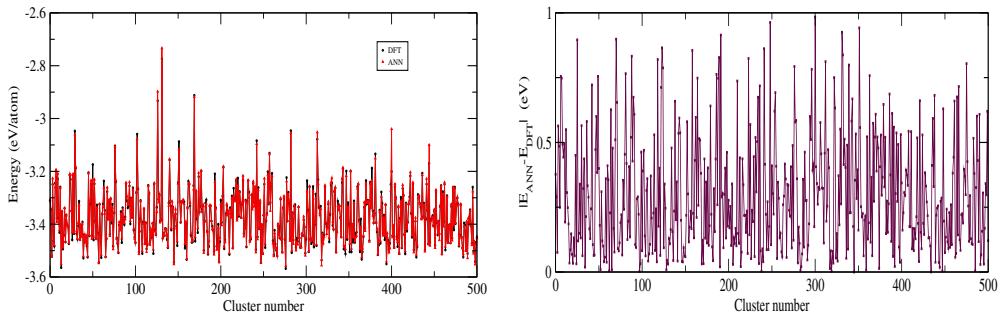

(a) (b)

Figure 5.10. (a) Comparison of DFT and ANN predicted energies for $Au_m(SH)_n$ clusters where m varies from 13 to 38 and n varies from 6 to 24, (b) Plot showing the absolute value of $|E_{ANN} - E_{DFT}|$ for $Au_m(SH)_n$ clusters where m varies from 13 to 38 and n varies from 6 to 24

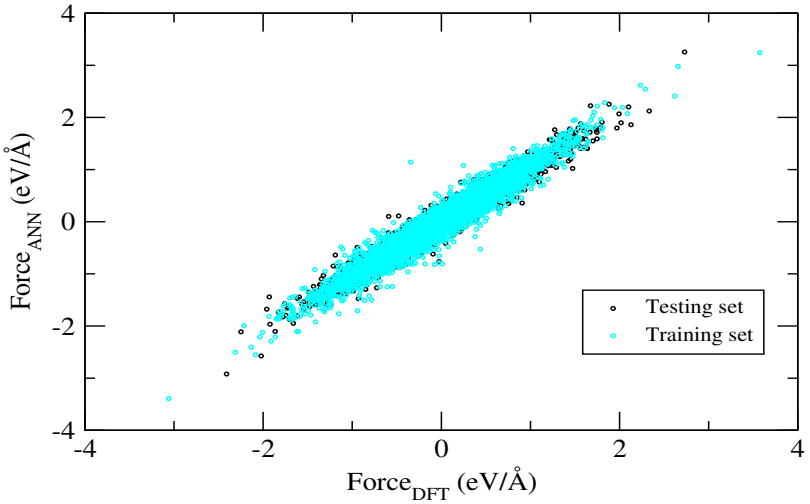

Figure 5.11. Correlation plot of ANN and DFT predicted atomic forces for testing and training set of $Au_m(SH)_n$ clusters where m varies from 13 to 38 and n varies from 6 to 24

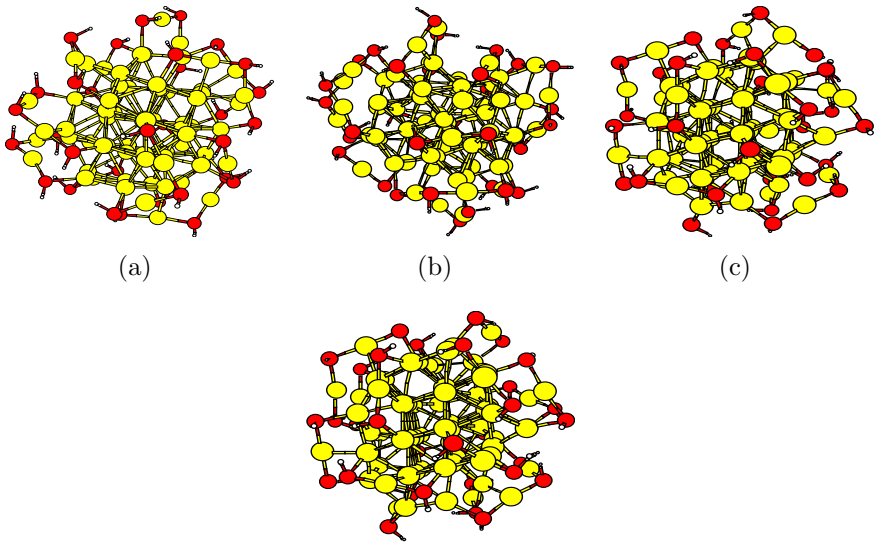

Figure 5.12. Optimized structures of $Au_{68}(SH)_{32}$ similar to that obtained by Xu et al. (a)The GM structure, (b),(c) and (d) are the local minimas.

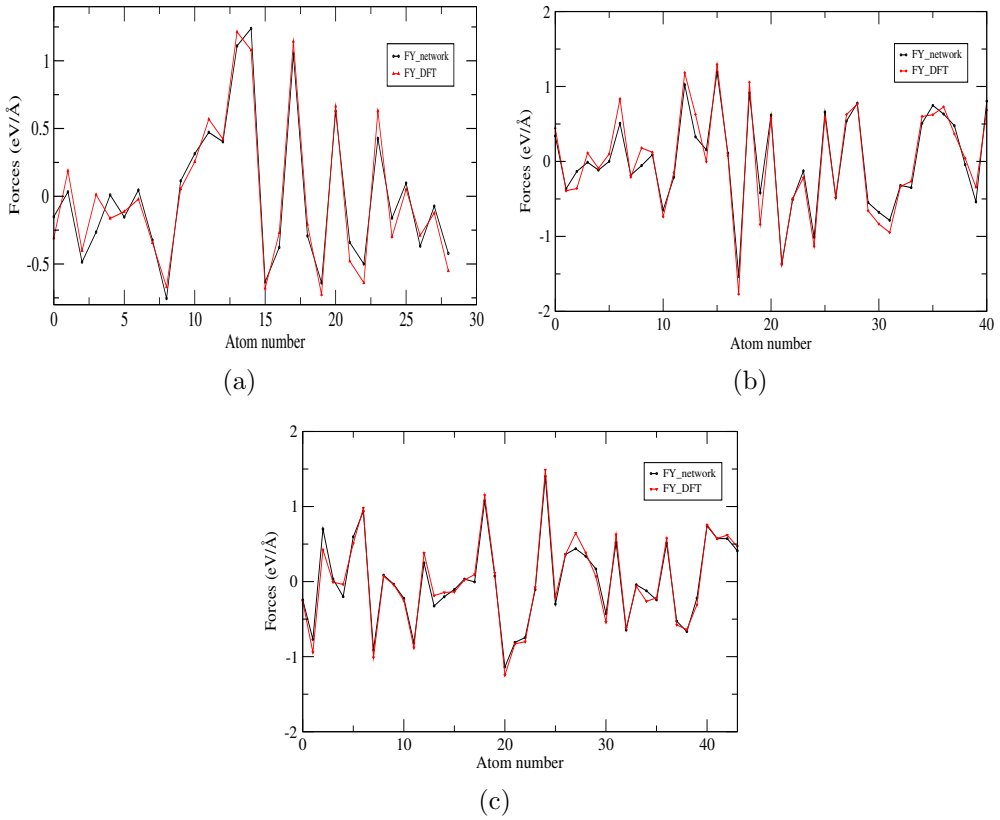

Figure 5.13. Plot of Y component of force for (a) $Au_{13}(SH)_8$, (b) $Au_{15}(SH)_{13}$, (c) $Au_{20}(SH)_{12}$

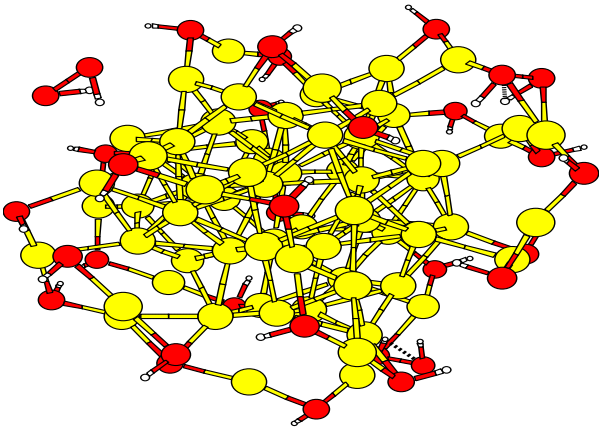

Figure 5.14. Desorption of thiol group from Au in $Au_{68}(SH)_{32}$ at 300 K

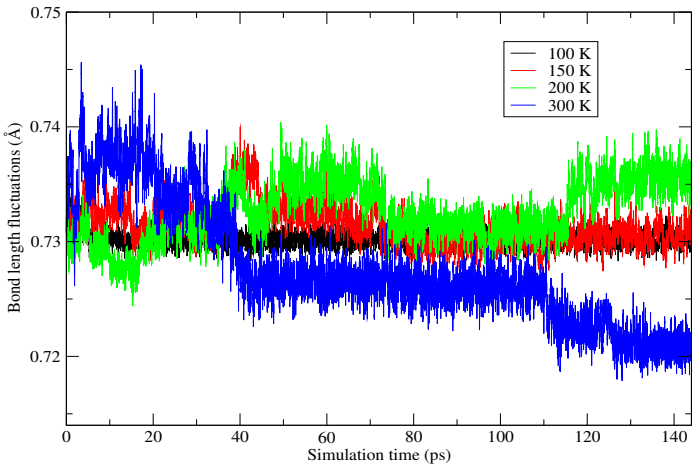

Figure 5.15. Average bond length fluctuations between S and staple-Au during MD simulations at 100 K, 150 K, 200 K and 300 K of $Au_{68}(SH)_{32}$

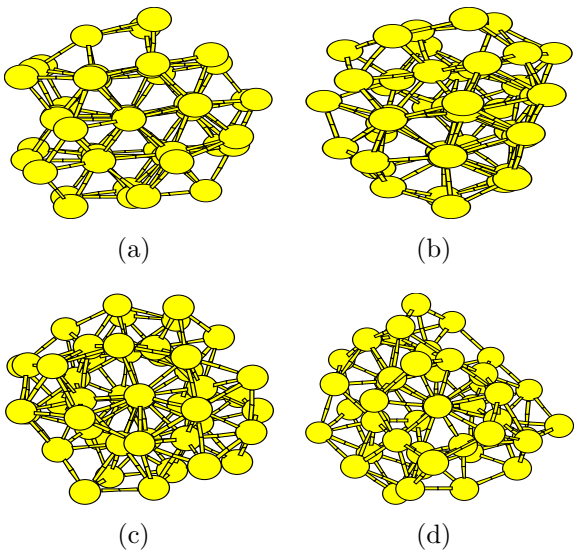

Figure 5.16. The core structures for $Au_{68}(SH)_{32}$

5.3.3 Application of ANN for global optimizations of $AgAu$ nanoalloys and thio-protected Au nanoclusters

After studying the ANN based MD simulations, global optimizations for gold-silver nanoalloys and thio- protected gold nanoclusters are performed. Two clusters for gold-silver nanoalloys having 10% (Ag_5Au_{50}) and 24% ($Ag_{13}Au_{42}$) composition of Ag are selected. For thio- protected gold nanoclusters, Au_{15} cluster protected with three different amounts of thiol units (8, 10 and 13) is chosen. The global optimizations are performed using BH[168] and MD simulations. The quenching of the structures is done with the L-BFGS algorithm.[73]

(i) $Ag_{13}Au_{42}$

The BH is initialized using 10 different structures. Each run is done for 30000 steps and a bunch of 50 minimum energy structures is quenched and saved from each run. A GM structure is obtained as shown in Fig. 5.17. The GM structure contains an 8 atom symmetric core and 47 atom surface. It is in accordance with previous work by Chiriki et al.[202]The 13 Ag atoms are arranged as 5 on the surface and 8 in the core. A total of 435 isomers lying in an energy range of 4 eV from the obtained GM structure are collected. A histogram is plotted to visualize the number of isomers obtained in this energy range as shown in Fig. 5.18. One of the common feature among all the isomers is the presence of 5 Ag atoms on the surface. Though, some high energy clusters contain more than 5 Ag atoms on the surface. Due to an accurate fitting of forces, different geometries of the inner core within close energy difference from the GM is obtained as shown in Fig. 5.19 and Table. 5.1. It shows the highly fluxional nature of gold-silver nanoalloys. Other than core geometries, surface atom arrangements also show a lot of fluctuations as seen in Fig. 5.20.

(ii) Ag_5Au_{50}

For exploring the PES of Ag_5Au_{50}, the MD simulations were ran at

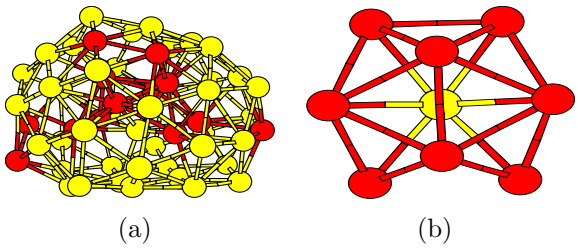

Figure 5.17. (a) The GM structure of $Ag_{13}Au_{42}$, (b) The core structure of the GM of $Ag_{13}Au_{42}$

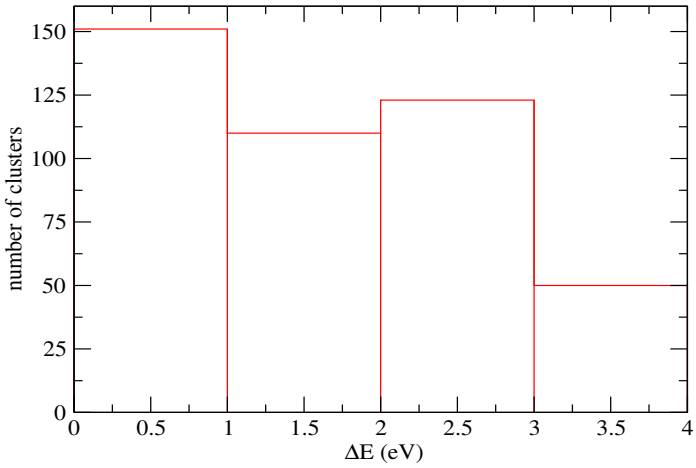

Figure 5.18. A histogram showing the number of isomers found in an energy range of 4 eV from the GM of $Ag_{13}Au_{42}$

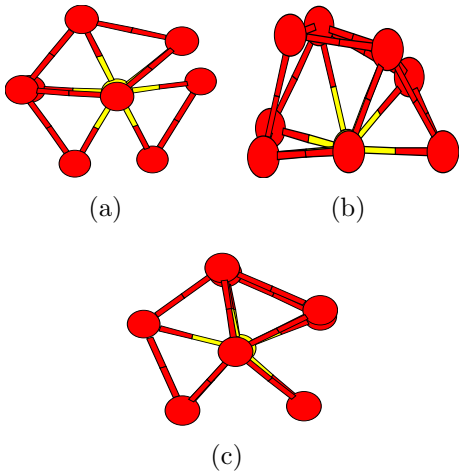

Figure 5.19. The core structures for $Ag_{13}Au_{42}$

300 K and 400 K for a total time of 1 ns at a time step of 2 fs using different initial structures. The structure were quenched after every 20 ps of the simulation. The GM isomer having an amorphous surface was obtained as shown in Fig. 5.21(a). A symmetric core arrangement was observed in the

Table 5.1. Difference between the energies of GM structure and some low lying isomers of $Ag_{13}Au_{42}$

Difference	Fig. 5.19(a)	Fig. 5.19(b)	Fig. 5.19(c)
$\Delta E(E_{GM} - E_{iso})$ (eV)	0.2359	0.3249	0.3743

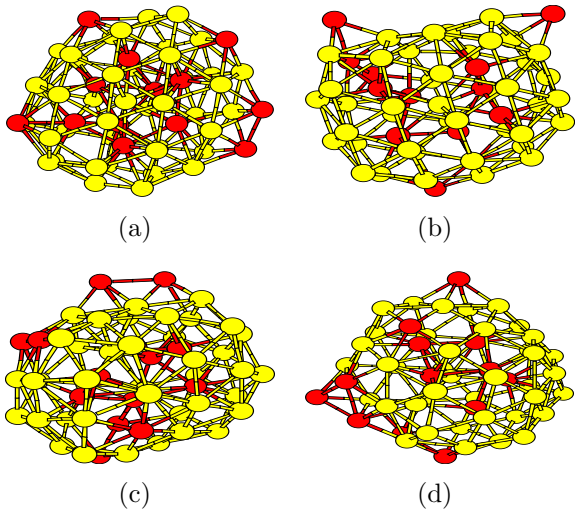

Figure 5.20. Low lying isomers of $Ag_{13}Au_{42}$ ΔE $(E_{GM} - E_{iso})$ (a) 0.483 eV, (b) 1.733 eV, (c) 1.737 eV, (d) 1.79 eV

GM structure as shown in Fig. 5.21(b). Since, Au atoms are in majority, the structure is more towards amorphous. A lot of low lying isomers were obtained having energy difference of 1 eV from the found GM structure. A different core arrangement was discovered in the low lying isomers as shown in Fig. 5.22. The difference between the energy of isomers shown in Fig. 5.22(a) and (b) from the GM is 0.0118 eV and 0.4856 eV, respectively. Since, the energy difference is less than 0.5 eV, it shows that gold doped nanoclusters are fluxional in nature. A lot of isomers were identified with very different arrangement of surface atoms as shown in Fig. 5.23.

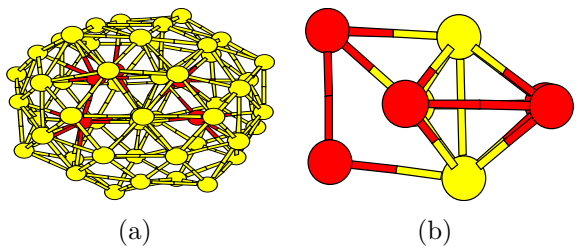

Figure 5.21. (a) The GM structure of Ag_5Au_{50}, (b) The core structure of the GM of Ag_5Au_{50}

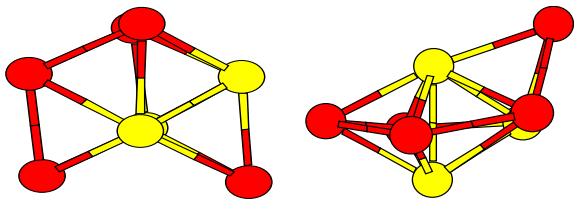

Figure 5.22. The core atom arrangement of Ag_5Au_{50}

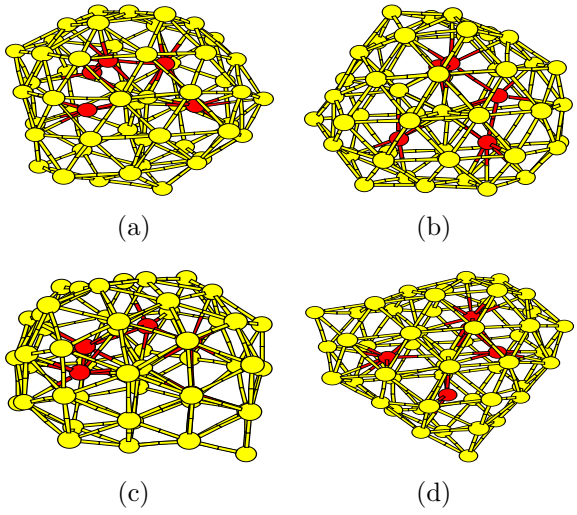

Figure 5.23. Low lying isomers of Ag_5Au_{50} $\Delta E(E_{GM} - E_{iso})$ (a) 0.1212 eV, (b) 0.3407 eV, (c) 0.5259 eV and (d) 1.16 eV

(iii) $Au_{15}(SH)_8$, $Au_{15}(SH)_{10}$ and $Au_{15}(SH)_{13}$

To study the global optimizations, thio- protected Au_{15} cluster was chosen with different concentration of SH group. The MD simulations were ran at 100 K and 150 K for sampling the PES of thio- protected gold clusters. Around 212 structures were sampled for $Au_{15}(SH)_8$ and 208 structures for $Au_{15}(SH)_{10}$ in an energy interval of 0.5 eV from the tentative GM structure obtained from the MD simulations. For $Au_{15}(SH)_{13}$, 220 structures were sampled in an energy interval of 1.0 eV from the tentative GM structure. All the simulations were run at time step of 1 fs and the total time of simulation was 2 ns. The GM structures are shown in Fig. 5.24. It was observed that as the number of units of SH increased from 8 to 10, a more symmetric structure is obtained. But, as the units were increased to 13, there was not much impact on the symmetry of the structure. Isomers having different geometries were obtained for all the three compositions.

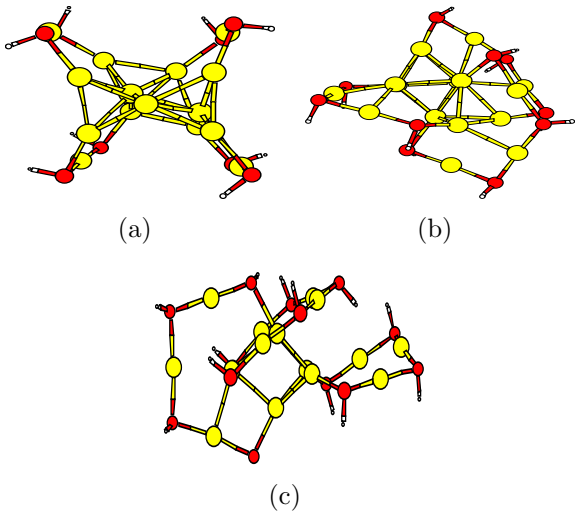

Figure 5.24. GM structures of (a) $Au_{15}(SH)_8$, (b) $Au_{15}(SH)_{10}$, (c) $Au_{15}(SH)_{13}$,

The low lying isomers for $Au_{15}(SH)_8$, $Au_{15}(SH)_{10}$ and $Au_{15}(SH)_{13}$ are shown in Fig. 5.25, 5.26, 5.27, respectively. A conclusion that can be made from the different isomers obtained for silver-gold nanoalloys and thio- protected gol nanoclusters is that gold based Nps exhibit a lot of fluctuations in their structure and thus reactivities can be tuned according to different geometries obtained.

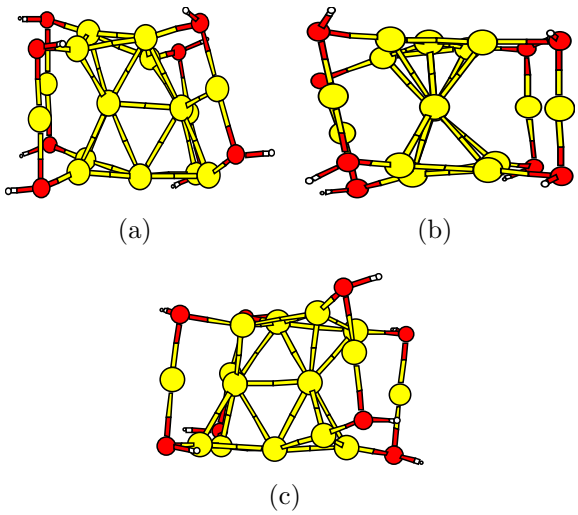

Figure 5.25. Low lying isomers of $Au_{15}(SH)_8$, ΔE ($E_{GM} - E_{iso}$) (a) 0.2389 eV, (b) 0.2737 eV, (c) 0.4178 eV

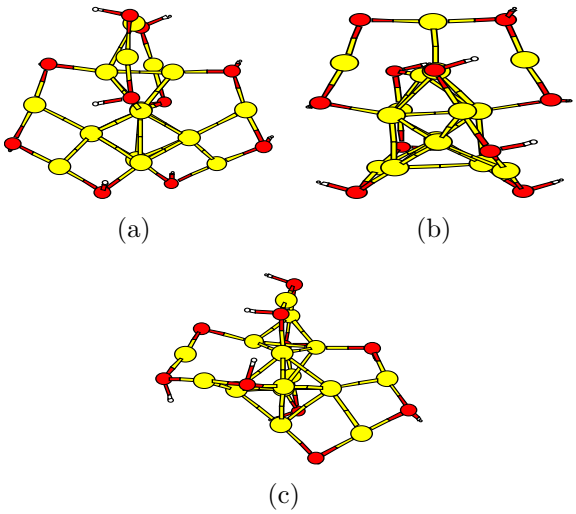

Figure 5.26. Low lying isomers of $Au_{15}(SH)_{10}$, ΔE ($E_{GM} - E_{iso}$) (a) 0.005 eV, (b) 0.095 eV, (c) 0.205 eV

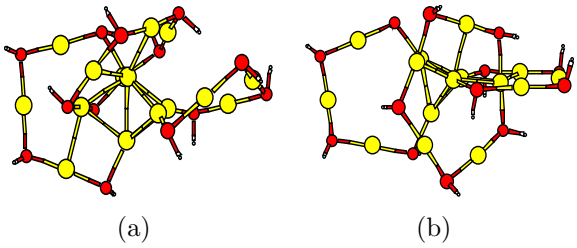

Figure 5.27. Low lying isomers of $Au_{15}(SH)_{13}$, ΔE ($E_{GM} - E_{iso}$) (a) 0.614 eV, (b) 1.329 eV

5.4 Summary

A transferable ANN model for fitting energy and forces for any Np is proposed. The model is termed "transferable" due to the dependence on inter-atomic distances, effective nuclear charges of the chemical species and reduced mass of the bonds involved in a chemical system. By doing a concurrent but decoupled fitting of energy and forces of a MC system using a SANN, an accurate representation of the atomic environments is achieved. Using the same network for any chemical species in the system leads to a tremendous reduction in the computational costs. Since, forces are highly sensitive for an atomic environment, its fitting was a challenge, which was discussed in this chapter. The proposed method was applied to two systems. One consisting of a bimetallic alloy i.e. $(AgAu)_{55}$-$(AgAu)_{147}$ and the other a range of thiol protected gold nanoclusters ($Au_{13}(SH)_6$-

$Au_{38}(SH)_{24}$), $Au_{68}(SH)_{32}$. Due to a precise representation of forces, the weights obtained for the dataset consisting of $Au_{13}(SH)_6$-$Au_{38}(SH)_{24}$ were able to optimize the geometry of $Au_{68}(SH)_{32}$ and run its dynamics. This proves the transferability of the scheme from a small size to a large size system.

Chapter 6

Evolution of gold from subnanometer to nanometer level and different levels of theory

6.1 Introduction

In previous chapters, I fitted the PES of gold nanoclusters up to Au_{147} using different types of descriptors and ANN. In this chapter, the exceptional ability of ANN weights is used to study the structural evolution of gold nanoclusters till a size of $\sim$ 3.3 nm. Relativistic effects in gold makes its behavior different than other metals. Unlike silver and copper, gold does not prefer symmetrical structures as the stable entities. The ANN trained on quantum mechanical data comprising of small to medium sized clusters, gives exceptional results for larger size clusters. It reflects the exceptional pattern recognizing capability of ANN. The PES for "magic" number clusters- 309, 561 and 923 is explored in this chapter. It is observed that these clusters do not prefer symmetric structures in gold. The probability for atoms to move towards surface in gold Nps is very high, leading to presence of more atoms on the surface to stabilize a compact core structure. They prefer a distorted symmetric core with amorphous layers of atoms over it. The amorphous geometries tend to be more stable in comparison to completely symmetric structures. A trend in the evo-

lution of a symmetric core is studied as the size of the Np increases. In the structural evolution, stable symmetric cores (Ih) are found at Au_{160}, Au_{327}, Au_{571}, which can be recognized as new magic numbers. Au_{923} is found to have a stable symmetric core of 147 atoms covered with layers of atoms that are not completely amorphous. This shows the preference of symmetric structures as the size of the Np increases(<3.3nm). A finite temperature probability analysis of Au_{309} is also discussed.

6.2 Computational details

DFT calculations All the DFT calculations are done using VASP[141, 142, 143, 144]. The relativistic effects and the core electrons in gold nanostructures, were taken care of by PAW method. PBE[146, 147] functional and generalized gradient approximation is used to describe the electron correlation. For sampling the Brillouin zone, a Gamma k-point mesh is used. The gradient convergence and the threshold energy is set at 10^{-4} and 250 eV, respectively.

MD simulations The simulations were run using in-house developed code in FORTRAN. Verlet algorithm was used to integrate Newton's equations. The thermostat used for maintaining constant temperature was Anderson thermostat. The MD simulations were run at temperatures- 250 K, 300 K and 400 K. A time step of $3fs$ was used and the run time of each simulation was 1 ns.

MCBH search In order to explore the PES around the obtained local minimas, MCBH search[169, 170, 171] was employed. In this search, the number of bins are fixed as 12, with a difference of energy as 1.5 eV between the minimum and maximum energy levels. The initial temperature was set as 0.55 for all the search runs. A total of 10 runs were done for a particular size of clusters and each run were performed for a maximum steps of 5×10^4. Top 50 isomers were collected in each run.

All the structure optimizations were done using L-BFGS algorithm[73]. The number of iterations were kept 500 till a gradient convergence of 10^{-5}

was achieved.

6.2.1 Fitting of energy and forces using ANN

To check the extrapolation ability and transferability of the NN weights, I applied the weights obtained in chapter 3 (set-I weights) for the prediction of energy and forces of very large size clusters(>300). The average RMS error in forces are plotted for a few large size clusters(Au_{309} and Au_{561}), as shown in Fig. 6.1(a). The RMS error of all the clusters lie below 84.74 meV/Å/atom and therefore for larger size Nps, the atomic forces patterns are very well captured by the data set consisting of a maximum size of 100 atoms. On the other hand, for very large size clusters, the energy pattern were same but the magnitude of the predicted energy differed from the DFT values. As shown in Fig. 6.1(b), the pattern followed by the energy for a few Au_{309} clusters using DFT and set-I weights are similar, but set-I weights are unable to differentiate between the stability of symmetric structure with the other low lying amorphous structures.

In order to remove the discrepancy in the magnitudes of the predicted energies, the energy of the same data set is fitted without fitting the forces. In the KF, instead of 3N+1 dimensional error vector, only a single component i.e. energy is fitted. Such a fitting helps in providing accurate energies for structures varying highly in symmetry, but lying in a same energy well. The RMS error for energy on a test set of 1300 clusters was 4.6meV/atom [set-II]. The energy of Au_{309} clusters using set-II weights is plotted as shown in Fig. 6.1(b). The predictions were completely inline with DFT and therefore, accurate energy predictions are achieved for very large size clusters. As shown in Table 6.1, the relative energy difference between the lowest minimum(LM) structure of Au_{309} (and Au_{561})and the other isomers of Au_{309} (and Au_{561}) from DFT and ANN are in good agreement. It is evident from the table that the energies are predicted very well by ANN, and the weights which are fitted for predictions of energy only can be applied to any size of clusters. Overall for very large size clusters,

two sets of weights are used – (1) For energy predictions [set-II] and (2) For forces predictions [set-I].

Table 6.1. The relative energy difference between LM and other isomers from DFT and ANN(set-II weights) (in eV) for Au_{309}

	Iso-1	Iso-2	Iso-3	Iso-4	Ih
DFT	0.307	5.321	5.357	7.313	8.274
ANN	0.107	4.977	5.543	6.978	7.660

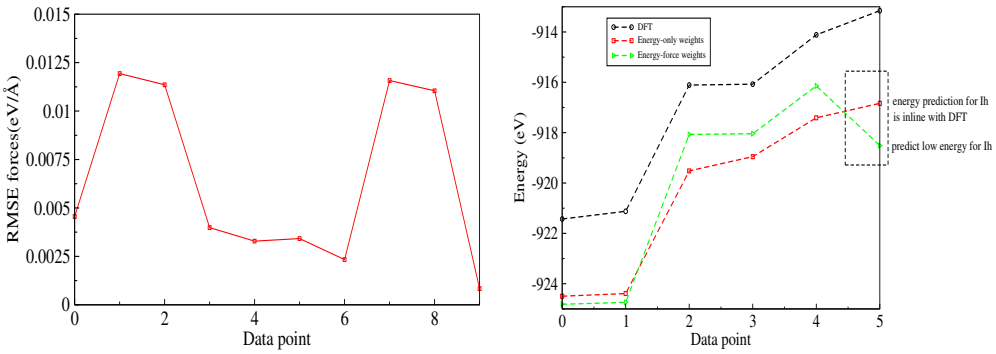

(a) (b)

Figure 6.1. (a) Average RMS error in forces for a data set containing Au_{309} and Au_{561}. The RMS error of all the clusters are below the average RMS error for the testing data set consisting maximum size of 100 atoms; (b) The comparison between the energy predictions by DFT, energy-force (set-I) weights and energy only (set-II) weights. It shows the discrepancy in the energy predictions using energy-force weights.

Table 6.2. The relative energy difference between LM and other isomers from DFT and ANN(set-II weights) (in eV) for Au_{561}

	Iso-1	Iso-2	Ih
DFT	2.005	0.2063	10.455
ANN	2.758	0.0073	11.397

6.3 Results and discussion

6.3.1 PES exploration using SAS tool

There are various methods by which the PES of a metallic cluster can be explored. The widely used algorithms are genetic algorithm[177, 178], BH method[168], Monte Carlo simulations, MD simulations. These algorithms helps in a global search of lowest energy structures efficiently. Since gold Nps have a wide variety of structures within narrow energy range, a new technique is developed for an efficient search within a narrow time range. The main target is to narrow down the search of LM structures on a very high dimensional PES. The gold Nps prefers amorphous and cage type structures with few exceptions like Au_{20}, which has a pyramidal structure[110, 116]. The methodology of SAS tool is discussed in Chapter 2.

6.3.2 Magic number clusters- Au_{309}, Au_{561} and Au_{923}

Using SAS tool, 10 different initial structures were constructed for Au_{309}. Few structures with a symmetric core and a spherical shell covering it were also generated. All the constructed structures along with the pure Ih structure of Au_{309} were optimized. The results obtained directs the indication towards gold's structural preference i.e. amorphous. The surface atoms in Ih geometry of Au_{309}(Fig. 6.2(a)) are 162, which, however, is not energetically preferred by gold. The amorphous structures obtained from preliminary optimizations contained 180 to 182 atoms on the surface. The inner core atoms ranged from 84 to 86, 33 to 38, and 5 to 7 in the third layer, second layer and inner core respectively. Most of these structures had energy lower than Ih, whereas a few were higher than Ih, giving a tough competition for mutual existence. The relative energy difference between amorphous structures and Ih structure are validated from DFT. DFT results were in agreement with the ANN predicted results. To further investigate the possible LM structure, MD simulations were performed. A

lot of LM structures were collected by quenching the MD trajectories. The LM structures along with randomly designed new structures were used as initial structures in MCBH search to obtain more minimas. A family of 212 clusters in an energy range of 0.82 eV containing 177 surface atoms, 86 atoms in third layer, 37 atoms in second layer and 9 atoms in the inner core were obtained. Few of the amorphous isomers of Au_{309} is shown in Fig. 6.3. The LM obtained has a proper core-shell structure as shown in Fig 6.4(a). The arrangement of core atoms reflects some symmetry but with a little distortion as shown in Fig 6.4(c). The diameter of the LM is 2.19 nm with bond lengths among surface atoms ranging from 2.64$\mathring{A}$ to 2.90$\mathring{A}$. The structure of inner core of the LM can be described as a bicapped pentagonal bipyramidal structure as shown in Fig 6.5(b). A similarity in the arrangement of core atoms of LM-Au_{309} is drawn with the core atom structure of GM of Au_{147}[134, 135] in Fig 6.5. The inner core of Au_{147} has 7 atoms arranged as capped square bipyramidal whereas, in Au_{309}, two more atoms i.e. 9 atom forms the core.

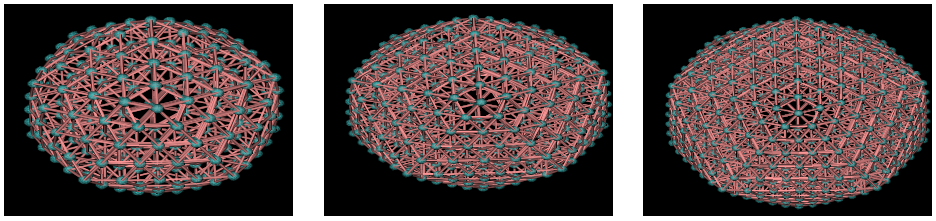

(a) (b) (c)

Figure 6.2. The Ih structure of a) Au_{309}, (b) Au_{561} and, (c) Au_{923}

After successfully applying SAS tool for LM search of Au_{309}, it was used for exploring the PES of Au_{561}. For initial structure construction for Au_{561}, a similar approach to Au_{309} was applied. The Ih structure (Fig. 6.2(b)) of Au_{561} consists of 252 atoms on the surface having bond lengths greater than 2.9 Å. On optimizing the structures made from SAS tool, the surface atoms in Au_{561} varied from 265 to 277 in different structures. MD simulation and MCBH search was applied further to collect more population.

In the LM structure, the surface atoms increased from 252 to 275

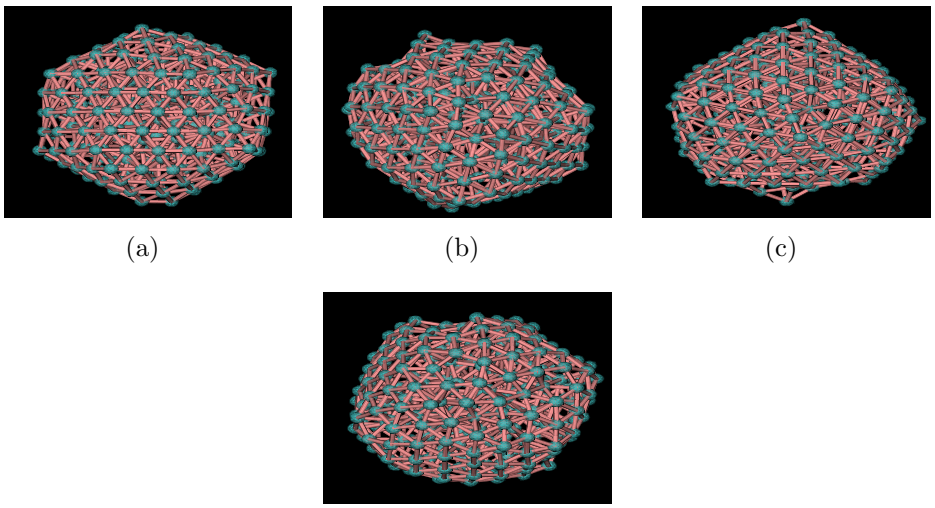

(a) (b) (c)

(d)

Figure 6.3. Isomers of Au_{309} (a) Iso-1, (b) Iso-2, (c) Iso-3, (d) Iso-4

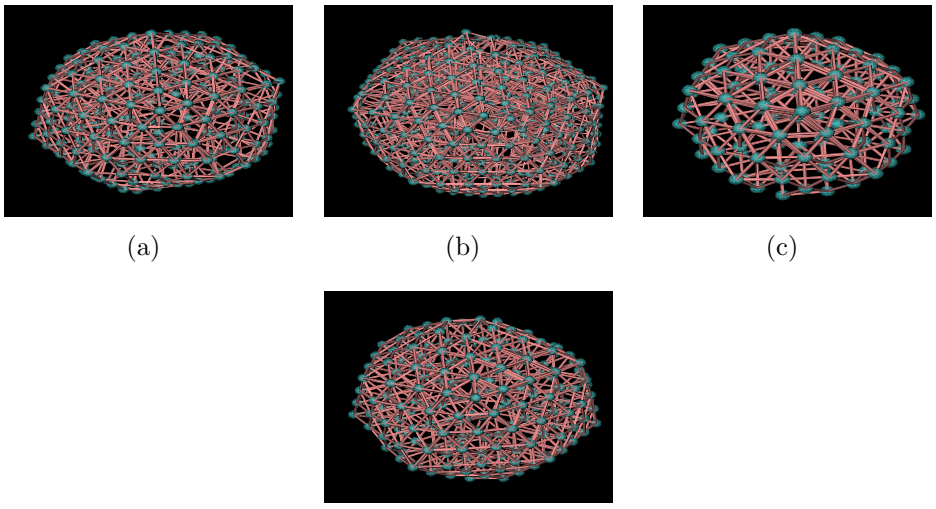

(a) (b) (c)

(d)

Figure 6.4. Core-Shell structure of LM obtained for(a) Au_{309}, (b) Au_{561}; The geometry of core of LM structure of (c) Au_{309}, (d) Au_{561}

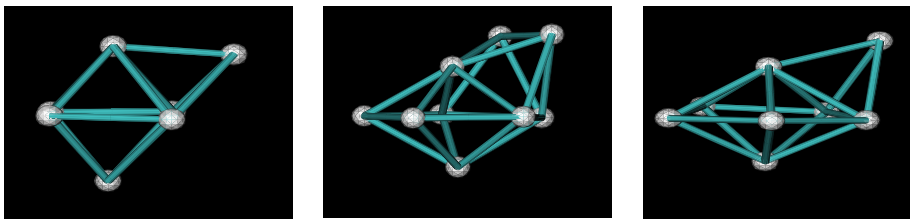

(a) (b) (c)

Figure 6.5. The inner core structure of a) Au_{147}, (b) LM-Au_{309}, (c) LM-Au_{561}

and the innermost core atoms decreased from 13 to 8. It clearly reflects the preference of amorphous structure with more surface atoms for gold

Nps. The LM structure has a diameter of 2.75 nm with bond lengths of surface atoms ranging from 2.62$\mathring{A}$ to 2.95$\mathring{A}$. The inner core structure possess a capped-pentagonal bipyramidal shape (Fig. 6.5(c)) whose pattern is similar to the arrangement of core atoms of LM of Au_{147}(Fig. 6.5(a)) and Au_{309}(Fig. 6.5(b)).

Au_{923} is a $\sim$ 3.3 nm sized particle, so calculating its energy and forces using DFT is highly computationally expensive. Since, DFT validated the ANN predictions for Au_{309} and Au_{561}, the ANN weights were used for exploring the stability of Ih structure for Au_{923}. The Ih-Au_{923}(Fig. 6.2(c)) consists of 362 surface atoms over a Ih-561 core. To explore the energetic stability of amorphous structures at $\sim$ 3.3 nm, 8 initial structures were constructed using SAS tool and further optimized. The search was biased by constructing 5 different structures having Ih-13, Ih-55, Ih-147, Ih-309 and Ih-561 as cores respectively, with required number of atoms and spherical layers over each to complete Au_{923} structure. On optimizations, structures having more surface atoms ranging from 370 to 385 were obtained. The MD simulations were ran using 3 different structures at 300K. On quenching the structures obtained from the simulations, the LM structure obtained (Fig. 6.6) was found to be $\sim$10 eV lower in energy than the Ih-Au_{923}. The interesting fact about the LM obtained is that an Ih-147 atoms core is maintained with varying atoms in the top three layers leading to a amorphous surface with 388 atoms. This reflects the fact that AuNps start evolving to a completely symmetric structure at $\sim$3.3 nm size. From MCBH search od Au_{923}, a family of structures lying higher in energy than the LM structure were obtained.

6.3.3 Adsorption energy of CO and O_2 on LM surface

On obtaining the LM structures of 309, 561 and 923, the catalytic activities of these clusters for CO and O_2 adsorption on their surface are probed. Xu et al[209] have recently designed geometry-adsorption activity descriptors

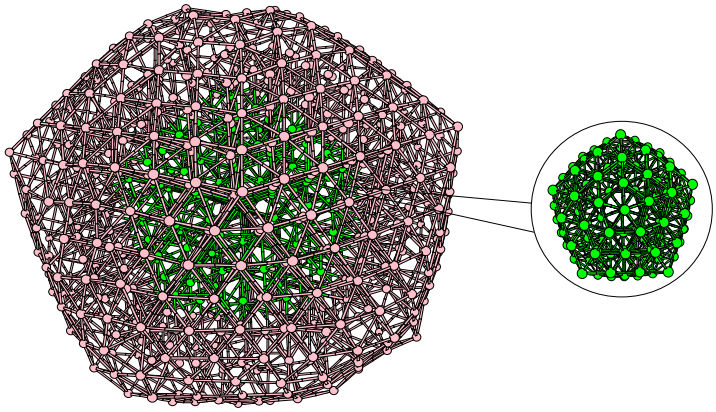

Figure 6.6. The LM of Au_{923} with a distorted surface and a Ih Au_{147}

to study the binding strength of CO and O_2 with gold clusters. In this work, those descriptors are applied to calculate the adsorption energies of Au_{309}-Ih, Au_{561}-Ih, Au_{923}-Ih, Au_{309}-LM , Au_{561}-LM and Au_{923}-LM using Eqs. 6.1 and 6.2. The $\overline{CN}$ is the generalized coordination number of an atom h, $\overline{CN}(h) = \sum_{k=1}^{atoms}(CN(k)N_k)/(CN)_{max}$. The $\overline{CN}$ is calculated as sum over all the neighbors coordination number. The neighbors coordination number$(CN(k))$ is weighted with the number of neighbors (N_k). CN_{max} is the maximum coordination number of Au in bulk structure i.e. 12.

$$E_{\text{ad}}(CO) = 0.14 \times \overline{CN} - 1.38 \tag{6.1}$$

$$E_{\text{ad}}(O_2) = 0.15 \times \overline{CN} - 0.93 \tag{6.2}$$

A plot of number of surface atoms having different adsorption energies for Ih-Au_{309} and LM-Au_{309} is shown in Fig. 6.7. On the X-axis, the adsorption energies vary from minimum to maximum interval. The total number of atoms which are activity centers in the cluster are binned with respect to the binding strength. It is observed that amorphous LM structure has more atoms with high binding strength for CO and O_2 as compared to the Ih structure. The atoms on LM surface have different binding energies due to amorphous arrangement. On the other hand, Ih structure has a symmetrical layout due to which many atoms have similar catalytic activity and thus similar binding strength. The sites having very low binding energy and a high binding strength for CO and O_2 is color marked in Fig. 6.8(a)

and 6.8(b). These sites have lower energy than the sites in Ih structure. The red colored atoms have the highest binding strength (< -0.9 eV for CO, < -0.5 eV for O_2), the blue (-0.8 eV to -0.9 eV for CO, -0.4 eV to -0.5 eV for O_2) and green colored atoms (-0.7 eV to -0.8 eV for CO, -0.3 eV to -0.4 eV for O_2) have slightly lower binding strength. Therefore, due to presence of more active sites, Au Nps having an amorphous surface structure have high catalytic activities.

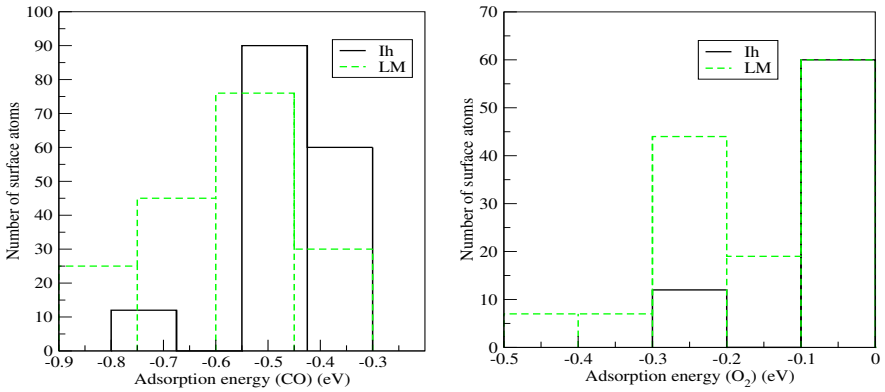

(a) (b)

Figure 6.7. The number of surface atoms binned with respect to adsorption energies of (a) CO and (b) O_2 on Ih-Au_{309} and LM-Au_{309}

Similarly, the adsorption energies of surface atoms of LM and Ih structure of Au_{561} are calculated. The adsorption energy plots (Fig. 6.10) show a contrast between the binding strengths and the number of atoms available for catalytic activities in Ih and LM structure. In the LM structure, the active sites having a high binding strength as compared to Ih structure is higher. As seen from Fig. 6.8(c) and 6.8(d), the top and edge sites have high binding strength as compared to the other sites on the surface. The adsorption energies plots for Ih and LM structures of Au_{923} follows a similar trend as Au_{309} and Au_{561}, as shown in Fig. 6.11. The binding sites have increased in the LM structure and therefore AuNps are catalytically active at $\sim$3.3 nm size. The active sites having high binding strength for CO and O_2 are highlighted in Fig. 6.8(e) and 6.8(f). This study shows that the number of surface atoms along with the structural arrangement has an impact on the catalytic activities of AuNps. A compact arrangement

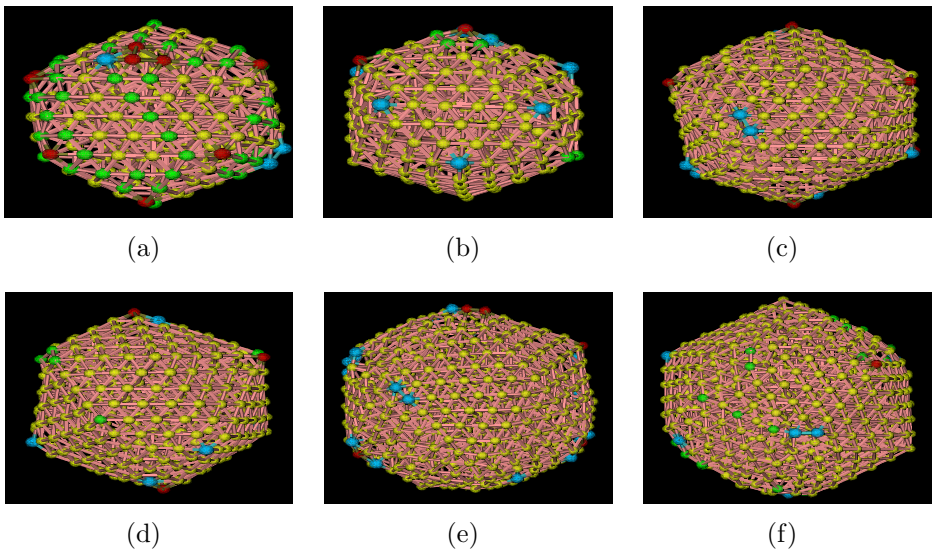

Figure 6.8. The active centres for CO and O_2 adsorption marked for the LM of (a) Au_{309}-CO, (b) Au_{309}-O_2, (c) Au_{561}-CO, (d) Au_{561}-O_2, (e) Au_{923}-CO, (f) Au_{923}-O_2; Red colored atoms have lowest binding energy (< -0.9 eV for CO, < -0.5 eV for O_2), blue colored atoms have binding energy (-0.8 eV to -0.9 eV for CO, -0.4 eV to -0.5 eV for O_2) and green colored atoms have binding energy (-0.7 eV to -0.8 eV for CO, -0.3 eV to -0.4 eV for O_2)

of atoms in Ih structure has lower binding strength when compared to an amorphous arrangement of atoms. In order to check the impact of size of core on the catalytic activities, different structures of Au_{309} are chosen and the adsorption energies for CO and O_2 are calculated. The adsorption energies did not have any impact due to the change in size of core. Although, the active sites decreased due to decrease in the number of surface atoms and increase in number of core atoms in few clusters, as shown in Fig. 6.9. The comparison is shown for five structures having core sizes of 8, 9 (LM), 10 and 13 atoms. For 13 atom core, an amorphous structure and the Ih structure was considered. An anomaly is encountered, when the number of core atoms are 13 for one of the amorphous isomer of Au_{309}. This can be explained by the absence of symmetry in the core atoms. Due to increase in the amorphous content in the cluster, the number of surface atoms increases.

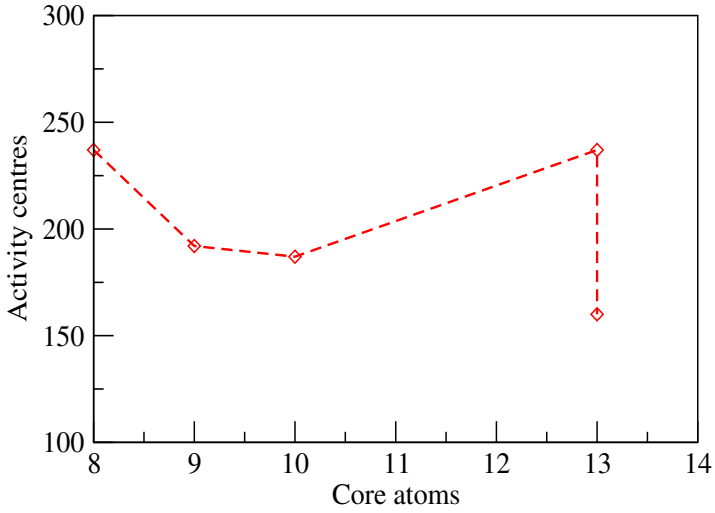

Figure 6.9. The number of active centers for CO adsorption on different clusters of Au_{309} with respect to the core atoms

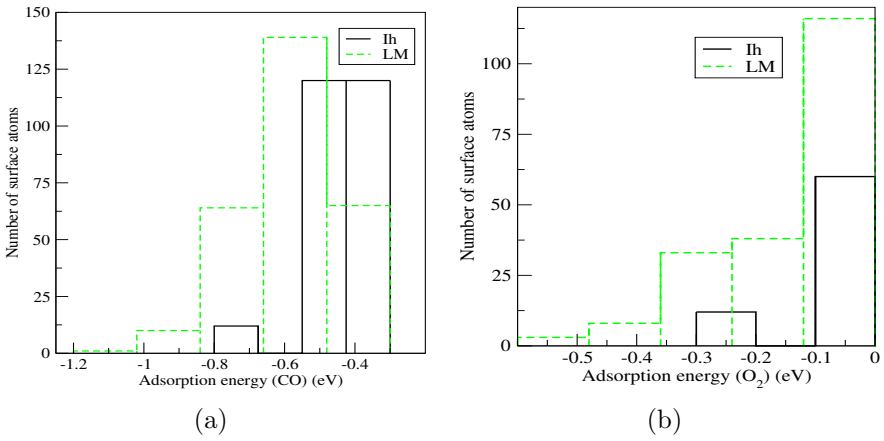

Figure 6.10. The number of surface atoms binned with respect to adsorption energies of (a) CO and (b) O_2 on Ih-Au_{561} and LM-Au_{561}

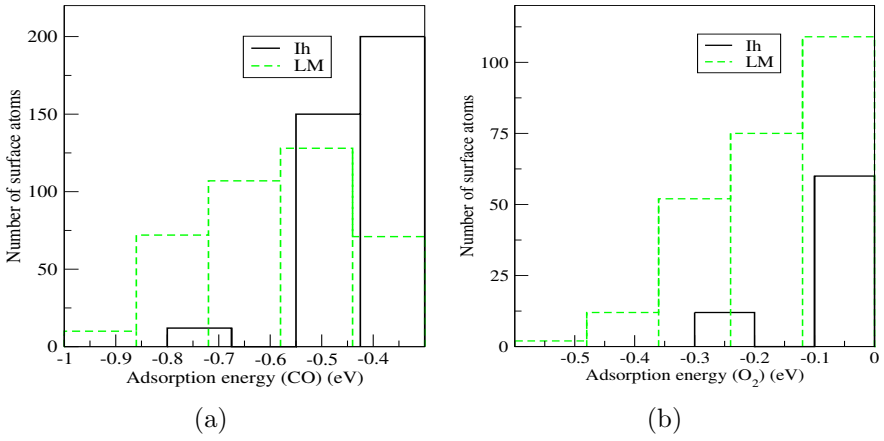

Figure 6.11. The number of surface atoms binned with respect to adsorption energies of (a) CO and (b) O_2 on Ih-Au_{923} and LM-Au_{923}

Table 6.3. The relative energy difference between LM and Ih and Dh structures from DFT and ANN(set-II weights) (in eV) for Au_{75}

ΔE	Ih	Dh
DFT	1.858	1.200
ANN	2.376	0.085

6.3.4 Evolution of a magic core in Au_{160}, Au_{327}, Au_{571}

With the understanding developed till now about the "magic" number clusters, it is confirmed that they tend to differ from having a compact symmetric structure. A recent work by Pande et al[130] showed the presence of Au_{13}(Ih) as a stable core in Au_{60}. This inspired me to look further for the clusters which can have a stable symmetric core. The approach of taking a symmetric core and encapsulating it by one spherical layer was followed. Since, more surface atoms are preferred by gold clusters, the number of surface atoms were selected accordingly. The structures are then optimized to get a LM structure. On optimization, if the symmetric structure persists then MD simulations were carried out to observe the thermodynamic stability of the structure obtained. Further, MD trajectories were quenched and stable structures were collected. The search was continued if the Ih symmetry was not disturbed in MD simulations by using MCBH search. Dh and Oh symmetric cores were not considered, as for gold clusters Ih has been found the most stable among Ih, Dh and Oh. In order to verify that ANN potential is not biased towards Ih geometry, a test case of the Lennard Jones(LJ) Au_{75} cluster was taken. The ground state of LJ-Au_{75} is fcc like (Dh) whereas the second lowest structure is Ih. The MCBH search of Au_{75}-Ih gave an isomer which is much lower in energy than the Dh and the Ih structure. The order of stability follows : LM(distorted symmetry) $>$ Dh $>$ Ih. All the structures are shown in Fig. 6.12. The energy order was confirmed with DFT and it was in agreement with ANN as shown in Table 6.3. This shows that ANN potential is not biased towards symmetric structures. The search was began with clusters around 147 atoms. The numbers chosen were Au_{150}, Au_{152}, Au_{154}, Au_{155}, Au_{156}, Au_{157}, Au_{158},

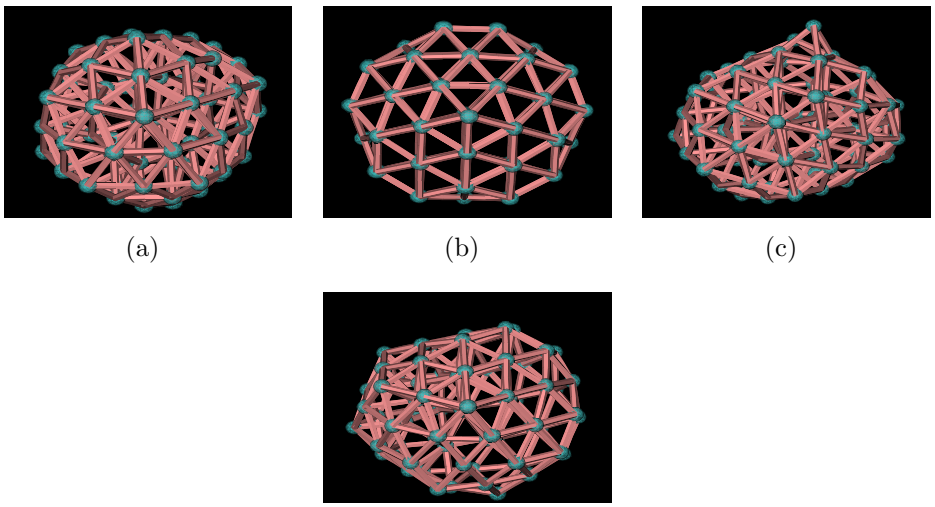

(a) (b) (c)

(d)

Figure 6.12. Au_{75} (a) Ih, (b) Dh, (c) LM obtained (view 1), (d) LM obtained (view 2)

Au_{159}, Au_{160}, Au_{166}, Au_{168}. The aim is to find the minimum number of atomic cluster configuration at which 13 atoms can form a stable core. Initially, alternative numbers are considered in order to get an insight. If 13 atoms are obtained in the core in a particular configuration, then a new configuration with less than one atom was checked. For example, case I- If I get 13 atoms in Au_{155}, then I check for the symmetric core in Au_{154} and case II- If I do not get 13 atoms inside the core, like in Au_{152}, I drop Au_{151} for the study. The 55 atom-Ih structure was put inside a sphere with 95, 97, 99, 100, 105, 111 and 113 atoms, respectively. The structures were optimized and after a series of simulations, Au_{160} was obtained with a stable 12 atom $(13-1)$ symmetric core(Fig. 6.14). The central core atom in the Mackay Ih of 13 atom metallic cluster moved to the outermost surface of Au_{160}. The symmetric core search was continued around 309 atoms. The numbers selected were Au_{308}, Au_{315}, Au_{318}, Au_{320}, Au_{321}, Au_{326}, Au_{327}, Au_{330}. After the simulations-optimization cycle, Au_{327} was obtained with a stable 54 atom $(55-1)$ symmetric core(Fig. 6.14). For search around 561 atoms, Au_{569}, Au_{570}, Au_{571}, Au_{575}, Au_{579}, Au_{581}, Au_{583} were chosen. The trend of having a symmetric core without one central atom continued with Au_{571}, which has a stable 146 atom $(147-1)$ symmetric core(Fig. 6.14). The observations made with this study is that two layers are required to

stabilize a symmetric core in gold Nps. Also, it was observed that the structures of Au_{160}, Au_{327} and Au_{571} containing the central core atom were energetically competitive with the structures without the central core atom. An energy difference of 0.5 eV to 1 eV was obtained between the two types of structures. It can be concluded that there is probably a symmetric core evolution starting from Au_{160} and continuing up to Au_{327} and Au_{571}. The surface of gold Nps is highly fluxional and therefore maintaining a compact symmetric shape is not possible. The numbers 147, 309 and 561 are unable to have a stable symmetric core because there are not enough atoms on the surface to protect the symmetry of the core. As soon as the number of atoms are increased in a structure i.e. in 160, 327 and 571, the inner core symmetry is maintained. With all the data available for different size of gold Nps, the surface atoms ratio with respect to the total atoms in a Np as shown in Fig. 6.13. A logarithmic dependence exists between the surface atoms ratio and total number of atoms. From Au_{147} to Au_{923}, the number of surface atoms decrease from 71% to 42%. Therefore, a decrease in the catalytic activities are observed with increase in the Np size.

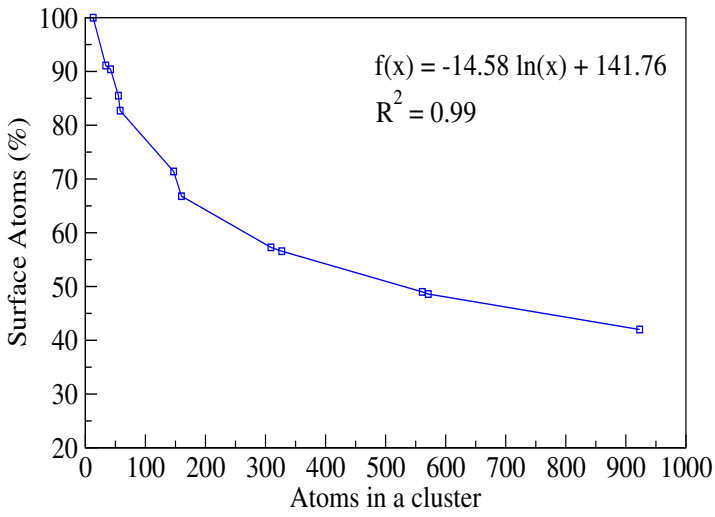

Figure 6.13. The plot of surface atoms ratio against the total number of atoms in a cluster. A logarithmic trend line is fitted to the data with R^2 and the equation in the inset of the plot.

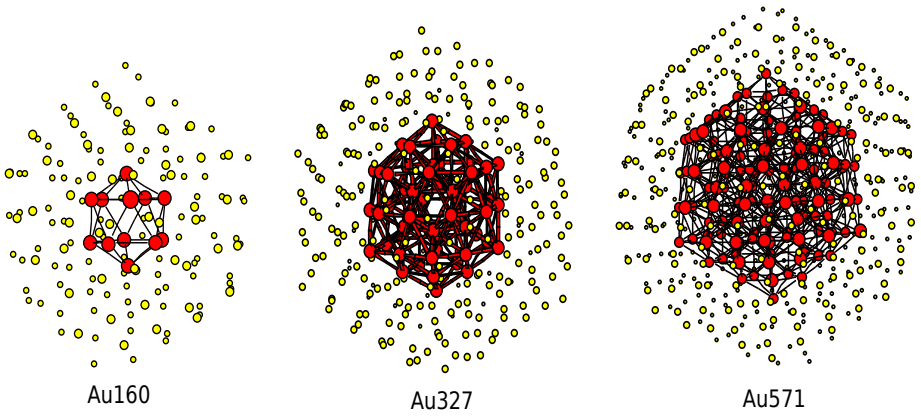

Figure 6.14. The symmetric core evolution in Au_{160}, Au_{327}, Au_{571}

6.4 Variation in structural preference of gold nanoclusters: Different levels of theory

In earlier studies, it have been shown that larger size gold nanocluster prefers Ih, Dh and fcc(Oh) structures. Koga et al[210] studied gold Nps in the size range of 3-14 nm using high resolution electron microscopy. In their study, a coexistence of Ih and Dh structures is observed below 5 nm. It is expected that for Au_{561} ($\sim$ 2.7nm) and Au_{923} ($\sim$ 3.3nm), the population should consists of a considerable amount of Ih and Dh structures. In another study by Foster et al,[211] the energy difference between Dh and fcc of Au_{561} supported on silicon nitride was found to be very small. The Dh and fcc structures were found in abundance in the generated population. Bao et al[212] performed theoretical study of gold clusters (up to 318 atoms) using RGL potential. They have also found very small energy difference between Dh and fcc structures. Wells et al[213] have shown the metastability of the symmetric structures. They have shown that fcc(Oh) and Dh structures are the most abundant in the generated population. All these studies show that symmetric structures- Dh and fcc(Oh) are experimentally preferred geometries. In my study, structures having an amorphous surface and a symmetric core has been found. As the size of the nanoclusters increases to $\sim$3.3 nm, the symmetric core also evolves with a amorphous layer of atoms

over it. These structures are found to be lower in energy (from ANN and DFT) when compared to Ih, Dh and Oh structures.

The DFT calculations are performed at 0 K and thus the stability at a finite temperature is not considered. Since ANN potential mimics DFT, it also gives the relative energy order similar to DFT. In order to check the energy difference between the structures obtained in this study with the symmetric structures, Ih, Dh and Oh structures are constructed using atomic simulation environment[214, 215] which is a python based program. By using ANN potential the Ih, Dh and Oh structures were not found in the population generated by MD simulations and MCBH search. One of the reason for this can be the huge difference in the energy of the amorphous structures and the compact symmetric structures as shown in Table 6.4. The Au_{309}-LM is found to be $\sim$ 8.274 eV (DFT) and $\sim$ 7.660 eV (ANN) lower in energy than Ih structure, $\sim$ 9.498 eV (DFT) and $\sim$ 12.961 eV (ANN) lower in energy than Dh structure and 12.841 eV (DFT) and $\sim$ 17.383 eV (ANN) lower in energy than Oh structure. The Au_{561}-LM is found to be $\sim$ 10.455 eV (DFT) lower in energy than Ih structure, $\sim$ 11.950 eV (DFT) lower in energy than Dh structure and $\sim$ 14.477 eV (DFT) lower in energy than Oh structure. For Au_{561}, the magnitude of the ANN predicted energies is far from the DFT predicted energies, but the relative ordering of the energy is followed by ANN. From DFT and ANN, the energy ordering between symmetric structures is Ih>Dh>Oh, which is according to the gold structural preferences.[120, 131] Since, the LM has a very low energy as compared to Ih, Dh and Oh structures they were not spotted in the MD trajectories and MCBH search. Also, the constructed structures of Ih, Dh and Oh geometry may not be the same structures found in the works of Koga et al,[210] Bao et al[212] and Foster et al.[211]

The energy of a molecule depends upon the type of functional used in DFT. For small gold clusters, Tao-Perdew-Staroverov-Scuseria (TPSS) has been shown to give more accurate results.[216, 217] A comparative study between PBE and TPSS functional calculations for gold nanoclusters was done by Li et al.[120] They showed that the magnitude of energies predicted

Table 6.4. The relative energy difference of Ih, Dh and Oh structures with the LM of Au_{309} and Au_{561} from DFT (in eV)

	Ih	Dh	Oh
Au_{309}	8.274	9.498	12.841
Au_{561}	10.455	11.950	14.477

by TPSS functional is higher than PBE functional, but the relative energies between the structures were same for both the cases.

In order to explain the discrepancy between the experimentally preferred and theoretically predicted structures, a finite temperature probability analysis for Ih, Dh, Oh(fcc) and LM structures of Au_{309} was performed. As discussed by Z. H. Li,[218] the LM structure for a system may not be the most probable and the preferred isomer at a particular temperature. The stability of a cluster at 0 K depends only on the potential energy (PE). At finite temperature, it is governed by other factors like translational, electronic, rotational and vibrational states. The molecular partition function estimates the partitioning of probabilities among different states. The translational partition function is dependent on mass and volume of the cubic box. As the box length and the mass is same for all the Au_{309} isomers, translational partition function is not considered. The electronic partition function is considered to be equal for all the isomers and is therefore removed from the calculations. Thus, the probability of different isomers dependent upon rotational (q_{rot}) and vibrational (q_{vib}) partition functions at 300K, 500K, 800K and 1100K is calculated. The probabilities are calculated only for the four isomers of Au_{309}. The probability may vary if more isomers are taken in the analysis, but the relative values are expected to be same.

The rotational partition function (q_{rot}) is approximated by rigid rotor approximation. For an isomer i, in Eq. 6.4, I_a, I_b and I_c are the moment of inertia in each axis, and σ is the symmetry number of the isomer. The symmetry number is obtained from the point group of a molecule. It is obtained by counting the number of elements excluding the identity and

rotations of the point group.[219] To calculate the point group, I used Gaussian 09[220]. The point group of Ih is IH, Dh is D5H, Oh is OH and LM is C1. The σ for IH, OH, D5H and C1 is 60, 24, 10 and 1, respectively.

The vibrational partition function (q_{vib}) is approximated by Harmonic Oscillator approximations. In Eq. 6.5, ν_b is the frequency of b vibrational modes. For large size clusters, a lot of vibrational modes are observed having small frequencies. The contribution to q_{vib} from such frequencies is large, which overestimates the q_{vib} as the vibrations become anharmonic. To decrease the error in calculation of q_{vib} and make a harmonic approximation, Z. H. Li,[218] raised the small frequencies to a high frequency by setting a cut-off frequency. All the smaller modes frequency values are raised to the cutoff frequency value. The maximum and the minimum frequency observed in Au_{309} is 160 cm^{-1} and 3.5 cm^{-1}, respectively. I arbitrarily chose 80 cm^{-1}(10 meV) as the cut-off frequency and below 80 cm^{-1} the frequency are treated as small frequencies and raised to 80 cm^{-1} in calculations.

$$P^i_{qrov} = \frac{q^i_{rot} q^i_{vib}}{\sum_{i=1}^{isomers} q^i_{rot} q^i_{vib}} \tag{6.3}$$

$$q^i_{rot} = \left(\frac{8\pi^2 kT}{h^2}\right)^{\frac{3}{2}} \frac{\sqrt{\pi I^i_a I^i_b I^i_c}}{\sigma^i} \tag{6.4}$$

$$q^i_{vib} = \prod_b \frac{e^{-\frac{hc\nu_b}{2kT}}}{1 - e^{-\frac{hc\nu_b}{kT}}} \tag{6.5}$$

The probability (P_{qrov}) of an isomer i is calculated from q_{rot} and q_{vib}, as given by Eq. 6.3. The P_{qrov} are calculated for the isomers at 300 K, 500 K, 800 K and 1100 K as shown in Table 6.6. The probability P_{qrov} gives a deeper insight into the formation of isomers dependent upon the partition functions. It can be seen from Table 6.6, at 300K, the P_{qrov} is almost zero for the LM ($1.53\times\ 10^{-5}$), whereas, it is maximum for Ih (0.92116). The probability of Oh (0.06356) and Dh (0.01527) isomers is also high as compared to the LM structure. As the temperature is increased to 500 K, the P_{qrov} of Ih decreases to 0.92067. But, the P_{qrov} of Dh, Oh and LM increases to 0.01562, 0.06369 and $1.73\times\ 10^{-5}$, respectively. This

trend is continued till the temperature of 1100 K for Ih, Dh and LM. The probability of Oh decreases as temperature increases from 800 K to 1100 K. Overall, the Ih structure is probable from 300 K up to 1100 K. The probability of LM structure is very small when compared to Ih, Dh and Oh structures. The Dh and Oh isomer becomes more probable as the temperature is increased. At all the temperatures, the LM structure is the least probable and therefore despite being lower in energy than Ih, Dh and Oh structure, such structures may be formed in very small percentage in the experiments. This is in agreement with the study by Foster et al[211] and Wells et al,[213] where, amorphous geometries have been identified but in a very small percentage for gold nanoclusters.

Among the four isomers of Au_{309}, it is observed that above cut-off frequency, the magnitude of the vibrational modes for the LM structure is higher in comparison to symmetric structures. The Dh, Oh and Ih structures have fewer modes with high frequency. Therefore, the value of vibrational partition function is comparatively low for LM structure and high for Ih, Dh and Oh structures. On the other hand, in the rotational partition function, the symmetry number in the denominator of q_{rot} is 1 for LM structure and 10, 24, 60 for Dh, Oh and Ih, respectively. It gives relatively higher value of q_{rot} for LM structure than the Ih, Dh and Oh structures. But as $q_{rov} = q_{vib} \times q_{rot}$, the vibrational partition function dominates and gives higher probability for symmetric structures when compared to LM structure. As the temperature is increased, the magnitude of vibrational partition function increases and highly dominates over the contribution from rotational partition function. So, the analysis shows that symmetric clusters have more chances to form and are stable at high temperatures due to vibrational part of the partition function. The q_{rot} and q_{vib} values for the four isomers of Au_{309} is provided in the Table 6.5. The vibrational modes calculation involves the calculation of force constants. The interatomic force constant is dependent on the interatomic forces. The accurate calculation of interatomic forces gives the accurate estimation of atomic positions and thus the fitting of forces in ANN should be accurate.

Table 6.5. The rotational (q_{rot}) and vibrational (q_{vib}) partition function of 4 isomers of Au_{309} at different temperatures

Isomer	Type	300K	500K	800K	1100K
Ih	q_{rot}	3.68×10^{11}	7.93×10^{11}	16.04×10^{11}	25.86×10^{11}
	q_{vib}	9.75×10^{-307}	2.43×10^{-100}	1.24×10^{89}	4.83×10^{216}
Oh	q_{rot}	3.81×10^{11}	8.19×10^{11}	16.58×10^{11}	26.73×10^{11}
	q_{vib}	0.65×10^{-307}	0.162×10^{-100}	0.083×10^{89}	0.324×10^{216}
Dh	q_{rot}	3.79×10^{11}	8.16×10^{11}	16.52×10^{11}	26.63×10^{11}
	q_{vib}	0.15×10^{-307}	0.04×10^{-100}	0.02×10^{89}	0.08×10^{216}
LM	q_{rot}	3.86×10^{11}	8.31×10^{11}	16.82×10^{11}	27.12×10^{11}
	q_{vib}	1.5×10^{-311}	4.3×10^{-105}	2.3×10^{84}	9.18×10^{211}

The Set-II weights predicts the accurate relative energy, whereas, the Set-I weights predicts accurate interatomic forces. The interatomic forces in gold nanoclusters for a dataset consisting of environments for Au_{30}-Au_{147} are fitted with an error of 84.74 meV/Å/atom using Set-I weights. When these weights are applied to estimate the forces of a few Au_{309}, an average error of 14 meV/Å/ atom in the prediction of atomic forces is observed. Due to such a small error in the prediction of forces, a fair estimation of force constants is obtained. Due to this small error, MD simulations and local optimization of the structures are also conducted.

Since the probability is highly governed by q_{vib}, the prediction of vibrational frequency from DFT and ANN is compared. As the computational time for calculation of vibrational modes for Au_{309} is huge, I took small sized clusters of Au_{34} and Au_{58} whose calculations are computationally feasible. Four different types of clusters of Au_{34} and Au_{58} each was taken and vibrational frequency was estimated using DFT (In VASP, IBRION=5, POTIM=0.015). The values of vibrational frequency do not matches exactly with those calculated using ANN (Set-I weights). The order of the probability(P_{qrov}) calculated using vibrational frequency from DFT and ANN are found to be in agreement with each other. The structure of the isomers is shown in Fig. 6.15 and 6.16. The P_{qrov} data is provided in Table 6.7 and 6.8. This shows the capability of ANN potential to predict the accurate probabilities of isomers at different temperatures.

Table 6.6. The probability P_{qrov} of Ih, Dh Oh and LM structure of Au_{309} at different temperatures

Isomer	300K	500K	800K	1100K
Ih	0.92116	0.92067	0.92051	0.92046
Oh(fcc)	0.06356	0.06369	0.06377	0.06374
Dh	0.01527	0.01562	0.01574	0.01577
LM	$1.53\times\ 10^{-5}$	$1.73\times\ 10^{-5}$	$1.80\times\ 10^{-5}$	$1.83\times\ 10^{-5}$

Table 6.7. The probability P_{qrov} of 4 isomers of Au_{34} at different temperatures

Isomer	Type	300K	500K	800K
1	ANN	0.2486	0.2489	0.2490
	DFT	0.2150	0.2166	0.2170
2	ANN	0.1296	0.1312	0.1317
	DFT	0.0835	0.0854	0.086
3	ANN	0.3721	0.3696	0.3688
	DFT	0.4486	0.4441	0.4425
4	ANN	0.2496	0.2501	0.2504
	DFT	0.2522	0.2538	0.2543

Table 6.8. The probability P_{qrov} of 4 isomers of Au_{58} at different temperatures

Isomer	Type	300K	500K	800K
1	ANN	0.2254	0.2258	0.2261
	DFT	0.1859	0.1873	0.1877
2	ANN	0.1578	0.1595	0.1600
	DFT	0.1527	0.1548	0.1555
3	ANN	0.2613	0.2612	0.2614
	DFT	0.239	0.2406	0.2408
4	ANN	0.3554	0.3534	0.3527
	DFT	0.4214	0.4173	0.4158

Thus, a finite temperature probability analysis performed by incorporating rotational and vibrational partition function has given a quantitative insight for the experimentally obtained results.

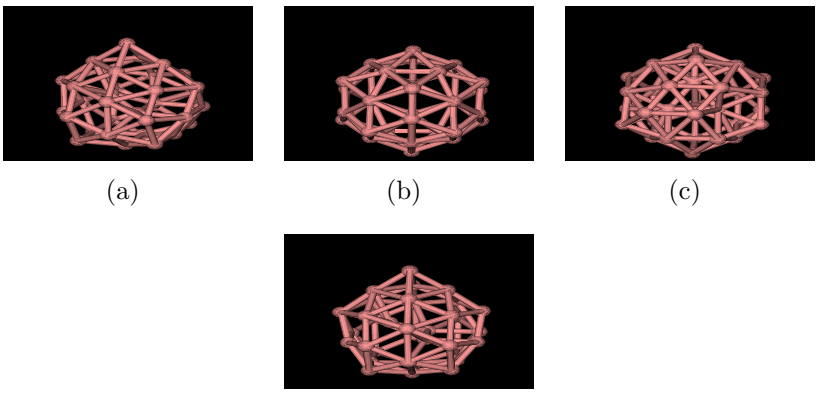

(a) (b) (c)

(d)

Figure 6.15. The four isomers of Au_{34} (a) 1, (b) 2, (c) 3, (d) 4

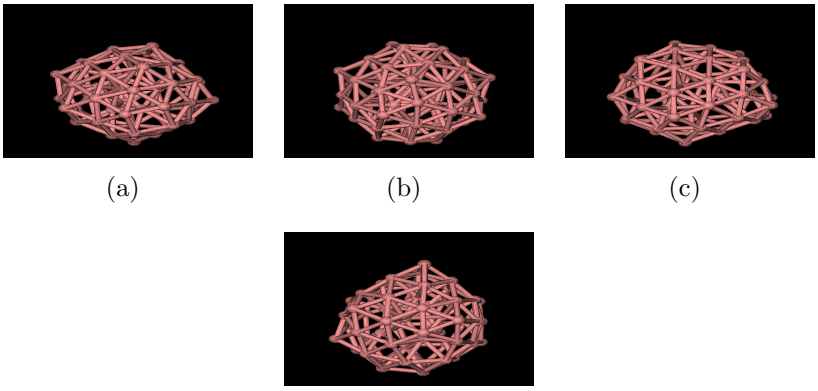

(a) (b) (c)

(d)

Figure 6.16. The four isomers of Au_{58} (a) 1, (b) 2, (c) 3, (d) 4

6.5 Summary

In this Chapter, the evolution of gold from cluster to a Np by proposing new numbers which shows a symmetric core evolution in the growth of gold Nps is presented. The exceptional pattern recognizing capability of ANN has made it possible to accurately predict structures up to a size of ∼3.3 nm. The structures till a size of ∼3.3 nm are not completely amorphous and a symmetric core is identified with amorphous layers of atoms over it. The "magic" number in metallic Nps (13, 55, 147, 309, 561 and 923), do not prefer symmetric structures in gold. The probability for atoms to move towards surface in gold Nps is very high, leading to requirement of more atoms on the surface to stabilize a compact core structure. Therefore, a plausible evolution of a symmetric core in gold Nps is shown. The

nucleation begins with a 12 atom symmetric structure, and two layers of atoms are deposited over it in Au_{160}. The next number is Au_{327}, where 54 atoms form a symmetric core with two layers of atoms deposited over it to keep the core stabilized. Further symmetric core arises in Au_{571}, where 146 atoms form a symmetric core, with the deposition of two layers over the core structure. These numbers reveal that gold Nps have a slow evolution towards bulk structure and therefore they have a high reactivity till a size of $\sim 3.3nm$. A finite temperature probability analysis of Au_{309} is also performed. The isomers lying higher in energy than the most stable structure are found to be more probable at different temperatures. The results obtained from the analysis has shown that the PE is not the only parameter for measuring the abundance of a structure in a population.

Chapter 7

Conclusion and Future scope

7.1 Conclusion

In last few decades, ML has become one of the major tool to solve a problem which is beyond the processing of a human brain. The learning and processing of the information by a machine leads to discoveries of different trends present in a database. ML techniques capture the intricacies in a system and find a relationship between different parameters.

ANN is one of the robust ML technique that mimics the learning process of a human brain using the basics of a perceptron model. The computational efficiency of ANN has inspired scientists to use it for solving complex quantum chemical problems. Exploration of PES of a molecule is one such problem which can be solved using ANN. To explore a PES, interatomic potential is required that gives the energy of the system. The most accurate interatomic potentials are obtained from ab initio methods. These methods consists of electronic structure dependent calculations that gives accurate properties but at a high computational cost for the experimentally relevant systems. ANN bridges the gap between accuracy of ab initio methods and low computational costs.

Metallic Nps have a variety of applications which makes them an important topic to study theoretically. The theoretical study of their properties is made feasible by efficient interatomic potentials which describe the atomic and molecular interactions. The study of structural dynamics of Nps leads to major insights into vacancy defects, surface energy, mechanical properties, plasmon-resonance behavior. The structural dynamics

analysis is thus impossible to conduct at a broader scale for large size systems using ab initio methods.

The goal of this thesis was to construct ANN interatomic potentials for studying the structural dynamics of metallic Nps (especially gold Nps and its alloys) having an accuracy of ab initio but at a much faster computational speed. The major reason to choose ANN is that it captures the complex bonding patterns in a system and find a relationship between coordinates and energy. As gold shows a rugged PES due to relativistic effects, the fitting of PES was possible with ANN.

For constructing a PES using ANN, one of the most important ingredient is the descriptors of the atomic environment. Before this thesis work, ANN was not applied to fit the PES of large size gold Nps. Also, a transferable approach for fitting energy and force of an alloy system was not done prior to the work done in this thesis. The proposed descriptors and various new models have proved to be of great significance in fitting the PES of complex system like gold. The results obtained shows the efficiency of ML techniques, especially ANN in fitting different properties of chemical systems. In brief, the major findings of the thesis are listed as:

1. Power spectrum coefficients as input descriptors to ANN leads to an accurate PES fitting tool for gold nanoclusters. The computational time for accurate calculation of energy and forces using power spectrum-ANN for a Au_{147} cluster is in seconds, which is very fast when compared to DFT ($\sim$ hours) (calculation done on parallelized 8 CPU [GenuineIntel 2600.0 MHz]).

2. Bispectrum - an order higher than power spectrum, is capable of capturing the atomic environments more efficiently than power spectrum. It resulted in searching more number of structures as compared to power spectrum driven structure exploration.

3. For an alloy system, the PES can be fitted using a single ANN by following a strategy of decoupled fitting of energy and forces. The

elements are differentiated between each other using weightings in the descriptors. The atomic forces are derived from gradients that are weighted according to the type of element.

4. The approach proposed for alloy systems is "transferable" as the parameters are dependent on interatomic distances, effective nuclear charges of the chemical species and reduced mass of the bonds involved in a chemical system. The ANN weights fitted for an alloy (Eg. $(AgAu)_{55}$-$(AgAu)_{147}$) can be used to predict energy and forces for an individual system (Eg. pure Ag or pure Au clusters).

5. The PES fitted for small and medium sized clusters($\sim$1.8 nm) is transferable to larger size clusters($<$3.3 nm).

6. A symmetric core evolution in gold nanoclusters is observed to occur at Au_{160}, Au_{327}, Au_{571}, which can be recognized as new magic numbers. In these clusters, the symmetric core is a Ih without the central atom.

7. A finite temperature probability analysis of gold clusters shows that the potential energy is not the only parameter for measuring the abundance of a structure in a population. The statistical analysis gives the preference of symmetric structures over amorphous structures in a sample.

7.2 Future Scope

The work that can be taken forward from this thesis can be summarized as

- The methodology presented in this thesis is tested on gold Nps and its alloys. The same scheme can be tested on a variety of nanomaterials for efficient mapping of PES from coordinates to energy. Other than ANN, there are various ML techniques which can be tried and modified according to the system in consideration.

- As thermodynamical quantities play a role in preferring one structure over another, an ML model can be created with descriptors having information about local structure environment as well as some data from thermodynamics. This will give a combine boost to the exploration of PES and thus a more accurate discovery of stable structures can be carried out.

- The approach to construct the training data set can be altered by using the DFT data calculated with different functionals. Doing so, the accuracy of the fitted energy can be improved and thus improving the PES.

- The complexity of a system increases with the presence of a lot of stable isomers at a particular temperature. A statistical tool for identifying such systems and devising a proper ML technique to fit its properties can be worked upon.

- The overfitting and the underfitting of the ANN weights can be tackled by a "choosing" mechanism, in which the hidden layers and the neurons are added or subtracted on the fly depending upon the probability analysis at each neuron.

- The foundation of DFT is 3 dimensional electron density, using which energy functionals are calculated and properties are estimated. Using ML, electron density can be modeled and estimated for an atomic arrangement. Once the electron density is obtained, the computational burden of DFT is reduced and thus it can be applied to a large size particle.

- Applications such as catalysis using ML approach can be studied. The reduction of carbon dioxide on gold Nps is one such important system that can be worked upon. The ML can simplify the identification of the structure of Np which can efficiently carry out the reduction.

- Different types of atomic environment descriptors can be designed to differentiate between stable and non-stable environments such that computational load of fitting a dataset is reduced.

- A global optimization strategy can be constructed using ML. The identification of very high energy isomers as well as the clustering of similar energy isomers can be done using a trained set of parameters. The identified structures can be modified by using gradient dependent approach to explore different minima basins.

Bibliography

[1] Andrew W Senior, Richard Evans, John Jumper, James Kirkpatrick, Laurent Sifre, Tim Green, Chongli Qin, Augustin Žídek, Alexander WR Nelson, Alex Bridgland, et al. Improved protein structure prediction using potentials from deep learning. *Nature*, 577(7792):706–710, 2020.

[2] Maxwell W Libbrecht and William Stafford Noble. Machine learning applications in genetics and genomics. *Nature Reviews Genetics*, 16(6):321–332, 2015.

[3] Marielle Malfante, Mauro Dalla Mura, Jean-Philippe Métaxian, Jerome I Mars, Orlando Macedo, and Adolfo Inza. Machine learning for volcano-seismic signals: Challenges and perspectives. *IEEE Signal Processing Magazine*, 35(2):20–30, 2018.

[4] Paul Raccuglia, Katherine C Elbert, Philip DF Adler, Casey Falk, Malia B Wenny, Aurelio Mollo, Matthias Zeller, Sorelle A Friedler, Joshua Schrier, and Alexander J Norquist. Machine-learning-assisted materials discovery using failed experiments. *Nature*, 533(7601):73–76, 2016.

[5] Warren S McCulloch and Walter Pitts. A logical calculus of the ideas immanent in nervous activity. *The bulletin of mathematical biophysics*, 5(4):115–133, 1943.

[6] Donald Olding Hebb. *The organization of behavior: A neuropsychological theory*. Psychology Press, 2005.

[7] Frank Rosenblatt. The perceptron: a probabilistic model for infor-

mation storage and organization in the brain. *Psychological review*, 65(6):386, 1958.

[8] Arthur L Samuel. Some studies in machine learning using the game of checkers. *IBM Journal of research and development*, 3(3):210–229, 1959.

[9] Bernard Widrow and Marcian E Hoff. Adaptive switching circuits. Technical report, Stanford Univ Ca Stanford Electronics Labs, 1960.

[10] John J Hopfield. Neural networks and physical systems with emergent collective computational abilities. *Proceedings of the national academy of sciences*, 79(8):2554–2558, 1982.

[11] Jure Zupan and Johann Gasteiger. Neural networks: A new method for solving chemical problems or just a passing phase? *Analytica Chimica Acta*, 248(1):1–30, 1991.

[12] Ning Qian, Terrence J Sejnowski, et al. Predicting the secondary structure of globular proteins using neural network models. *Journal of molecular biology*, 202(4):865–884, 1988.

[13] Burkhard Rost, Chris Sander, et al. Prediction of protein secondary structure at better than 70% accuracy. *Journal of molecular biology*, 232(2):584–599, 1993.

[14] Burkhard Rost and Chris Sander. Combining evolutionary information and neural networks to predict protein secondary structure. *Proteins: Structure, Function, and Bioinformatics*, 19(1):55–72, 1994.

[15] Kenta Nakai and Minoru Kanehisa. Expert system for predicting protein localization sites in gram-negative bacteria. *Proteins: Structure, Function, and Bioinformatics*, 11(2):95–110, 1991.

[16] Henrik Nielsen, Jacob Engelbrecht, Søren Brunak, and Gunnar Von Heijne. A neural network method for identification of prokaryotic and eukaryotic signal peptides and prediction of their cleavage sites. *International journal of neural systems*, 8(05n06):581–599, 1997.

[17] Ernest W Robb and Morton E Munk. A neural network approach to infrared spectrum interpretation. *Microchimica Acta*, 100(3-4):131–155, 1990.

[18] Kazutoshi Tanabe, Tadao Tamura, and Hiroyuki Uesaka. Neural network system for the identification of infrared spectra. *Applied spectroscopy*, 46(5):807–810, 1992.

[19] JA Darsey, DW Noid, and BR Upadhyaya. Application of neural network computing to the solution for the ground-state eigenenergy of two-dimensional harmonic oscillators. *Chemical physics letters*, 177(2):189–194, 1991.

[20] J Androsiuk, L Kułak, and K Sienicki. Neural network solution of the schrödinger equation for a two-dimensional harmonic oscillator. *Chemical physics*, 173(3):377–383, 1993.

[21] BG Sumpter and DW Noid. On the use of computational neural networks for the prediction of polymer properties. *Journal of thermal analysis*, 46(3-4):833–851, 1996.

[22] Xue-Mei Duan, Zhen-Hua Li, Guo-Liang Song, Wen-Ning Wang, Guan-Hua Chen, and Kang-Nian Fan. Neural network correction for heats of formation with a larger experimental training set and new descriptors. *Chemical physics letters*, 410(1-3):125–130, 2005.

[23] Frederico V Prudente, Paulo H Acioli, and JJ Soares Neto. The fitting of potential energy surfaces using neural networks: Application to the study of vibrational levels of h 3+. *The Journal of chemical physics*, 109(20):8801–8808, 1998.

[24] Sergei Manzhos, Xiaogang Wang, Richard Dawes, and Tucker Carrington. A nested molecule-independent neural network approach for high-quality potential fits. *The Journal of Physical Chemistry A*, 110(16):5295–5304, 2006.

[25] Sönke Lorenz, Axel Groß, and Matthias Scheffler. Representing high-dimensional potential-energy surfaces for reactions at surfaces by neural networks. *Chemical Physics Letters*, 395(4-6):210–215, 2004.

[26] Thomas B Blank, Steven D Brown, August W Calhoun, and Douglas J Doren. Neural network models of potential energy surfaces. *The Journal of chemical physics*, 103(10):4129–4137, 1995.

[27] Jerry A Darsey, Ashish G Soman, and Don W Noid. Artificial neural system modeling of monte carlo simulations of polymers. *Macromolecular Theory and Simulations*, 2(5):711–719, 1993.

[28] Włodzisław Duch and Geerd HF Diercksen. Neural networks as tools to solve problems in physics and chemistry. *Computer physics communications*, 82(2-3):91–103, 1994.

[29] Jörg Behler and Michele Parrinello. Generalized neural-network representation of high-dimensional potential-energy surfaces. *Physical review letters*, 98(14):146401, 2007.

[30] Nongnuch Artrith, Björn Hiller, and Jörg Behler. Neural network potentials for metals and oxides–first applications to copper clusters at zinc oxide. *physica status solidi (b)*, 250(6):1191–1203, 2013.

[31] Siva Chiriki, Shweta Jindal, and Satya S Bulusu. Neural network potentials for dynamics and thermodynamics of gold nanoparticles. *The Journal of chemical physics*, 146(8):084314, 2017.

[32] Chris M Handley and Paul LA Popelier. Potential energy surfaces fitted by artificial neural networks. *The Journal of Physical Chemistry A*, 114(10):3371–3383, 2010.

[33] Sönke Lorenz, Axel Groß, and Matthias Scheffler. Representing high-dimensional potential-energy surfaces for reactions at surfaces by neural networks. *Chemical Physics Letters*, 395(4-6):210–215, 2004.

[34] Bin Jiang and Hua Guo. Permutation invariant polynomial neural network approach to fitting potential energy surfaces. *The Journal of chemical physics*, 139(5):054112, 2013.

[35] Stefan Chmiela, Alexandre Tkatchenko, Huziel E Sauceda, Igor Poltavsky, Kristof T Schütt, and Klaus-Robert Müller. Machine learning of accurate energy-conserving molecular force fields. *Science advances*, 3(5):e1603015, 2017.

[36] John C Snyder, Matthias Rupp, Katja Hansen, Klaus-Robert Müller, and Kieron Burke. Finding density functionals with machine learning. *Physical review letters*, 108(25):253002, 2012.

[37] Kristof T Schütt, Farhad Arbabzadah, Stefan Chmiela, Klaus R Müller, and Alexandre Tkatchenko. Quantum-chemical insights from deep tensor neural networks. *Nature communications*, 8:13890, 2017.

[38] John Edward Lennard-Jones. On the determination of molecular fields. ii. from the equation of state of gas. *Proc. Roy. Soc. A*, 106:463–477, 1924.

[39] Louis A Girifalco and Victor G Weizer. Application of the morse potential function to cubic metals. *Physical Review*, 114(3):687, 1959.

[40] Raju P Gupta. Lattice relaxation at a metal surface. *Physical Review B*, 23(12):6265, 1981.

[41] Murray S Daw and Michael I Baskes. Embedded-atom method: Derivation and application to impurities, surfaces, and other defects in metals. *Physical Review B*, 29(12):6443, 1984.

[42] S. M. Foiles, M. I. Baskes, and M. S. Daw. Embedded-atom-method functions for the fcc metals cu, ag, au, ni, pd, pt, and their alloys. *Phys. Rev. B*, 33:7983–7991, Jun 1986.

[43] John N Murrell and Rachel E Mottram. Potential energy functions for atomic solids. *Molecular physics*, 69(3):571–585, 1990.

[44] MW Finnis and JE Sinclair. A simple empirical n-body potential for transition metals. *Philosophical Magazine A*, 50(1):45–55, 1984.

[45] BWH Van Beest, Gert Jan Kramer, and RA Van Santen. Force fields for silicas and aluminophosphates based on ab initio calculations. *Physical Review Letters*, 64(16):1955, 1990.

[46] Kenno Vanommeslaeghe, Elizabeth Hatcher, Chayan Acharya, Sibsankar Kundu, Shijun Zhong, Jihyun Shim, Eva Darian, Olgun Guvench, P Lopes, Igor Vorobyov, et al. Charmm general force field: A force field for drug-like molecules compatible with the charmm all-atom additive biological force fields. *Journal of computational chemistry*, 31(4):671–690, 2010.

[47] Geza Fogarasi and Peter Pulay. Ab initio vibrational force fields. *Annual Review of Physical Chemistry*, 35(1):191–213, 1984.

[48] Kimberly Chenoweth, Adri CT Van Duin, and William A Goddard. Reaxff reactive force field for molecular dynamics simulations of hydrocarbon oxidation. *The Journal of Physical Chemistry A*, 112(5):1040–1053, 2008.

[49] Thomas P Senftle, Sungwook Hong, Md Mahbubul Islam, Sudhir B Kylasa, Yuanxia Zheng, Yun Kyung Shin, Chad Junkermeier, Roman Engel-Herbert, Michael J Janik, Hasan Metin Aktulga, et al. The reaxff reactive force-field: development, applications and future directions. *npj Computational Materials*, 2(1):1–14, 2016.

[50] Jörg Behler. Constructing high-dimensional neural network potentials: A tutorial review. *International Journal of Quantum Chemistry*, 115(16):1032–1050, 2015.

[51] Albert P Bartók, Mike C Payne, Risi Kondor, and Gábor Csányi. Gaussian approximation potentials: The accuracy of quantum mechanics, without the electrons. *Physical review letters*, 104(13):136403, 2010.

[52] Albert P Bartók, Risi Kondor, and Gábor Csányi. On representing chemical environments. *Physical Review B*, 87(18):184115, 2013.

[53] Matthias Rupp, Alexandre Tkatchenko, Klaus-Robert Müller, and O Anatole Von Lilienfeld. Fast and accurate modeling of molecular atomization energies with machine learning. *Physical review letters*, 108(5):058301, 2012.

[54] Venkatesh Botu and Rampi Ramprasad. Learning scheme to predict atomic forces and accelerate materials simulations. *Physical Review B*, 92(9):094306, 2015.

[55] Aidan P Thompson, Laura P Swiler, Christian R Trott, Stephen M Foiles, and Garritt J Tucker. Spectral neighbor analysis method for automated generation of quantum-accurate interatomic potentials. *Journal of Computational Physics*, 285:316–330, 2015.

[56] Oliver T Unke and Markus Meuwly. A reactive, scalable, and transferable model for molecular energies from a neural network approach based on local information. *The Journal of chemical physics*, 148(24):241708, 2018.

[57] John E Herr, Kevin Koh, Kun Yao, and John Parkhill. Compressing physics with an autoencoder: Creating an atomic species representation to improve machine learning models in the chemical sciences. *The Journal of chemical physics*, 151(8):084103, 2019.

[58] Geoffrey E Hinton and Ruslan R Salakhutdinov. Reducing the dimensionality of data with neural networks. *science*, 313(5786):504–507, 2006.

[59] Matthew Hirn, Stéphane Mallat, and Nicolas Poilvert. Wavelet scattering regression of quantum chemical energies. *Multiscale Modeling & Simulation*, 15(2):827–863, 2017.

[60] Michael Eickenberg, Georgios Exarchakis, Matthew Hirn, and Stéphane Mallat. Solid harmonic wavelet scattering: Predicting

quantum molecular energy from invariant descriptors of 3d electronic densities. In *Advances in Neural Information Processing Systems*, pages 6540–6549, 2017.

[61] Nongnuch Artrith, Tobias Morawietz, and Jörg Behler. High-dimensional neural-network potentials for multicomponent systems: Applications to zinc oxide. *Physical Review B*, 83(15):153101, 2011.

[62] Nongnuch Artrith, Alexander Urban, and Gerbrand Ceder. Efficient and accurate machine-learning interpolation of atomic energies in compositions with many species. *Physical Review B*, 96(1):014112, 2017.

[63] Steven Hobday, Roger Smith, and Joe Belbruno. Applications of neural networks to fitting interatomic potential functions. *Modelling and Simulation in Materials Science and Engineering*, 7(3):397, 1999.

[64] Kun Yao, John E Herr, David W Toth, Ryker Mckintyre, and John Parkhill. The tensormol-0.1 model chemistry: a neural network augmented with long-range physics. *Chemical science*, 9(8):2261–2269, 2018.

[65] Kristof T Schütt, Huziel E Sauceda, P-J Kindermans, Alexandre Tkatchenko, and K-R Müller. Schnet–a deep learning architecture for molecules and materials. *The Journal of Chemical Physics*, 148(24):241722, 2018.

[66] Jie Zhou, Ganqu Cui, Zhengyan Zhang, Cheng Yang, Zhiyuan Liu, Lifeng Wang, Changcheng Li, and Maosong Sun. Graph neural networks: A review of methods and applications. *arXiv preprint arXiv:1812.08434*, 2018.

[67] Thomas N Kipf and Max Welling. Semi-supervised classification with graph convolutional networks. *arXiv preprint arXiv:1609.02907*, 2016.

[68] Justin Gilmer, Samuel S Schoenholz, Patrick F Riley, Oriol Vinyals, and George E Dahl. Neural message passing for quantum chemistry. In *Proceedings of the 34th International Conference on Machine Learning-Volume 70*, pages 1263–1272. JMLR. org, 2017.

[69] Thomas Hofmann, Bernhard Schölkopf, and Alexander J Smola. Kernel methods in machine learning. *The annals of statistics*, pages 1171–1220, 2008.

[70] Thomas Hofmann, Bernhard Schölkopf, and Alexander J Smola. A review of kernel methods in machine learning. *Mac-Planck-Institute Technical Report*, 156, 2006.

[71] Ioannis Tsochantaridis, Thomas Hofmann, Thorsten Joachims, and Yasemin Altun. Support vector machine learning for interdependent and structured output spaces. In *Proceedings of the twenty-first international conference on Machine learning*, page 104, 2004.

[72] Stuart Andrews, Ioannis Tsochantaridis, and Thomas Hofmann. Support vector machines for multiple-instance learning. In *Advances in neural information processing systems*, pages 577–584, 2003.

[73] Dong C Liu and Jorge Nocedal. On the limited memory bfgs method for large scale optimization. *Mathematical programming*, 45(1-3):503–528, 1989.

[74] Greg Welch, Gary Bishop, et al. An introduction to the kalman filter. 1995.

[75] Simon Haykin. *Kalman filtering and neural networks*, volume 47. John Wiley & Sons, 2004.

[76] James B Witkoskie and Douglas J Doren. Neural network models of potential energy surfaces: Prototypical examples. *Journal of chemical theory and computation*, 1(1):14–23, 2005.

[77] Jorge J Moré. The levenberg-marquardt algorithm: implementation and theory. In *Numerical analysis*, pages 105–116. Springer, 1978.

[78] Robert Hecht-Nielsen. Theory of the backpropagation neural network. In *Neural networks for perception*, pages 65–93. Elsevier, 1992.

[79] Martin F Møller. *A scaled conjugate gradient algorithm for fast supervised learning*. Aarhus University, Computer Science Department, 1990.

[80] Diederik P Kingma and Jimmy Ba. Adam: A method for stochastic optimization. *arXiv preprint arXiv:1412.6980*, 2014.

[81] Paul J Steinhardt, David R Nelson, and Marco Ronchetti. Icosahedral bond orientational order in supercooled liquids. *Physical Review Letters*, 47(18):1297, 1981.

[82] Paul J Steinhardt, David R Nelson, and Marco Ronchetti. Bond-orientational order in liquids and glasses. *Physical Review B*, 28(2):784, 1983.

[83] JS Van Duijneveldt and D Frenkel. Computer simulation study of free energy barriers in crystal nucleation. *The Journal of chemical physics*, 96(6):4655–4668, 1992.

[84] Eduardo R Hernández and Jorge Iniguez. First-principles simulations on the nature of the melting line of sodium. *Physical review letters*, 98(5):055501, 2007.

[85] Jonathan PK Doye, Mark A Miller, and David J Wales. The double-funnel energy landscape of the 38-atom lennard-jones cluster. *The Journal of Chemical Physics*, 110(14):6896–6906, 1999.

[86] Lívia B Pártay, Albert P Bartók, and Gábor Csányi. Efficient sampling of atomic configurational spaces. *The Journal of Physical Chemistry B*, 114(32):10502–10512, 2010.

[87] R Biswas and DR Hamann. New classical models for silicon structural energies. *Physical Review B*, 36(12):6434, 1987.

[88] Risi Kondor. A novel set of rotationally and translationally invariant features for images based on the non-commutative bispectrum. *arXiv preprint cs/0701127*, 2007.

[89] FE Wagner, S Haslbeck, L Stievano, S Calogero, QA Pankhurst, and K-P Martinek. Before striking gold in gold-ruby glass. *Nature*, 407(6805):691–692, 2000.

[90] LB Hunt. The true story of purple of cassius. *Gold Bulletin*, 9(4):134–139, 1976.

[91] Michael Faraday. X. the bakerian lecture.—experimental relations of gold (and other metals) to light. *Philosophical Transactions of the Royal Society of London*, (147):145–181, 1857.

[92] Gustav Mie. Beiträge zur optik trüber medien, speziell kolloidaler metallösungen. *Annalen der physik*, 330(3):377–445, 1908.

[93] René Fournier and Satya Bulusu. *Closed-Shell Metal Clusters*. Springer, New York, NY, 2013.

[94] G. C. Bond. Introduction to the physical and chemical properties of gold. *Gold Nanoparticles for Physics, Chemistry and Biology, Imperial College Press, London*, pages 29–42, 2012.

[95] P. Pyykkö and J. P. Desclaux. Relativity and the periodic system of elements. *Accounts of Chemical Research*, 12(8):276–281, 1979.

[96] Peter Schwerdtfeger. Relativistic effects in properties of gold. *Heteroatom Chemistry: An International Journal of Main Group Elements*, 13(6):578–584, 2002.

[97] D. J. Gorin and F. D. Toste. Relativistic effects in homogeneous gold catalysis. *Nature*, 446(7134):395, 2007.

[98] Wei Huang, Min Ji, Chuan-Ding Dong, Xiao Gu, Lei-Ming Wang, Xin Gao Gong, and Lai-Sheng Wang. Relativistic effects and the

unique low-symmetry structures of gold nanoclusters. *Acs Nano*, 2(5):897–904, 2008.

[99] Y. Du, H. Sheng, D. Astruc, and M. Zhu. Atomically precise noble metal nanoclusters as efficient catalysts: A bridge between structure and properties. *Chemical reviews*, 2019.

[100] Balaram S Takale, Ming Bao, and Yoshinori Yamamoto. Gold nanoparticle (aunps) and gold nanopore (aunpore) catalysts in organic synthesis. *Organic & biomolecular chemistry*, 12(13):2005–2027, 2014.

[101] Xiao Yan Liu, Aiqin Wang, Tao Zhang, and Chung-Yuan Mou. Catalysis by gold: New insights into the support effect. *Nano Today*, 8(4):403–416, 2013.

[102] Nuria Lopez, TVW Janssens, BS Clausen, Y Xu, Manos Mavrikakis, T Bligaard, and Jens Kehlet Nørskov. On the origin of the catalytic activity of gold nanoparticles for low-temperature co oxidation. *Journal of Catalysis*, 223(1):232–235, 2004.

[103] Arne Wittstock and Marcus Bäumer. Catalysis by unsupported skeletal gold catalysts. *Accounts of chemical research*, 47(3):731–739, 2013.

[104] Mei Yan, Tienan Jin, Qiang Chen, Hon Eong Ho, Takeshi Fujita, Lu-Yang Chen, Ming Bao, Ming-Wei Chen, Naoki Asao, and Yoshinori Yamamoto. Unsupported nanoporous gold catalyst for highly selective hydrogenation of quinolines. *Organic letters*, 15(7):1484–1487, 2013.

[105] Takeshi Fujita, Pengfei Guan, Keith McKenna, Xingyou Lang, Akihiko Hirata, Ling Zhang, Tomoharu Tokunaga, Shigeo Arai, Yuta Yamamoto, Nobuo Tanaka, et al. Atomic origins of the high catalytic activity of nanoporous gold. *Nature materials*, 11(9):775, 2012.

[106] Partha Ghosh, Gang Han, Mrinmoy De, Chae Kyu Kim, and Vincent M Rotello. Gold nanoparticles in delivery applications. *Advanced drug delivery reviews*, 60(11):1307–1315, 2008.

[107] Y. Zhang, C. Zhang, C. Xu, X. Wang, C. Liu, G. Waterhouse, Y. Wang, and H. Yin. Ultrasmall au nanoclusters for biomedical and biosensing applications: A mini-review. *Talanta*, 2019.

[108] Tong-Tong Jia, G. Yang, Sai-Jun Mo, Zhao-Yang Wang, Bing-Jie Li, W. Ma, Yue-Xin Guo, X. Chen, X. Zhao, Jun-Qi Liu, et al. Atomically precise gold–levonorgestrel nanocluster as a radiosensitizer for enhanced cancer therapy. *ACS nano*, 2019.

[109] C. L. Cleveland, U. Landman, T. G. Schaaff, M. N. Shafigullin, P. W. Stephens, and R. L. Whetten. Structural evolution of smaller gold nanocrystals: The truncated decahedral motif. *Physical review letters*, 79(10):1873, 1997.

[110] E. Aprà, R. Ferrando, and A. Fortunelli. Density-functional global optimization of gold nanoclusters. *Physical Review B*, 73(20):205414, 2006.

[111] IL Garzón, K. Michaelian, MR Beltrán, A. Posada-Amarillas, P. Ordejón, E. Artacho, D. Sánchez-Portal, and JM Soler. Lowest energy structures of gold nanoclusters. *Physical review letters*, 81(8):1600, 1998.

[112] F. Pittaway, L. O. Paz-Borbón, R. L. Johnston, H. Arslan, R. Ferrando, C. Mottet, G. Barcaro, and A. Fortunelli. Theoretical studies of palladium- gold nanoclusters: Pd- au clusters with up to 50 atoms. *The Journal of Physical Chemistry C*, 113(21):9141–9152, 2009.

[113] Wei Huang, Satya Bulusu, Rhitankar Pal, Xiao Cheng Zeng, and Lai-Sheng Wang. Structural transition of gold nanoclusters: from the golden cage to the golden pyramid. *ACS nano*, 3(5):1225–1230, 2009.

[114] Hannu Häkkinen, Bokwon Yoon, Uzi Landman, Xi Li, Hua-Jin Zhai, and Lai-Sheng Wang. On the electronic and atomic structures of small au n-(n= 4- 14) clusters: A photoelectron spectroscopy and density-functional study. *The Journal of Physical Chemistry A*, 107(32):6168–6175, 2003.

[115] Satya Bulusu, Xi Li, Lai-Sheng Wang, and Xiao Cheng Zeng. Evidence of hollow golden cages. *Proceedings of the National Academy of Sciences*, 103(22):8326–8330, 2006.

[116] Jun Li, Xi Li, Hua-Jin Zhai, and Lai-Sheng Wang. Au20: A tetrahedral cluster. *Science*, 299(5608):864–867, 2003.

[117] Satya Bulusu, Xi Li, Lai-Sheng Wang, and Xiao Cheng Zeng. Structural transitions from pyramidal to fused planar to tubular to core/shell compact in gold clusters: Au n-(n= 21- 25). *The Journal of Physical Chemistry C*, 111(11):4190–4198, 2007.

[118] CD Dong and XG Gong. Gold cluster beyond hollow cage: A double shell structure of au 58. *The Journal of chemical physics*, 132(10):104301, 2010.

[119] Mark Turner, Vladimir B Golovko, Owain PH Vaughan, Pavel Abdulkin, Angel Berenguer-Murcia, Mintcho S Tikhov, Brian FG Johnson, and Richard M Lambert. Selective oxidation with dioxygen by gold nanoparticle catalysts derived from 55-atom clusters. *Nature*, 454(7207):981, 2008.

[120] Hui Li, Lei Li, Andreas Pedersen, Yi Gao, Navneet Khetrapal, Hannes Jónsson, and Xiao Cheng Zeng. Magic-number gold nanoclusters with diameters from 1 to 3.5 nm: Relative stability and catalytic activity for co oxidation. *Nano letters*, 15(1):682–688, 2014.

[121] Pekka Pyykkö. Structural properties: Magic nanoclusters of gold. *Nature nanotechnology*, 2(5):273, 2007.

[122] Siwei Luo. Discussion on the origin of magic numbers in clusters. *arXiv preprint arXiv:1411.1007*, 2014.

[123] H-G Boyen, G Kästle, F Weigl, B Koslowski, C Dietrich, P Ziemann, Joachim P Spatz, S Riethmüller, C Hartmann, M Möller, et al. Oxidation-resistant gold-55 clusters. *Science*, 297(5586):1533–1536, 2002.

[124] Thomas C Allison and YuYe J Tong. Evaluation of methods to predict reactivity of gold nanoparticles. *Physical Chemistry Chemical Physics*, 13(28):12858–12864, 2011.

[125] Hyesung An, Soonho Kwon, Hyunwoo Ha, Hyun You Kim, and Hyuck Mo Lee. Reactive structural motifs of au nanoclusters for oxygen activation and subsequent co oxidation. *The Journal of Physical Chemistry C*, 120(17):9292–9298, 2016.

[126] H-G Boyen, A Ethirajan, G Kästle, F Weigl, P Ziemann, G Schmid, MG Garnier, M Büttner, and P Oelhafen. Alloy formation of supported gold nanoparticles at their transition from clusters to solids: Does size matter? *Physical review letters*, 94(1):016804, 2005.

[127] J Oviedo and RE Palmer. Amorphous structures of cu, ag, and au nanoclusters from first principles calculations. *The Journal of chemical physics*, 117(21):9548–9551, 2002.

[128] Hannu Häkkinen and Michael Moseler. 55-atom clusters of silver and gold: Symmetry breaking by relativistic effects. *Computational materials science*, 35(3):332–336, 2006.

[129] CM Chang and MY Chou. Alternative low-symmetry structure for 13-atom metal clusters. *Physical review letters*, 93(13):133401, 2004.

[130] Seema Pande, Xingao Gong, Lai-Sheng Wang, and Xiao Cheng Zeng. Au60–: The smallest gold cluster with the high-symmetry icosahedral core au13. *The journal of physical chemistry letters*, 10(8):1820–1827, 2019.

[131] Stephanie G Lambie, Geoffrey R Weal, Caroline E Blackmore, Richard E Palmer, and Anna L Garden. Contrasting motif preferences of platinum and gold nanoclusters between 55 and 309 atoms. *Nanoscale Advances*, 2019.

[132] Maxime Van den Bossche. Dftb-assisted global structure optimization of 13-and 55-atom late transition metal clusters. *The Journal of Physical Chemistry A*, 123(13):3038–3045, 2019.

[133] Luiz FL Oliveira, Nathalie Tarrat, Jérôme Cuny, Joseph Morillo, Didier Lemoine, Fernand Spiegelman, and Mathias Rapacioli. Benchmarking density functional based tight-binding for silver and gold materials: From small clusters to bulk. *The Journal of Physical Chemistry A*, 120(42):8469–8483, 2016.

[134] Shweta Jindal, Siva Chiriki, and Satya S Bulusu. Spherical harmonics based descriptor for neural network potentials: Structure and dynamics of au147 nanocluster. *The Journal of chemical physics*, 146(20):204301, 2017.

[135] Shweta Jindal and Satya S Bulusu. An algorithm to use higher order invariants for modelling potential energy surface of nanoclusters. *Chemical Physics Letters*, 693:152–158, 2018.

[136] Nathalie Tarrat, Mathias Rapacioli, and Fernand Spiegelman. Au147 nanoparticles: Ordered or amorphous? *The Journal of chemical physics*, 148(20):204308, 2018.

[137] Max Born and Robert Oppenheimer. Zur quantentheorie der molekeln. *Annalen der physik*, 389(20):457–484, 1927.

[138] John C Slater. A simplification of the hartree-fock method. *Physical review*, 81(3):385, 1951.

[139] Pierre Hohenberg and Walter Kohn. Inhomogeneous electron gas. *Physical review*, 136(3B):B864, 1964.

[140] Andrew R Leach and Andrew R Leach. *Molecular modelling: principles and applications*. Pearson education, 2001.

[141] Georg Kresse and Jürgen Hafner. Ab initio molecular dynamics for liquid metals. *Physical Review B*, 47(1):558, 1993.

[142] Georg Kresse and Jürgen Hafner. Ab initio molecular-dynamics simulation of the liquid-metal–amorphous-semiconductor transition in germanium. *Physical Review B*, 49(20):14251, 1994.

[143] Georg Kresse and Jürgen Furthmüller. Efficiency of ab-initio total energy calculations for metals and semiconductors using a plane-wave basis set. *Computational materials science*, 6(1):15–50, 1996.

[144] Georg Kresse and Jürgen Furthmüller. Efficient iterative schemes for ab initio total-energy calculations using a plane-wave basis set. *Physical review B*, 54(16):11169, 1996.

[145] Peter E Blöchl. Projector augmented-wave method. *Physical review B*, 50(24):17953, 1994.

[146] John P Perdew, Kieron Burke, and Matthias Ernzerhof. Generalized gradient approximation made simple. *Physical review letters*, 77(18):3865, 1996.

[147] Kieron Burke, John P Perdew, and Matthias Ernzerhof. Why the generalized gradient approximation works and how to go beyond it. *International journal of quantum chemistry*, 61(2):287–293, 1997.

[148] E Fabiano, Lucian A Constantin, and F Della Sala. Exchange-correlation generalized gradient approximation for gold nanostructures. *The Journal of chemical physics*, 134(19):194112, 2011.

[149] Stefano A Serapian, Michael J Bearpark, and Fernando Bresme. The shape of au 8: gold leaf or gold nugget? *Nanoscale*, 5(14):6445–6457, 2013.

[150] Wen Wu Xu, Xiao Cheng Zeng, and Yi Gao. Au13 (8e): A secondary block for describing a special group of liganded gold clusters containing icosahedral au13 motifs. *Chemical Physics Letters*, 675:35–39, 2017.

[151] Wen Wu Xu, Xiao Cheng Zeng, and Yi Gao. The structural isomerism in gold nanoclusters. *Nanoscale*, 10(20):9476–9483, 2018.

[152] Chunyan Liu, Yingzi Tan, Sisi Lin, Hui Li, Xiaojun Wu, Lei Li, Yong Pei, and Xiao Cheng Zeng. Co self-promoting oxidation on nanosized gold clusters: Triangular au3 active site and co induced o–o scission. *Journal of the American Chemical Society*, 135(7):2583–2595, 2013.

[153] Fabrizio Cleri and Vittorio Rosato. Tight-binding potentials for transition metals and alloys. *Physical Review B*, 48(1):22, 1993.

[154] Tariq Rashid. *Make your own neural network*. CreateSpace Independent Publishing Platform, 2016.

[155] Jürgen Schmidhuber. Learning complex, extended sequences using the principle of history compression. *Neural Computation*, 4(2):234–242, 1992.

[156] John A Hertz. *Introduction to the theory of neural computation*. CRC Press, 2018.

[157] Moshe Leshno, Vladimir Ya Lin, Allan Pinkus, and Shimon Schocken. Multilayer feedforward networks with a nonpolynomial activation function can approximate any function. *Neural networks*, 6(6):861–867, 1993.

[158] David F Shanno. Conditioning of quasi-newton methods for function minimization. *Mathematics of computation*, 24(111):647–656, 1970.

[159] Christopher D Taylor. Connections between the energy functional and interaction potentials for materials simulations. *Physical Review B*, 80(2):024104, 2009.

[160] Olivier Michel and Patrick Flandrin. *Higher order statistics for chaotic signal analysis*. Control and Dynamic System, 1996.

[161] Ramakrishna Kakarala. The bispectrum as a source of phase-sensitive invariants for fourier descriptors: a group-theoretic approach. *Journal of Mathematical Imaging and Vision*, 44(3):341–353, 2012.

[162] YC Kim and EJ Powers. Digital bispectral analysis of self-excited fluctuation spectra. *The Physics of Fluids*, 21(8):1452–1453, 1978.

[163] Michael Gastegger, Ludwig Schwiedrzik, Marius Bittermann, Florian Berzsenyi, and Philipp Marquetand. wacsf—weighted atom-centered symmetry functions as descriptors in machine learning potentials. *The Journal of chemical physics*, 148(24):241709, 2018.

[164] Hans C Andersen. Molecular dynamics simulations at constant pressure and/or temperature. *The Journal of chemical physics*, 72(4):2384–2393, 1980.

[165] Martin J Field, Paul A Bash, and Martin Karplus. A combined quantum mechanical and molecular mechanical potential for molecular dynamics simulations. *Journal of Computational Chemistry*, 11(6):700–733, 1990.

[166] Helmut Grubmüller, Helmut Heller, Andreas Windemuth, and Klaus Schulten. Generalized verlet algorithm for efficient molecular dynamics simulations with long-range interactions. *Molecular Simulation*, 6(1-3):121–142, 1991.

[167] Kurt Binder, Dieter Heermann, Lyle Roelofs, A John Mallinckrodt, and Susan McKay. Monte carlo simulation in statistical physics. *Computers in Physics*, 7(2):156–157, 1993.

[168] David J Wales and Harold A Scheraga. Global optimization of clusters, crystals, and biomolecules. *Science*, 285(5432):1368–1372, 1999.

[169] Lixin Zhan, Bart Piwowar, Wing-Ki Liu, PJ Hsu, SK Lai, and Jeff ZY Chen. Multicanonical basin hopping: A new global optimization method for complex systems. *The Journal of chemical physics*, 120(12):5536–5542, 2004.

[170] Lixin Zhan, Jeff ZY Chen, Wing-Ki Liu, and SK Lai. Asynchronous multicanonical basin hopping method and its application to cobalt nanoclusters. *The Journal of chemical physics*, 122(24):244707, 2005.

[171] Bernd A Berg. Algorithmic aspects of multicanonical simulations. *Nuclear Physics B-Proceedings Supplements*, 63(1-3):982–984, 1998.

[172] Yi Gao, Nan Shao, Yong Pei, Zhongfang Chen, and Xiao Cheng Zeng. Catalytic activities of subnanometer gold clusters (au16–au18, au20, and au27–au35) for co oxidation. *ACS nano*, 5(10):7818–7829, 2011.

[173] Angelo Vargas, Gianluca Santarossa, Marcella Iannuzzi, and Alfons Baiker. Fluxionality of gold nanoparticles investigated by born-oppenheimer molecular dynamics. *Physical Review B*, 80(19):195421, 2009.

[174] Nan Shao, Wei Huang, Yi Gao, Lei-Ming Wang, Xi Li, Lai-Sheng Wang, and Xiao Cheng Zeng. Probing the structural evolution of medium-sized gold clusters: Au n-(n= 27- 35). *Journal of the American Chemical Society*, 132(18):6596–6605, 2010.

[175] Seema Pande, Wei Huang, Nan Shao, Lei-Ming Wang, Navneet Khetrapal, Wai-Ning Mei, Tian Jian, Lai-Sheng Wang, and Xiao Cheng Zeng. Structural evolution of core–shell gold nanoclusters: Au n–(n= 42–50). *ACS nano*, 10(11):10013–10022, 2016.

[176] Runhai Ouyang, Yu Xie, and De-en Jiang. Global minimization of gold clusters by combining neural network potentials and the basin-hopping method. *Nanoscale*, 7(36):14817–14821, 2015.

[177] Vladimir A Froltsov and Karsten Reuter. Robustness of 'cut and

splice'genetic algorithms in the structural optimization of atomic clusters. *Chemical Physics Letters*, 473(4-6):363–366, 2009.

[178] Zhanghui Chen, Xiangwei Jiang, Jingbo Li, and Shushen Li. A sphere-cut-splice crossover for the evolution of cluster structures. *The Journal of chemical physics*, 138(21):214303, 2013.

[179] Marie-Christine Daniel and Didier Astruc. Gold nanoparticles: assembly, supramolecular chemistry, quantum-size-related properties, and applications toward biology, catalysis, and nanotechnology. *Chemical reviews*, 104(1):293–346, 2004.

[180] Claire M Cobley, Jingyi Chen, Eun Chul Cho, Lihong V Wang, and Younan Xia. Gold nanostructures: a class of multifunctional materials for biomedical applications. *Chemical Society Reviews*, 40(1):44–56, 2011.

[181] Zhiyao Duan, Yuanyuan Li, Janis Timoshenko, Samuel T Chill, Rachel M Anderson, David F Yancey, Anatoly I Frenkel, Richard M Crooks, and Graeme Henkelman. A combined theoretical and experimental exafs study of the structure and dynamics of au 147 nanoparticles. *Catalysis Science & Technology*, 6(18):6879–6885, 2016.

[182] Samuel T Chill, Rachel M Anderson, David F Yancey, Anatoly I Frenkel, Richard M Crooks, and Graeme Henkelman. Probing the limits of conventional extended x-ray absorption fine structure analysis using thiolated gold nanoparticles. *ACS nano*, 9(4):4036–4042, 2015.

[183] Wen Wu Xu, Yi Gao, and Xiao Cheng Zeng. Unraveling structures of protection ligands on gold nanoparticle au68 (sh) 32. *Science advances*, 1(3):e1400211, 2015.

[184] Zhen Hua Li and Donald G Truhlar. Nanothermodynamics of metal nanoparticles. *Chemical Science*, 5(7):2605–2624, 2014.

[185] Donald Allan McQuarrie and John Douglas Simon. *Physical chemistry: a molecular approach*, volume 1. University science books Sausalito, CA, 1997.

[186] Britt Hvolbæk, Ton VW Janssens, Bjerne S Clausen, Hanne Falsig, Claus H Christensen, and Jens K Nørskov. Catalytic activity of au nanoparticles. *Nano Today*, 2(4):14–18, 2007.

[187] M Haruta and M Date. Appl catal a. *Gen*, 222:427, 2001.

[188] Gao Li and Rongchao Jin. Atomically precise gold nanoclusters as new model catalysts. *Accounts of chemical research*, 46(8):1749–1758, 2013.

[189] Hannu Häkkinen. Atomic and electronic structure of gold clusters: understanding flakes, cages and superatoms from simple concepts. *Chemical Society Reviews*, 37(9):1847–1859, 2008.

[190] Masatake Haruta. Size-and support-dependency in the catalysis of gold. *Catalysis today*, 36(1):153–166, 1997.

[191] MS Chen and DW Goodman. The structure of catalytically active gold on titania. *science*, 306(5694):252–255, 2004.

[192] Angelo Vargas, Gianluca Santarossa, Marcella Iannuzzi, and Alfons Baiker. Fluxionality of gold nanoparticles investigated by born-oppenheimer molecular dynamics. *Physical Review B*, 80(19):195421, 2009.

[193] Matthias Arenz, Uzi Landman, and Ueli Heiz. Co combustion on supported gold clusters. *ChemPhysChem*, 7(9):1871–1879, 2006.

[194] Xiao Gu, Satya Bulusu, Xi Li, Xiao C Zeng, Jun Li, Xingao G Gong, and Lai-Sheng Wang. Au34-: A fluxional core- shell cluster. *The Journal of Physical Chemistry C*, 111(23):8228–8232, 2007.

[195] Andrés Aguado and José M López. Small sodium clusters that melt gradually: Melting mechanisms in na 30. *Physical Review B*, 74(11):115403, 2006.

[196] Aldo Glielmo, Peter Sollich, and Alessandro De Vita. Accurate interatomic force fields via machine learning with covariant kernels. *Physical Review B*, 95(21):214302, 2017.

[197] Zhenwei Li, James R Kermode, and Alessandro De Vita. Molecular dynamics with on-the-fly machine learning of quantum-mechanical forces. *Physical review letters*, 114(9):096405, 2015.

[198] Jingheng Wu, Lin Shen, and Weitao Yang. Internal force corrections with machine learning for quantum mechanics/molecular mechanics simulations. *The Journal of chemical physics*, 147(16):161732, 2017.

[199] Samad Hajinazar, Junping Shao, and Aleksey N Kolmogorov. Stratified construction of neural network based interatomic models for multicomponent materials. *Physical Review B*, 95(1):014114, 2017.

[200] Venkatesh Botu and Rampi Ramprasad. Learning scheme to predict atomic forces and accelerate materials simulations. *Physical Review B*, 92(9):094306, 2015.

[201] Venkatesh Botu, Rohit Batra, James Chapman, and Rampi Ramprasad. Machine learning force fields: Construction, validation, and outlook. *The Journal of Physical Chemistry C*, 121(1):511–522, 2016.

[202] Siva Chiriki, Shweta Jindal, and Satya S Bulusu. ct phase diagram and landau free energies of (agau) 55 nanoalloy via neural-network molecular dynamic simulations. *The Journal of chemical physics*, 147(15):154303, 2017.

[203] Enrico Clementi and D-L_ Raimondi. Atomic screening constants from scf functions. *The Journal of Chemical Physics*, 38(11):2686–2689, 1963.

[204] Enrico Clementi, DL Raimondi, and William P Reinhardt. Atomic screening constants from scf functions. ii. atoms with 37 to 86 electrons. *The Journal of chemical physics*, 47(4):1300–1307, 1967.

[205] Anna L Gould, Andrew J Logsdail, and C Richard A Catlow. Influence of composition and chemical arrangement on the kinetic stability of 147-atom au–ag bimetallic nanoclusters. *The Journal of Physical Chemistry C*, 119(41):23685–23697, 2015.

[206] Anna L Gould, Kevin Rossi, C Richard A Catlow, Francesca Baletto, and Andrew J Logsdail. Controlling structural transitions in auag nanoparticles through precise compositional design. *The journal of physical chemistry letters*, 7(21):4414–4419, 2016.

[207] Xóchitl López Lozano, C Mottet, and H-Ch Weissker. Effect of alloying on the optical properties of ag–au nanoparticles. *The Journal of Physical Chemistry C*, 117(6):3062–3068, 2013.

[208] Michael Büttner, Thomas Belser, and Peter Oelhafen. Stability of thiol-passivated gold particles at elevated temperatures studied by x-ray photoelectron spectroscopy. *The Journal of Physical Chemistry B*, 109(12):5464–5467, 2005.

[209] Haoxiang Xu, Daojian Cheng, Yi Gao, and Xiao Cheng Zeng. Assessment of catalytic activities of gold nanoclusters with simple structure descriptors. *ACS Catalysis*, 8(10):9702–9710, 2018.

[210] Kenji Koga, Tamio Ikeshoji, and Ko-ichi Sugawara. Size-and temperature-dependent structural transitions in gold nanoparticles. *Physical review letters*, 92(11):115507, 2004.

[211] DM Foster, R Ferrando, and RE Palmer. Experimental determination of the energy difference between competing isomers of deposited, size-selected gold nanoclusters. *Nature communications*, 9(1):1–6, 2018.

[212] Kuo Bao, Stefan Goedecker, Kenji Koga, Frédéric Lançon, and Alexey Neelov. Structure of large gold clusters obtained by global

optimization using the minima hopping method. *Physical Review B*, 79(4):041405, 2009.

[213] Dawn M Wells, Giulia Rossi, Riccardo Ferrando, and Richard E Palmer. Metastability of the atomic structures of size-selected gold nanoparticles. *Nanoscale*, 7(15):6498–6503, 2015.

[214] Ask Hjorth Larsen, Jens Jørgen Mortensen, Jakob Blomqvist, Ivano E Castelli, Rune Christensen, Marcin Dułak, Jesper Friis, Michael N Groves, Bjørk Hammer, Cory Hargus, Eric D Hermes, Paul C Jennings, Peter Bjerre Jensen, James Kermode, John R Kitchin, Esben Leonhard Kolsbjerg, Joseph Kubal, Kristen Kaasbjerg, Steen Lysgaard, Jón Bergmann Maronsson, Tristan Maxson, Thomas Olsen, Lars Pastewka, Andrew Peterson, Carsten Rostgaard, Jakob Schiøtz, Ole Schütt, Mikkel Strange, Kristian S Thygesen, Tejs Vegge, Lasse Vilhelmsen, Michael Walter, Zhenhua Zeng, and Karsten W Jacobsen. The atomic simulation environment—a python library for working with atoms. *Journal of Physics: Condensed Matter*, 29(27):273002, 2017.

[215] S. R. Bahn and K. W. Jacobsen. An object-oriented scripting interface to a legacy electronic structure code. *Comput. Sci. Eng.*, 4(3):56–66, MAY-JUN 2002.

[216] Heehyun Baek, Jiwon Moon, and Joonghan Kim. Benchmark study of density functional theory for neutral gold clusters, au n (n= 2–8). *The Journal of Physical Chemistry A*, 121(12):2410–2419, 2017.

[217] Yuan-Kun Shi, Zhen Hua Li, and Kang-Nian Fan. Validation of density functional methods for the calculation of small gold clusters. *The Journal of Physical Chemistry A*, 114(37):10297–10308, 2010.

[218] Zhen Hua Li, Ahren W Jasper, and Donald G Truhlar. Structures, rugged energetic landscapes, and nanothermodynamics of al n ($2 \leq n \leq 65$) particles. *Journal of the American Chemical Society*, 129(48):14899–14910, 2007.

[219] Peter William Atkins, Julio De Paula, and James Keeler. *Atkins' physical chemistry*. Oxford university press, 2018.

[220] MJEA Frisch and Trucks et al. Gaussian 09 revision d. 01. 2014.